Tephra layers in the marine environment: a review of properties and emplacement processes

Armin Freundt[1]*, Julie C. Schindlbeck-Belo[1], Steffen Kutterolf[1] and Jenni L. Hopkins[2]

[1]GEOMAR Helmholtz Centre for Ocean Research Kiel, 24148 Kiel, Germany

[2]School of Geography Environment and Earth Science, Te Herenga Waka – Victoria University of Wellington, New Zealand

AF, 0000-0003-3157-2266; JCSB, 0000-0001-5865-3272; SK, 0000-0002-0645-3399

*Correspondence: afreundt@geomar.de

Abstract: This review focuses on the recognition of volcanic ash occurrences in marine sediment cores and on using their appearance and properties to deduce their origin. Widespread marine tephra layers are important marker horizons for both volcanological as well as general geological investigations. We describe ash detection by visual inspection and logging of sediment cores. Ash layer structure and texture, particle morphologies and lithological compositions of primary volcanic deposits are summarized and processes modifying them are discussed, both natural processes acting on and in the seafloor, i.e. erosion and bioturbation, and anthropogenic modifications during drilling/coring and core preparation. We discuss primary emplacement processes of marine fall and flow tephra deposits derived from either subaerial or submarine sources in order to identify distinguishing properties. We also elaborate on processes generating secondary, resedimented volcaniclastic layers such as submarine landslides and shelf erosion as well as fluvial input and ice-rafting, and how they can be distinguished from primary volcaniclastic deposits, which is essential in tephrostratigraphy. Finally, methods of tephra correlation between cores and on-land deposits/volcanoes are illustrated because they allow us to extend the 1D information from single cores to 3D distribution and facies changes of tephras and to bridge the land–sea gap.

Large volume, highly explosive eruptions producing both a convective Plinian plume and large pyroclastic density currents can generate huge volumes of mostly ash-grade tephra that is widely dispersed in the atmosphere (Walker 1981; Rose and Durant 2009) across land, lakes and the ocean. The resulting Plinian and co-ignimbrite fallout ash layers thus can extend across different depositional environments and are practically instantaneously emplaced, which makes them ideal chronostratigraphic marker horizons. This qualification is enhanced by their often unique compositional characteristics which facilitate their correlation across large distances and facies changes. Additionally, these characteristics assist their precise age dating either by correlation with dated tephras on land or by radiometric dating of their containing minerals. Tephra marker beds are best preserved in the marine environment because large regions of the seafloor are unaffected by erosion and carry relatively little fauna producing bioturbation. Marine ash layers thus are an important tool in volcanology but also support other Earth science disciplines.

In volcanology, marine ash layers are used to improve determinations of magnitude, intensity and volatile budgets of past eruptions (e.g. Ninkovich *et al.* 1978; Ledbetter and Sparks 1979; Rose and Chesner 1990; Rampino and Ambrose 2000; Kutterolf *et al.* 2008*b*, 2015), to date volcanic events of unknown age using known bracketing tephra ages and pelagic sedimentation rates (e.g. Zielinski *et al.* 1997; Alloway *et al.* 2007; Froese *et al.* 2008; Kutterolf *et al.* 2008*a*, 2016, 2018; Lowe 2011), and to reveal the temporal succession of physical and geochemical changes of magmatic systems (e.g. Paterne *et al.* 1990; Schmincke and Sumita 1998; Allan *et al.* 2008). In addition, pelagic and lacustrine sedimentation rates and their lateral and temporal variations can be constrained by tephrostratigraphic data (Kutterolf *et al.* 2008*c*, 2016). Temporal correlations between ash layer successions and palaeoclimate and environmental proxies can provide insights into volcanism–climate interactions (e.g. Paterne *et al.* 1990; Kutterolf *et al.* 2013, 2019; Berben *et al.* 2020). Dated ash layers provide important anchor points when local $\delta^{18}O$ or palaeomagnetic records are calibrated against respective global records (e.g. Allan *et al.* 2008; Schindlbeck *et al.* 2018). A tephrochronological framework hosting deposits formed by non-volcanic geological processes can constrain the age and rates of these processes, such as the cyclic activity of marine fluid

From: Di Capua, A., De Rosa, R., Kereszturi, G., Le Pera, E., Rosi, M. and Watt, S. F. L. (eds)
Volcanic Processes in the Sedimentary Record: When Volcanoes Meet the Environment.
Geological Society, London, Special Publications, **520**,
https://doi.org/10.1144/SP520-2021-50

venting structures (Kutterolf *et al.* 2008*d*). Moreover, time constraints can be placed on diverse events such as the evolution of sedimentary basins (Çağatay *et al.* 2015) or the occurrence of submarine landslides (Harders *et al.* 2010) or seismites and tsunamiites from palaeoseismic activity (Seilacher 1969; Cita and Aloisi 2000; Lu *et al.* 2017). Freshly deposited ash can supply fertilizing nutrients to phytoplankton (Duggen *et al.* 2007; Langmann *et al.* 2010; Durant *et al.* 2012) but can also interrupt benthic fauna, providing the opportunity to observe species survival and recolonization (e.g. Hess and Kuhnt 1996; Hess *et al.* 2001). Ash beds also affect the geochemical environment in marine sediment and pore water, and resulting diagenetic processes (Haeckel *et al.* 2001; Kent *et al.* 2002; Schacht *et al.* 2008; Hong *et al.* 2020; Luo *et al.* 2020).

However, all the above stratigraphic applications are reliant on knowing the exact position of the primary volcanic event in the geological record, i.e. it is essential to distinguish primary from secondary, resedimented tephra. The distinction between primary and secondary marine volcaniclastic layers requires knowledge of how they are emplaced and how they may be modified after emplacement and during coring (e.g. Hunt and Najman 2003). These topics, together with the methods used for ash-layer correlations, are the focus of this review. Most of the topics discussed, although focused on marine ash layers, can also be applied to the lacustrine environment.

The first section describes the appearance and properties of marine ash deposits, how ash deposits can be recognized, and how they may be modified by post-emplacement and coring processes. The second section discusses the processes of primary emplacement of marine ash beds during volcanic eruptions, and the third discusses the processes that generate resedimented volcaniclastic deposits. The fourth section reviews criteria by which primary and secondary ash deposits may be distinguished, and the final section shows how ash deposits can be correlated between cores and with tephra deposits on land.

The appearance of marine ash beds

Properties of ash beds

Layers, pods, dispersed ash. In general, the appearance and classification of ash-bearing sediments can be characterized by different parameters. Visual identification of ash layers is easy when the ash forms millimetre- to centimetre-thick continuous, distinct and undistorted beds (Fig. 1). Visually recognizable are also ash pods, i.e. lenticular or irregularly shaped pockets of ash with sharp contact to host sediment and little or no internal sedimentary structures (e.g. Hopkins *et al.* 2020), that occur singularly or aligned at a given horizon, forming a pod layer (Fig. 1f, g). Ash pods can be found both closely associated (above or below) with ash layers, or occur apparently independently, depending on whether the primary ash bed was partially or completely eroded. Ash layers and pods have colour, strength, grain size and structure clearly distinct from almost any marine background sediment, even where such sediment contains dispersed ash. However, when mass wasting processes on a range of scales redistribute the ash visual recognition in core sections can become difficult, particularly in continental slope settings but also in abyssal basins (Kutterolf *et al.* 2008*a*). Additional parameters including lithological composition, degree of homogeneity of glass-shard compositions, and bedding structures are very useful to distinguish between primary and secondary ash layers, but also between fall and flow deposits (see the section 'Distinguishing primary and secondary ash layers').

Ash-containing sediment layers show marked differences in porosity, water content, density and grain size compared to ash-free mud sediment (Kutterolf *et al.* 2007). Some ash layers are significantly hardened compared to their host sediment due to diagenetic reactions typically of glass shards with pore waters. Silica and/or carbonate derived from an ash bed (cf. Luo *et al.* 2020) can cause hardening and discoloration of underlying sediment by incipient cementation up to a depth of several centimetres (Kutterolf *et al.* 2008*c*, 2016). Such changes are recorded by core logging techniques which assist core description by identification of both distinct layers and dispersed ashes in marine sediments. Standard core logging parameters include P-wave velocity, sediment density from gamma-wave attenuation, and magnetic susceptibility. Ash layers of both mafic and felsic compositions show elevated gamma density values (Fig. 2). Magnetic susceptibility is the degree to which a material can be magnetized by an external magnetic field and is proportional to the volume fraction of magnetic minerals (Hunt *et al.* 1995) that is taken as a measure of the concentration of ash. Kutterolf *et al.* (2007, 2008*a*) showed that mafic ashes can easily be recognized by elevated magnetic susceptibility (Fig. 2) due to their high contents of magnetic minerals (e.g. magnetite, chromite, siderite, hematite, titanomagnetite, franklinite, pyrrhotite). In contrast, felsic ashes which are poor in iron-rich minerals but rich in feldspar, glass, and related weathering products, are generally characterized by low magnetic susceptibility values (Hunt *et al.* 1995).

Ash particles. Felsic tephra layers in marine sediments are white, light grey, pinkish, or yellowish in colour, and are mainly (>90 vol%) composed of fresh, colourless glass shards to pumice lapilli. The

glass shards can vary from highly vesicular, pumiceous and fibrous textures with commonly elongated to tubular vesicles, to dense, angular blocky, cuspate, flat and y-shaped shards with nearly no bubbles (Fig. 3a–d). Vesicle texture reflects the conditions of extended magmatic degassing (high vesicularity, thin bubble walls) v. premature quenching (low vesicularity, thick bubble walls) whereas particle shape reflects fragmentation by bubble disruption (cuspate, y-shaped) v. brittle fracture (angular, blocky). Complex eruption mechanisms can generate ash with a mixture of vesicular and blocky shards (Fig. 1i–o). Felsic tephra beds can range from crystal poor (1–5 vol%) to crystal rich (up to 50 vol%, typically enriched at base), with dominant plagioclase and/or sanidine accompanied by variable occurrences of quartz, amphibole, clinopyroxene, orthopyroxene, Fe/Ti-spinel, and biotite as well as foid (feldspathoid) minerals (e.g. nepheline, leucite, haüyne) when alkaline magma compositions are involved. Additionally, lithic fragments of different types can occur that either derive from the source volcano or, particularly in the case of volcaniclastic turbidites, have been picked up from the seafloor such as shallow-water bioclasts (Sigurdsson *et al.* 1980; Manville and Wilson 2004).

In contrast, mafic ash layers are generally dark-grey to black in colour, and consist predominantly of dark brown sideromelane and tachylite shards or microcrystalline juvenile particles as well as fine scoria lapilli. The glass shards mostly have blocky shapes and are medium to poorly vesicular with mostly round and elliptical bubble shapes (Fig. 3e–g). Some mafic ash layers, particularly those from intense (sub-)Plinian mafic eruptions, contain dominantly highly vesicular, tubular, (light-)brownish to red–brown glass shards (Fig. 3f). The mineral assemblages of the mafic tephras include plagioclase, pyroxene, Fe/Ti-spinel, some olivine and apatite, as well as occasionally amphibole and, with highly alkaline compositions, phlogopite and foid minerals.

Ash fallout distribution. Highly explosive, typically Plinian and phreatoplinian, eruptions generate ash clouds that drift over huge distances and areas typically at stratospheric heights. For example, the 10 -cm-isopach of the 26.5 ka Kawakawa/Oruanui phreatoplinian fallout includes an area $\geq$1 000 000 km^2 (Carter *et al.* 1995; Wilson 2001). Indeed, Sun *et al.* (2014) and Koffman *et al.* (2013) have shown ash particles a few micrometres in size in ice cores from both polar regions, suggesting the finest ash of some huge ash clouds can, in fact, reach hemispheric to global dispersals (Dunbar *et al.* 2017). Ultra-distal and very fine ashes dispersed in sediment are difficult to identify but such 'cryptotephras' can still be found and analysed in marine and other settings but require special extraction techniques (Turney 1998; Davies 2015). Primary cryptotephra deposits form where the concentration of fallout of fine ash is very low, and are easily mixed with sediment by bioturbation. Davies (2015) provides a review of the sampling, analysis and interpretation of cryptotephras which provide valuable tephrostratigraphic data particularly where visible ash beds were not emplaced or preserved (e.g. van den Bogaard and Schmincke 2002; Abbott *et al.* 2011; Lowe *et al.* 2017; Wulf *et al.* 2018; Wastegard *et al.* 2020).

In marine sediment cores, analyses mostly deal with the visible fallout tephra layers a few millimetres to decimetres thick, which often thin with distance in an exponential fashion although there can be significant deviations from such a pattern (Fig. 4a). These unstratified layers are characterized by a sharp, horizontal to sub-horizontal basal contact to underlying background sediment (Fig. 1c–f) that may be disturbed by bioturbation (Fig. 1g) or other processes (Fig. 1d, h, i, j). The top can also be a sharp contact to overlying marine sediment (Fig. 1e, k) but is often diffuse due to a gradual transition into overlying ash-bearing sediment (up to 50 cm, apparently without systematic relation to ash layer thickness) which is then overlain by 'clean' (hemi) pelagic sediment (Manville and Wilson 2004; Kutterolf *et al.* 2007, 2008*a*, 2016, 2018; Eisele *et al.* 2015*b*; Schindlbeck *et al.* 2016*a*, 2018; Hopkins *et al.* 2020).

Grain-size characteristics. The lateral distribution of accumulation rate for each grain size is determined by its particle fall velocity, its concentration in the ash cloud and the volume flux of that cloud so that a range of grain sizes is emplaced at a given distance while the median grain size gets finer with distance (Sparks *et al.* 1992). Marine tephra beds are often well sorted and have average ash grain sizes ranging from *c.* 10 μm to *c.* 500 μm, which commonly decrease with distance (Fig. 4b), but may also occur as pumice or scoria lapilli layers over the proximal few tens of kilometres from the source (Fig. 1c, e). Since larger and denser particles sink faster through water, ash beds are commonly normally graded in grain size (Fig. 1e) as well as in grain density, which is visible as crystals or dense particles enriched towards the base of ash beds (Fig. 1h; Ninkovich *et al.* 1978; Sigurdsson *et al.* 1980; Kutterolf *et al.* 2018). The very fine ash, which is particularly abundant in silicic highly explosive eruptions (up to >50%; Rose and Durant 2009), is typically expected to be carried to great distances. However, marine ash layers with bimodal grain size distributions and correspondingly poorer sorting are also quite common. Bimodally distributed ash in more proximal locations typically becomes unimodal at greater distances because the coarse mode decreases with distance while the fine mode remains fairly constant

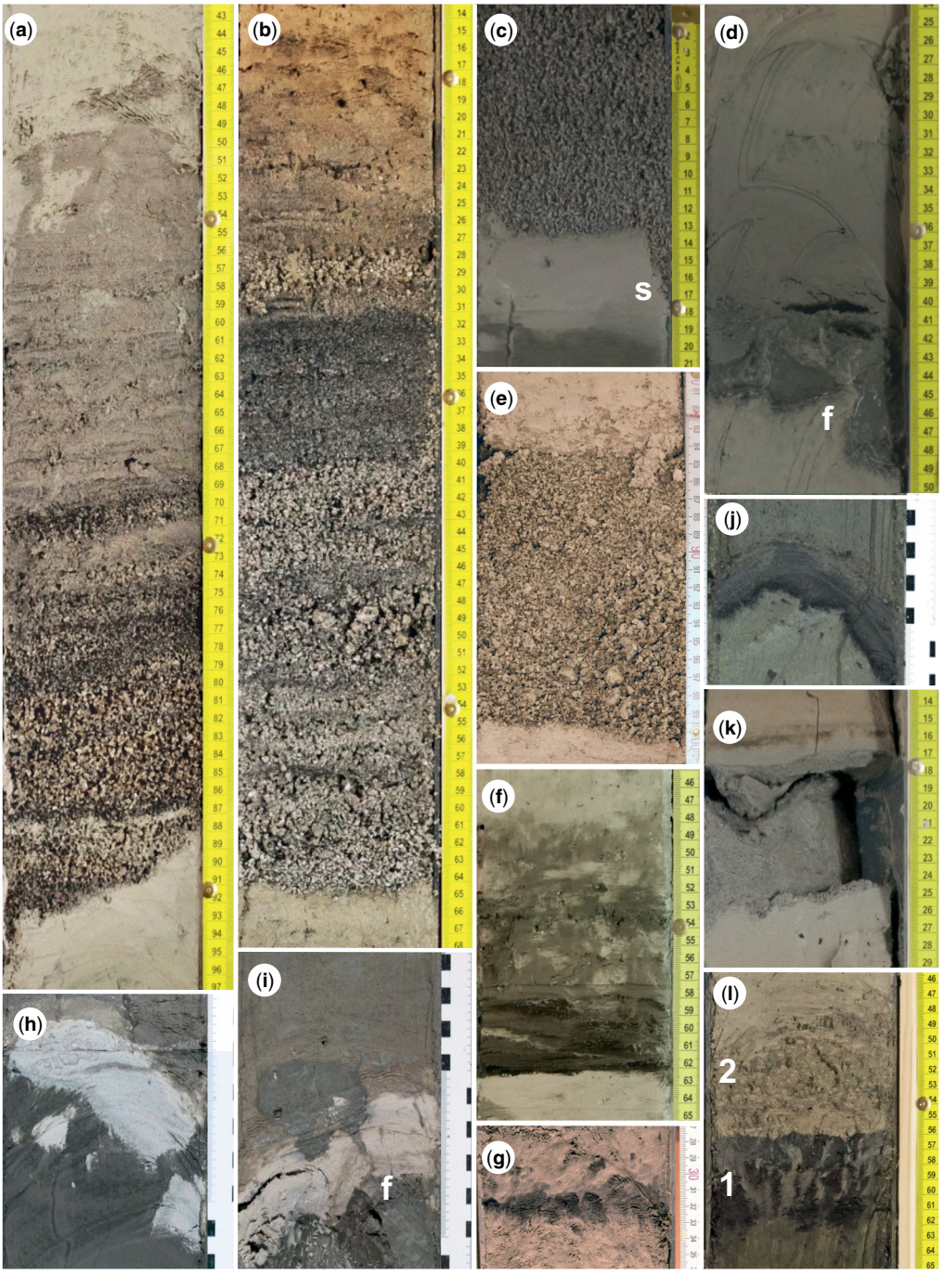

Fig. 1. (**a**) Submarine Cape Riva (22 ka) ash turbidite on eroded base, upward fining grain size from fine lapilli to fine ash paralleled by more intense stratification. Bioturbation at the top (POS513/14, 142–197 cm; 50 km NE from Santorini). (**b**) Turbidite facies of Minoan tephra (3.6 ka) stratified by alternating but upward fining grain size, with bioturbated top, in channel position 25 km NE of Santorini (POS513/20, 13–62 cm). (**c**) Minoan tephra well-sorted massive, reversely graded fallout facies 50 km east of Santorini in the 'shadow' of Anafi island. Downward shear s along liner (POS513/30, 43–64 cm). (**d**) Distal normal graded Minoan ash layer with midcore flow-in f at the

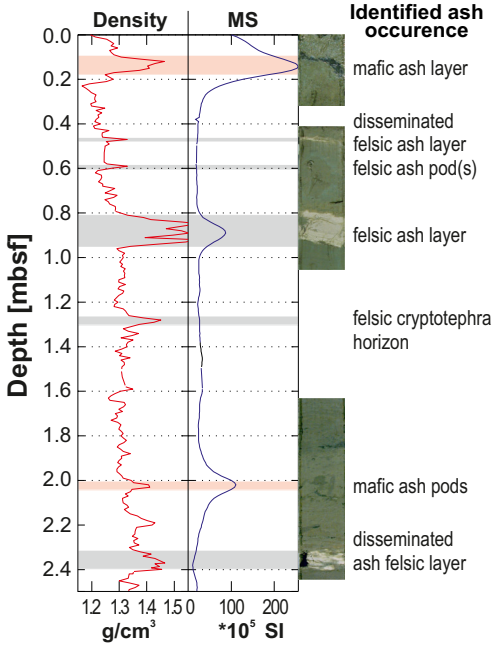

Fig. 2. Density and magnetic susceptibility (MS) logs of core M54/11 offshore Nicaragua indicating felsic (grey bars; high density, low MS) and mafic (red bars; high density, high MS) ash layers. Some of these are clearly visible in the core while others have been partially destroyed or dispersed by bioturbation. MS is expressed as the intensity ratio of the sediment magnetization to an external magnetic field.

(Sparks and Huang 1980; Brazier *et al.* 1983). For example, Pinatubo marine ash has a dominant coarse mode proximally but becomes bimodal with distance until it is dominated by the fine mode (Fig. 4c) when the coarse mode and median size decrease to the fine mode value (Fig. 4b; Wiesner *et al.* 2004). Bimodality can arise from different deposition modes acting simultaneously (Sparks and Walker 1977; Sparks and Huang 1980) such as closely associated emplacement of Plinian fallout and co-ignimbrite ash (Engwell *et al.* 2014) or immediately post-eruption settling of fine ash (Kandlbauer *et al.* 2013). Bimodality can also be caused by 'premature' scavenging from the eruption cloud of aggregated fine ash together with coarser ash (Carey and Sigurdsson 1982; Brazier *et al.* 1983; Wilson 2001; Van Eaton and Wilson 2013). Ash particles can form larger aggregates by wet adhesion in ash clouds that are humid due to condensation or phreatomagmatic origin (Moore and Peck 1962; Gilbert and Lane 1994; Schumacher and Schmincke 1995), or by electrostatic forces (James *et al.* 2002; Telling and Dufek 2012). Unless these aggregates cement quickly during transport (Gilbert and Lane 1994; Scolamacchia and Dingwell 2014) they will rapidly disintegrate when dropped into the ocean due to breakage at impact and loss of the adhesive forces in the water. Consequently, they are almost never found in deep-sea tephras and fine-ash fallout by aggregation is just inferred from the presence of a fine ash mode in the tephra. A rare exception of uncemented aggregates preserved in a marine ash bed is documented in Figure 1l and Cunningham and Beard (2014) report an example from uplifted Miocene deep-marine rocks.

Ash turbidites. So far we have considered massive ash beds that are typical for fallout emplacement, although pulse-like activity may also generate parallel stratified fallout layers. Many marine ash beds do, however, show features indicative of lateral transport along the ground such as wavy or cross-bedding and erosive basal contacts (Figs 1a, b & 5). These ash beds are often less well sorted than fallout ash layers (e.g. Trofimovs *et al.* 2008; Schindlbeck *et al.* 2013; Kutterolf *et al.* 2018). Their internal structure can correspond to the Bouma divisions well known from non-volcanic turbidites (e.g. Fig. 5a; Trofimovs

Fig. 1. *Continued.* liquefied base. At the top, diffuse transition from ash to sediment (POS513/34, 20–51 cm; 110 km ENE from Santorini). (**e**) 17 cm-thick, massive coarse ash/fine lapilli layer with sharp base and top; fauna extinction inhibited bioturbation (M141-1154, 84–101 cm; 70 km east of São Miguel, Azores). (**f**) About 5 cm-thick mafic fine-ash layer with sharp base but overlain by *c.* 10 cm bioturbated dark ash–light pelagic sediment mixture, indicating fast fauna recovery after ash deposition (M141-1174, 328–348 cm; central Azores). (**g**) Thin mafic fine-ash bed almost completely disturbed by intense bioturbation creating ash pods; fauna probably survived ash deposition (M141-1154, 727–736 cm; central Azores). (**h**) Felsic ash layer with crystal-rich base (darker 1 cm along base) rotated and fragmented by coring (M66/222, 218–241 cm; 25 ka Upper Apoyo Tephra, Nicaragua). (**i**) Felsic ash layer dissected by coring, with upward flow-in f of underlying softer sediment through crack (M66-229, 508–531 cm; 75 ka Los Chocoyos Tephra). (**j**) Normally graded mafic ash with up-arching base due to core deformation (M66-223, 292–307 cm). (**k**) Medium ash disturbed by core extension and liquefaction, internal structures destroyed and ash partly washed out (POS513/53, 13–29 cm; Minoan ash 150 km east of Santorini). (**l**) A grey fine-ash layer 2 with abundant lighter coloured, slightly flattened ash aggregates immediately and sharply overlies a black scoria ash layer 1, possibly representing a mafic eruption on land that changed from magmatic to phreatomagmatic. Shallow (353 m) water depth and transport in slow ground-hugging ash cloud rather than fall from great height may have favoured preservation of the soft ash aggregates (POS513/46, 171–184 cm; 33 km SW Nisyros).

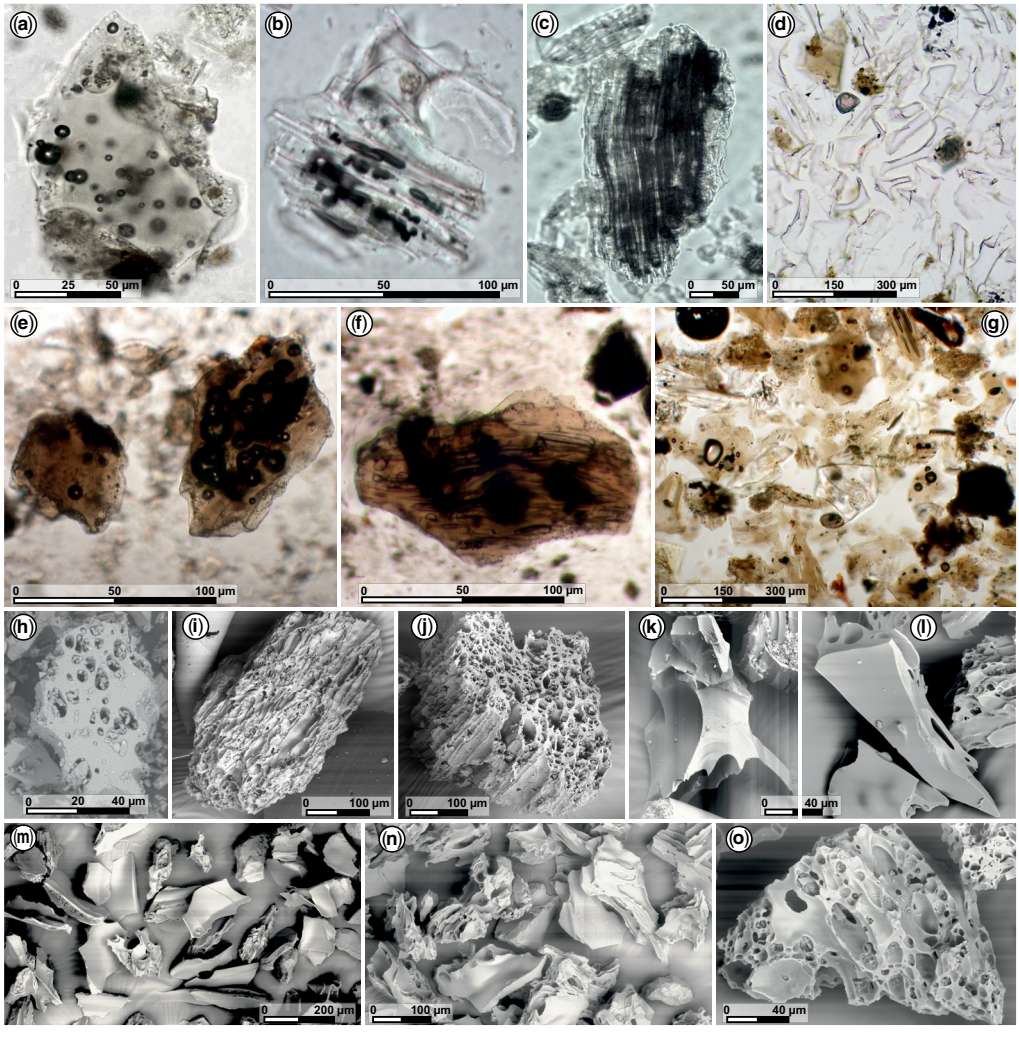

Fig. 3. Optical and electron microscope photographs. (**a**) Dense angular glass shard with few round and elliptical vesicles (IODP Exp. 346-U1442A-2R-1, 7 cm). (**b**) Felsic glass shard with fine tubular vesicles and wall segments of larger round vesicles (M66–222, 273 cm). (**c**) Felsic pumiceous shard with bent tubular vesicles (IODP Exp. 352-U1439A-3H-1, 7 cm). (**d**) Large blocky cuspate felsic glass shards (M66-229, 535 cm). (**e**) Blocky mafic sideromelane shards with (right) and without (left) vesicles (M66-223, 305 cm). (**f**) Sideromelane shard with elongated and tubular vesicles (M66-222, 440 cm). (**g**) Mixture of dense and variably vesicular sideromelane shards (M66/222, 518 cm). (**h**) Poorly vesicular glass shard similar to A (IODP Exp. 375-U1520C-2R-1, 104 cm). (**i**) Highly vesicular pumice particle with twisted tubular vesicles (POS513-31, 5 cm). (**j**) Tube pumice fragment (POS513-31, 5 cm). (**k**) Cuspate glass shard (POS513-20, 6 cm). (**l**) Blocky glass shard with very few vesicles (POS513-16, 30 cm). (**m**) Mostly blocky and cuspate glass shard assemblage (POS513-17, 32 cm). (**n**) Cuspate and pumiceous glass shard assemblage (POS513-16, 45 cm). (**o**) Pumice with larger elongated and smaller round vesicles (POS513-16, 45 cm). Images i to o are all from submarine tephra emplaced by the 1650 Kolumbo eruption, Aegean Sea.

et al. 2008). Large volcaniclastic turbidites can be generated by submarine landslides (see 'Volcanic landslides') while primary ash turbidites are typically generated where pyroclastic flows enter the sea (see 'Submarine ash deposits from subaerial pyroclastic density currents'). Sparks *et al.* (1980) argued that some pyroclastic flows entering the sea may maintain their integrity but geological evidence for intact pyroclastic flow deposits in the sea are restricted to very shallow near-shore waters (Reedman *et al.* 1987; Kokelaar and Busby 1992; Mandeville *et al.* 1994, 1996; White and McPhie 1997).

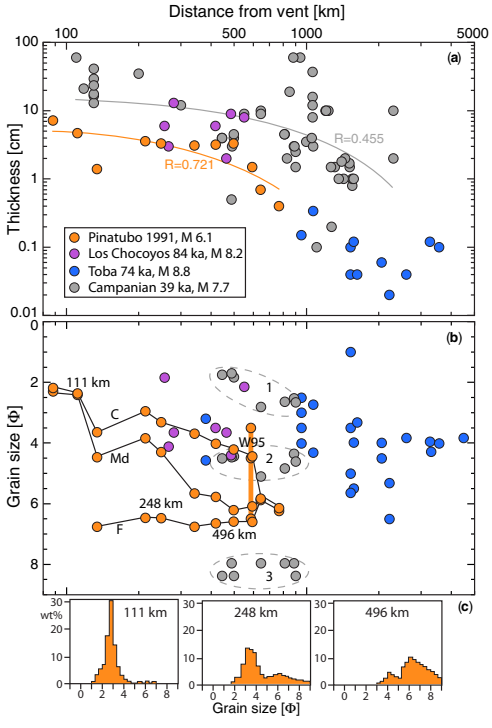

Fig. 4. (**a**) Thickness and (**b**) grain size v. distance for selected marine tephras from major eruptions. Colour-coded lines in (a) show exponential fits to Campanian and Pintubo data; wide scatter around the fit is partly due to sample sites off the fan axis. Dashed envelopes in (b) identify three subpopulations in the bimodally distributed Campanian Ignimbrite tephra. Lines C, Md, and F connect coarse mode, median and fine mode grain sizes in the Pinatubo data in (b); orange bar W95 marks these grain sizes observed in sediment traps. (**c**) Proximal unimodal to distally bimodal grain size distributions of Pinatubo 1991 tephra at the distances indicated also in (b). Data sources: Pinatubo 1991 data from Wiesner *et al.* (1995, 2004); Los Chocoyos own data; Young Toba Tuff data from Gatti and Oppenheimer (2012); Campanian Ignimbrite data from Engwell *et al.* (2014). In this tephra the coarse mode represents the Plinian fallout and the fine mode the co-ignimbrite ash contributions.

With steeper slopes and deeper waters, intense mixing dominates and pyroclastic density currents are converted into volcaniclastic turbidity currents. Ash turbidites can occur as singular layers intercalated with marine sediments but often they form piles of multiple beds particularly when the source eruption was unsteady or multi-episodic (Fig. 5). The Bouma division of turbidites includes normally graded or completely massive facies next to facies with tractional bedforms. Normal grading of fine ash in distal turbidites originates from suspension sedimentation from waning flow (see 'Submarine ash deposits from subaerial pyroclastic density currents') and such facies is difficult to distinguish from ash beds emplaced by fallout. On the other hand, thick massive volcaniclastic turbidite deposits can show coarse-tail grain size and density segregation features resembling those observed in ignimbrites on land (Sparks *et al.* 1973), such as pumice and lithic concentration zones (Schindlbeck *et al.* 2013, Kutterolf *et al.* 2018). An example of proximal turbidite facies is the submarine deposit related to terrestrial ignimbrite in Japan, which comprises <1.2 m of a lower pebble facies, a central pumice breccia/sand facies 4.5 m thick, and a very thick (>15 m) top facies of stratified vitric ash composed of normally graded beds (Allen *et al.* 2012). An erosive basal contact, ripped-up mud clasts, and laterally very variable bedforms attest to high energy flow.

Modifications on and in the seafloor

Tephrochronology has its basis in the recognition and connection of regionally or globally synchronous events (isochrons), however, this can become complex when the primary deposits have been modified. Ash deposits are easily agitated in their unconsolidated state shortly after deposition by passing turbidity currents or by semi-permanent bottom currents and episodic re-sedimentation processes (Ninkovich and Shackleton 1975; Carey and Sigurdsson 1978; Sparks *et al.* 1983; Carter *et al.* 1995; Wallrabe-Adams and Lackschewitz 2003; Manville and Wilson 2004). Survival of, or rapid recolonization by, benthic biota can lead to intense bioturbation of ash layers. Differential compaction as a function of burial depth, grain size, and sorting modifies layer thicknesses. The thicknesses of ash beds observed in widely spaced drill cores (which cannot image local variations) thus have some uncertainty that carries into quantification of isopachs and the derived eruption parameters (Manville and Wilson 2004). For example, IODP expedition 350 drilled four holes just a few tens of metres apart but even across such short distances the marine tephra deposits showed varying thicknesses, preservation, and even occurrence (Tamura *et al.* 2015, fig. F17). Sevink *et al.* (2020) also emphasize the need of multiple coring to better assess ash layer stratigraphy and properties.

Slumping/folding on slopes. In high-relief regions of frequent mass movement events post-depositional modification of tephra is common (Carter *et al.* 1995). For example, repeated ash beds with identical glass-shard geochemical compositions, separated by marine sediments have been interpreted to result from repeated slumping of tephra packages at the shelf or slope (e.g. Allan *et al.* 2008; Eisele *et al.*

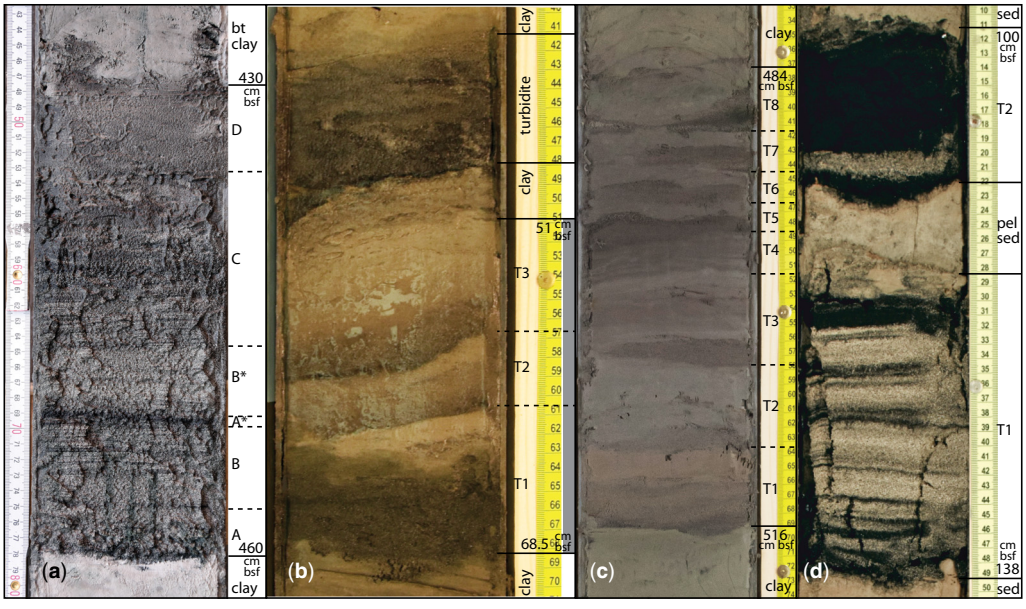

Fig. 5. (**a**) Ash turbidite above slightly eroded base. Normally graded coarse ash zone A overlain by planar stratified zone B. A* is a reversal to coarser grain size followed by weakly stratified zone B* with its light colour due to abundant foraminifera. Zone C is low-angle cross-stratified medium to fine ash capped by massive to weakly stratified fine-ash zone D. Zones A to D correspond to Bouma turbidite divisions of upper flow regime suspension fallout (A) and planar lamination (B) to lower flow regime tractional bed-load (C) and suspension sedimentation (D). Note vertical flowage along core liner (M141-1174, 427–461 cm; central Azores). (**b**) Ash layer from the 39 ka Campanian Ignimbrite eruption north of Stromboli (POS522/51, 51–68 cm; 215 km S from vent). The pile of three (T1 to T3) turbidite beds normally graded from dark medium ash to light very fine ash reflects the multi-phase character of the eruption (Rosi *et al.* 1996). This is pyroclastic flow-derived ash because Plinian fallout was dispersed strictly eastward (Rosi *et al.* 1999; Engwell *et al.* 2014). (**c**) Pile of at least eight turbidites correlated with the *c.* 54 ka Upper Nisyros Pumice fall–surge–flow tephra succession (POS513/45, cm; 20 km SW of Nisyros). Direct contacts of the turbidite layers in b and c indicate rapid emplacement succession. (**d**) Lower turbidite T1 of alternating and mixed coarse black ash and white foraminifer sand and upper turbidite T2 mainly of massive black volcaniclastics but containing light layer rich in foraminifers. T2 is the distal equivalent of the first of two major collapses at the eastern flank of Fogo volcano (Cape Verdes) while T1 may have formed by stepwise smaller collapses or resedimentation. Core M155/14, 100–140 cm; *c.* 200 SSE from Fogo; note marginal faulting in T1 by coring.

2015*a*). Even large coherent bodies of material with minimal internal deformation and intact internal stratigraphically can pile up to form repeated sequences (Allan *et al.* 2008). Such mass movements are typically triggered by gravitational instability and tectonic processes. Porous ash layers enclosed between impermeable clayey sediments can themselves become a cause for failure when liquefaction, possibly triggered by earthquakes, reduces their shear strength and thus creates a slip plane on which the overlying sediment package can glide (Harders *et al.* 2010; Sammartini *et al.* 2018). Rough and angular particles increase the shear strength of an ash layer but ash alteration (see 'Alteration of glass' below) reduces shear strength and increases the potential for slope failure (Wiemer and Kopf 2015).

While sediment and ash packages are in a soft, uncompacted state they can creep and fold even on gentle slopes. Soft-sediment deformation structures such as load and flame structures, convolute lamination and folding then form particularly where porous, water-soaked sediment is capped by impermeable fine sediment as in the case of turbidites (Fig. 6). If such deformation involved cross-stratified strata and is later also overprinted by tectonic faulting, the resulting structures can be very complex indeed (Fig. 6a).

Modification by bioturbation. Bioturbation is the mixing impact caused by fauna living both in and on the sediment in which the tephra is deposited. This mixing is most commonly caused by burrowing, feeding, defecation and locomotion, and can mix ash both above and below the primary ash layer (Todd *et al.* 2014). Such bioturbation is the key mechanisms for ash pod formation although occasionally ash pods also form by soft sediment deformation (Pillans *et al.* 2005; Callow and McIlroy

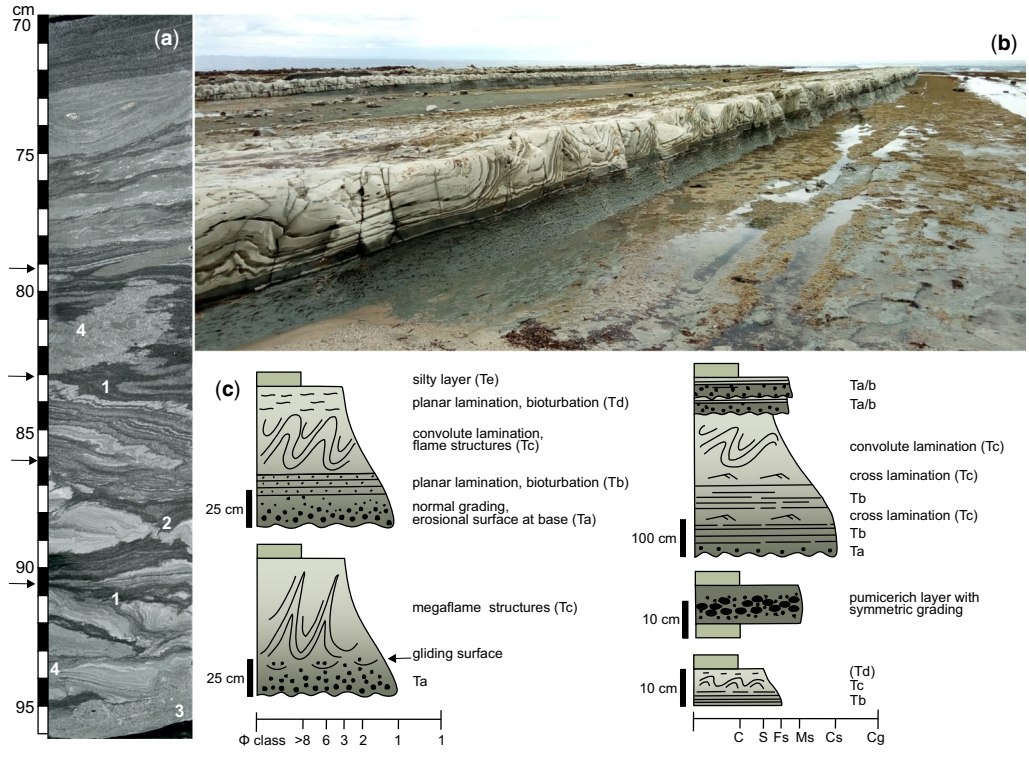

Fig. 6. (**a**) Chaotic deposit of laminated volcaniclastic sandstone showing isoclinal folding (1), attenuation of beds (2), load and flame structures (3), and current-ripple lamination and sandstone injections (4). These chaotic structures formed by syn-sedimentary creeping and folding. Later-stage tectonics created sharp detachment surfaces (arrows at left) at which bedding dip changes abruptly, dividing the deposit into at least three discrete zones, with the lowermost zone having the most intense internal deformation (IODP Expedition 322, interval C0012A-45R-1, 70–96 cm). (**b**) Field photograph by J. Hopkins of Mahia peninsula, New Zealand, showing features illustrated in (c). (**c**) Schematic depositional sequences of ash turbidites of the Middle Miocene interval of Mahia Peninsula. Drawing modified after Schneider *et al.* (2001), with permission from Elsevier © 2001. Left sketches show classical turbidite sequences with Bouma divisions (Ta–Te). Right sketches show, from top to base, an amalgamated turbidite, pumice concentration layer, and incomplete sequence of a distal turbidite. Grain size Φ fractions (left) and corresponding classes (right) clay (c), silt (s), fine, middle, coarse sand (Fs, Ms, Cs) and coarse gravel (Cg).

2011; Hopkins *et al.* 2020). The cutting effect can show pod-like 2D shapes on the drill core surface which, in fact, are part of a complex 3D structure of the (deformed, disrupted, bioturbated) ash deposit. Such complex structures can nowadays be visualized by high-resolution X-ray micro-tomography (Griggs *et al.* 2015), which can reveal the mechanism of formation more accurately.

High sedimentation rates (typically >20 cm ky^{-1}) of either pelagic sediment or ash minimize bioturbation (Thornalley *et al.* 2011). Wetzel (2009) distinguished between (1) 'non-local mixing' by deep burrows, which penetrate an ash layer, (2) 'mixing from below' by Scolicia producers, and (3) 'mixing from above/local mixing' by crawling macro- and megafauna. While deep burrows affect the tephra layers only very locally, mixing from below and above can destroy even several cm-thick ash layers. Ash deposits <1 cm thick rarely survive as laterally continuous layers but evidence of their existence can be commonly found by volcaniclastic infillings of burrows formed by bioturbation (e.g. Huang *et al.* 1975; Kennett 1981; Hess and Kuhnt 1996; Marquez 2000; Manville and Wilson 2004; Todd *et al.* 2014; Hopkins *et al.* 2020). This suggests that tephra horizons <1 cm thick are insufficient to suppress benthic biota activity or post-depositional bioturbation (e.g. Carter *et al.* 1995; Hess and Kuhnt 1996; Marquez 2000). Slow settling of fine-ash particles (<32 μm), favours survival of upward-burrowing benthic fauna and, hence, disruption of the ash deposit (Fig. 1g). Conversely, the commonly observed sharp basal contacts of coarser, thicker (≥1 cm) and rapidly accumulated ash suggest

smothering of benthic fauna although burrowing after recolonization can still modify such ash beds (Fig. 1f). A sharp top contact to overlying sediment is not commonly preserved unless an ash bed is coarse grained or was rapidly covered by thick sediment (Fig. 1e). The top is often a diffuse gradual transition into overlying sediment that is rich in ash due to bioturbation after relatively rapid post-depositional recolonization of the sea bed (e.g. Cita and Podenzani 1980; Marquez 2000; Hess *et al.* 2001). The Pinatubo 1991 event illustrates the rate of recolonization: 5 years after the eruption the foraminifera assemblages on the seafloor had not yet recovered to the pre-eruptive state (Marquez 2000). Figure 7 illustrates an example of a felsic ash layer above which ash particles have been mixed with hemipelagic sediment by bioturbation such that the ash concentration gradually decreases upward to at least 15 cm above the primary ash bed.

The use of cryptotephra deposits to increase the resolution of tephrochronology is becoming increasingly popular, therefore the impact of bioturbation on tephra deposits needs to be carefully considered as it may cause uncertainties in defining isochrons (e.g. Davies *et al.* 2014). Only non-modified cryptotephra will show a sharp peak in shard concentrations and thus an obvious isochron (e.g. Berben *et al.* 2020).

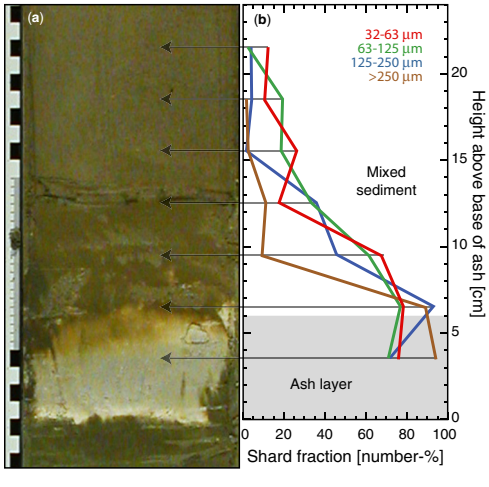

Fig. 7. (**a**) Gravity core section of station SO 173-17 off the Pacific coast of central Nicaragua showing the light-colored marine ash bed of the 25 ka Upper Apoyo Tephra from Apoyo Caldera, Nicaragua. It is under- and overlain by silty clay sediment. (**b**) Point-counted number fraction of felsic glass shards for the grain-size fractions indicated. Admixed ash in the sediment is found up to at least 15 cm above the ash bed, and apparently finer shards (<125 µm) are mixed farther than coarser (>125 µm) ones. J. Schindlbeck-Belo, unpublished data.

Different bathymetric settings, the nature of the sediments, and assemblages of faunal species cause great variability in the rate and extent of bioturbation (Todd *et al.* 2014). For example, in low energy, estuarine environments bioturbation occurs rapidly but potentially only to a depth of ≤20 mm (e.g. Solan *et al.* 2004; Todd *et al.* 2014). Conversely, deep marine environments show evidence for deep mixing of sediments by a range of fauna (e.g. Marquez 2000; Wetzel 2009). Biological activity in marine sediments can also physically alter glass shards, forming *bioalteration textures* (called *etch pits* by those favouring a non-biogenic origin), including granular or tabular textures, fractures and voids (Fisk and McLoughlin 2013).

Ash layer preservation. Distal ash layers in mostly non-erosive marine environments generally have a much better chance of preservation than comparative deposits on land, where thin ash beds often already disappear during the next rain fall. However, preservation of marine ash beds is still threatened by erosion by aqueous and turbidity currents, mixing by sediment slumping and sliding on slopes, and mixing by seafloor fauna. Erosive currents and mechanical mixing processes can occur in regions of high bathymetric relief and steep slopes as well as in canyons and trenches (e.g. Hopkins *et al.* 2020). On the other hand, elevated plateaus where density currents do not reach or are not erosive provide a high potential for ash-layer preservation. Bathymetric relief can be particularly complex around volcanic ocean islands so that preservation conditions can change quickly laterally. Conversely, regions of high sedimentation rates provide the chance for ash beds to be quickly covered by thick turbidites and thereby protected from the modification by benthic fauna (Carter *et al.* 1995). Relatively thick ash layers in isolated basins also have a great potential of preservation (Hopkins *et al.* 2020). Ash layer disturbance up to complete mixing by bioturbation requires that benthic fauna either survive ash deposition or quickly recolonize the seafloor. Faunal recovery is fastest where the fauna had already adapted to mixed, sandy sediment (i.e. grain size similar to ash) in contrast to fauna living on mud (Wetzel 2009; Cassidy *et al.* 2014). Relatively rapid accumulation of nutrient-rich sediment forming a fauna habitat on top of an ash bed also favours fast fauna recovery and resulting ash disturbance, such as in regions of terrigenous input or strong upwelling (Wetzel 2009). Thicker ash beds result in longer times for fauna recovery, and thus have a better chance of survival until deeper burial. Depending on the thickness of an ash bed, benthic faunal activity can create a several centimetres thick mixed zone (Wetzel 2009) that can completely replace thin ash beds or form at the top of thicker ash beds (Fig. 7). In summary, the highest

preservation potential even of thin ash layers can be expected in the abyssal plains where background sediment is mud, and burial rate of organic matter (food) and faunal productivity are low (Wetzel 2009).

Modification by coring

Causes of core disturbances commonly are operational, anthropogenic, formation-induced, or a combination of the three. The appearances of core deformation structures and their formation processes have been summarized by Jutzeler *et al.* (2014*b*) for IODP coring techniques but also apply to all other coring techniques. A modification common to all rotary, piston and gravity coring methods is that the seafloor/seawater interface is initially disrupted to a certain degree that is not quantifiable due to the variable relations between penetration forces and sediment firmness. Deeper in the cores, drilling/coring disturbances can modify structure and texture by deformation as well as the composition of the ash layers by mixing with sediment. Common features are shear deformation of sediment against the core barrel, basal flow-in or core extension due to underpressure during pull-out, expansion and dissection of core material due to escape of gas, sediment loss through the core catcher, fall-in during core barrel exchange, and core transport-induced modifications such as liquefaction. Coring disturbances thus can significantly influence sediment interpretations but are often underappreciated. For example, an up-arching (Fig. 1j) or down-sheared (Fig. 1c), formerly planar base of an ash layer may wrongly be interpreted as an erosive contact. Core disturbances occur particularly where more competent, none-cohesive (but sometimes incipiently cemented) layers of fine to coarse ash or lapilli are intercalated within less competent, cohesive, clay-rich layers (Fig. 1h, i). These contrasting physical properties (e.g. yield strength, viscosity) lead to different deformation reactions to the stress applied by the corer. Moreover, liquefaction may lead to vertical flow-in of soft sediment (Fig. 1i, d) and, when coupled with core expansion, can cause wash-out and deletion of internal structure of an ash bed (Fig. 1k). These effects must be recorded in detail in core descriptions to allow accurate interpretations of the tephra horizon's morphology to be made (Jutzeler *et al.* 2014*b*).

Primary volcanic emplacement processes

Submarine ash deposits from subaerial fallout

Ash settling out of the ash cloud. The 15 June 1991 Pinatubo Plinian eruption offered the opportunity to compare satellite observations and field measurements. The Plinian eruption column rose to 40 km height within one hour (at 14:41, Fig. 8), then fluctuated between 35 and 30 km for about 4 h (until *c.* 20:41, Fig. 8), then settled to <30 km and finally declined towards the tropopause (*c.* 17 km) during early morning of 16 June (visible and IR satellite observations; Holasek *et al.* 1996). Holasek *et al.* (1996) attributed the decline in height to decreasing eruption mass flux but Rosi *et al.* (2001) attribute it to the gradual change from convective Plinian to collapsing ignimbrite-forming eruption column. The umbrella cloud mapped in Figure 8 is that of the climactic Plinian phase that was driven by stratospheric winds to the SW across the South China Sea where it covered an area of 300 000 km^2 after 5 h and >1 000 000 km^2 after 12 h (Fig. 8; Holasek *et al.* 1996). The southwestward dispersed normally graded Plinian fallout was interspersed by intraplinian ash from pyroclastic surges (Rosi *et al.* 2001). From about 16:40 the eruption reached a phase of entirely collapsing column and ignimbrite production for about 2.5 h. The convective co-ignimbrite ash cloud reached about 30 km height (Rosi *et al.* 2001). By the time of the summit caldera collapse (about 19:11), the vast majority of tephra had been emplaced although the eruption continued into 16 June and ash emissions lasted for weeks.

Isopach and isopleth mapping of the proximal Plinian fallout (Paladio-Melosantos *et al.* 1996;

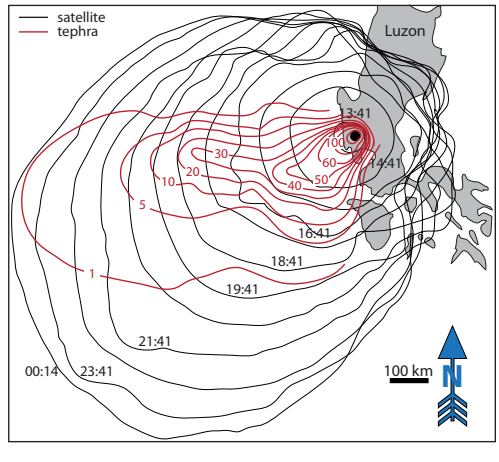

Fig. 8. Lateral spreading of the Mt Pinatubo 15 June 1991 ash cloud of the climactic Plinian phase as observed by satellite and the lateral distribution of the tephra from the total eruption duration. Black contours redrawn from Holasek *et al.* (1996, fig. 5b, courtesy of John Wiley and Sons) show ash cloud shapes at the indicated times on June 15. Red lines are isopachs (thickness in cm) of the June 15 tephra redrawn from Wiesner *et al.* (2004, fig. 1), by permission from Springer Nature, © 2004.

Rosi *et al.* 2001) showed a circular distribution that matches the initial shape of the cloud observed by satellite (Fig. 8). The isopach map based on distal marine ash layer thicknesses (Wiesner *et al.* 2004) shows a more strictly westward dispersal than the ash-cloud isochrons from satellite images of the initial climactic phase (Fig. 8). The distal ash is the product of the entire eruption duration and thus includes contributions from both the convective Plinian eruption column and the subsequent co-ignimbrite ash cloud which rose to lower heights. The marine ash comprises a lower, coarser-grained unit I that is dispersed towards the WSW in agreement with Plinian fallout on land and the stratospheric wind direction. The upper, fine-grained unit II probably represents co-ignimbrite ash driven westward by upper-tropospheric winds (cf. Wiesner *et al.* 2004). Typhoon Yunya passed Pinatubo during the eruption and generated strong lower-tropospheric (<5 km height) winds towards the SE and NE, which may be responsible for the asymmetrical southward extension of the fallout fan (Fig. 8; Wiesner *et al.* 2004).

The Pinatubo case illustrates the interplay of the two most important factors that control the lateral distribution of tephra and thereby also its local composition: the mode of eruption such as the change from convective to collapsing eruption column which determined atmospheric height into which erupted ash is injected, and the regionally, temporally and vertically variable wind patterns that drive erupted ash away from the vent at different speeds and to different directions.

Ash dispersal from relatively low eruption columns is particularly controlled by tropospheric winds that are temporally and vertically more variable than stratospheric winds (Papp *et al.* 2005). At the other end of the spectrum, ash distribution from very large-magnitude ($M > 6.5$; $M = \log_{10}(m) - 7$ with erupted magma mass m in kg) eruptions will not be significantly affected by wind at all (Baines and Sparks 2005; Mahony *et al.* 2016). The almost circular distribution of the ash from the $M = 8.2$ Los Chocoyos eruption (Atitlan Caldera, Guatemala) is an illustrative example (Kutterolf *et al.* 2016; Cisneros de Leon *et al.* 2021).

Ash settling in the ocean. The settling velocities in water of ash particles in the size range typical of marine tephras are shown in Figure 9a.

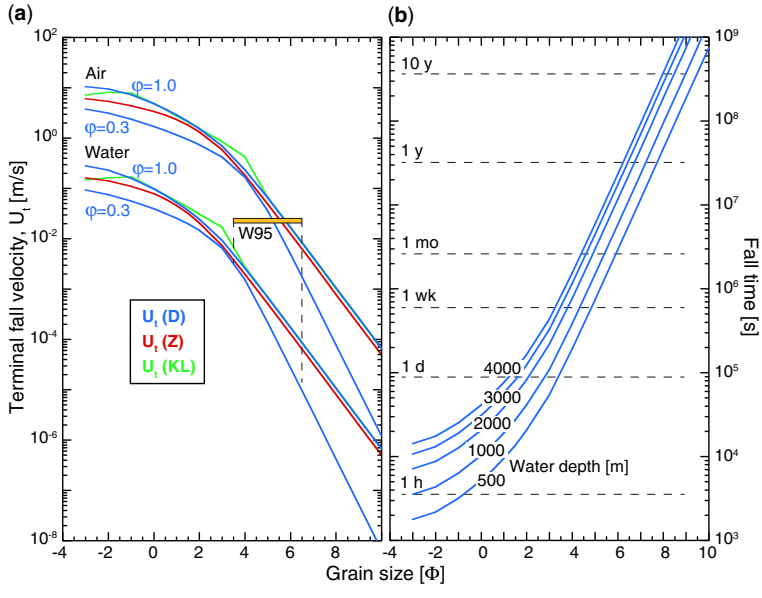

Fig. 9. (**a**) Terminal fall velocities of particles through air and water, calculated for spherical particles after Kunii and Levenspiel (1969) (U_t KL), Zhiyao *et al.* (2008) (U_t Z), and for spherical (shape factor $\varphi = 1$) and irregular ($\varphi = 0.5$) particles after Dioguardi *et al.* (2018) (U_t *D*). Yellow bar (W95) indicates settling velocity of Pinatubo ash with 3.5 and 6.5 Φ modes as recorded by sediment traps (Wiesner *et al.* 1995). The density of pumiceous ash is 2300 kg m^{-3} for particles smaller than +3 Φ dry 500 kg m^{-3} in air and soaked 1300 kg m^{-3} in water for particles larger than −3 Φ, and linearly interpolated over Φ in-between, approximating the sigmoidal distribution of Eychenne and Le Pennec (2012). Although we mostly assume spherical particles here for convenience, we emphasize that irregular particles only reach about 50% (at −2 Φ) to 2% (at +9 Φ) of the fall speed of spherical particles. (**b**) Particle settling times to the seafloor (at 500 to 4000 m depths) using U_t (*D*).

Corresponding settling times in the ocean range from around 1 hour to several years with decreasing grain size (Fig. 9b). Ocean currents of 0.2 m s^{-1} in the Ekman layer (0–100 m) and average 0.004 m s^{-1} at deeper levels, can then laterally displace particles coarser than 2 Φ by less than 1 km but particles finer than 6 Φ by >100 km (e.g. Ninkovich and Shackleton 1975; Carter *et al.* 1995; Wallrabe-Adams and Lackschewitz 2003). Such lateral displacement would be most efficient in regions with very strong currents as exemplified by Ninkovich and Shackleton (1975).

Marine ash beds often show a gradual transition at the top into sediment mixed with ash over several centimetres height. This is, however, not a result of synchronous slow settling of fine ash and pelagic sediment because (a) the mixture also contains medium to coarse ash (Fig. 7) and (b) (hemi-)pelagic sedimentation rates are commonly too slow to generate observed mixed-sediment thicknesses over the time of fine-ash sinking (typically, 5 cm ky^{-1}, can reach 10 cm ky^{-1} on oceanic plate close to a trench and may reach 100 cm ky^{-1} on continental slopes; Eisma and Passchier 1978; Kohn and Glasby 1978; Marquez *et al.* 1999; Kutterolf *et al.* 2008*c*; Schindlbeck *et al.* 2016*b*; Vannucchi *et al.* 2013).

Grain-size dependent settling speeds of individual particles in water (Fig. 9a) will create normal distribution grading of the marine deposit. Grading characteristics of ash layers can be used to determine the sedimentation (=eruption) duration as shown by Ledbetter and Sparks (1979) and Iriyama *et al.* (2018), who deduced eruption durations of 20–27 days and 4–42 days, respectively, from grading of the Los Chocoyos ash (marine Worzel D ash layer) mentioned above. For comparison, the erupted magma mass of 1.53×10^{15} kg (Cisneros de Leon *et al.* 2021) and a column height of 45 km (Metzner *et al.* 2012), which corresponds to *c.* 10^9 kg s^{-1} mass eruption rate (Mastin *et al.* 2009), suggest an eruption duration of about 18 days.

However, natural and experimental observations and theoretical considerations have challenged the assumption of individual particle settling in the formation of marine ash beds (Bradley 1965). One example observation is that the sedimentation rate of Pinatubo ash of about 2.2 cm s^{-1}, measured by sediment traps (Wiesner *et al.* 1995), was much faster than the individual grain settling speed of the median grain size (5.8 Φ; Fig. 9a). Moreover, there was no significant lateral displacement of the fine ash by ocean currents which would be expected if the fine particles sank individually to the up to 4500 m deep seafloor (Wiesner *et al.* 2004; cf. Figs 8 & 9b). Ash particles fall through air at about two orders of magnitude higher speed than they sink in water (Fig. 9a) due to the huge ambient density and viscosity jump at the sea surface. Hence particles accumulate in a layer at the ocean surface (Carey 1997) which eventually exceeds a critical thickness, H_{cr}, (a function of particle concentration and, hence, of volume flux V_p and grain size d_p), and 'finger' instabilities at the lower boundary form downward-flowing sediment plumes if the ratio, B_{vi}, of the timescale of individual particles settling to the timescale of collective settling in a plume is $B_{vi} > 1$ (Bradley 1965; Carey 1997; Hoyal *et al.* 1999). Here we follow Jacobs *et al.* (2015) in defining the parameters B_{vi} (their eqn 7) and H_{cr} (their eqn 16). Faster-sinking coarser particles achieve less concentration and thus need higher H_{cr}, while very slowly sinking fine particles achieve high concentrations and thus need lower H_{cr} for fingering. However, even within the condition $B_{vi} > 1$, calculated solutions for V_p–d_p pairs can yield physically meaningless results such as H_{cr} approaching d_p or H_{cr} exceeding ocean depth. While H_{cr} of a few centimetres or less can be observed in laboratory experiments, such thin surface layers will perpetually be disturbed and mixed by wave action in the ocean and the corresponding tiny and very slow plumes are unlikely to stay intact while sinking to the seafloor. We thus consider the range $0.1 < H_{cr} < 1000$ m to represent plausible solutions. Figure 10a shows the V_p and d_p values that support this H_{cr} range, which is typically realized by intermediate grain sizes (about 3 to 6 Φ) in the observed tephra data from magnitude M1.3 to 7.9 eruptions while the coarsest and finest grain-size fractions yield unrealistically large and small H_{cr} values, respectively. The initial finger or plume velocity, U_f, increases with volume flux V_p, grain size d_p, and surface layer depth H_{cr} (Fig. 10b). Observed tephra data that satisfy $B_{vi} > 1$ and $0.1 < H_{cr} < 1000$ m, U_f values lie in the range of about 0.003 to 0.05 m s^{-1} (Fig. 10b), which includes the only known measured value of 0.022 m s^{-1} from the Pinatubo 1991 eruption (Wiesner *et al.* 1995). For comparison, ash plumes from eruption clouds sink at about 1 m s^{-1} (Manzella *et al.* 2015). The time t_{cr} needed to build up a surface layer to depth $0.1 < H_{cr} < 1000$ m typically takes a few minutes to a few hours, it decreases with volume flux V_p and grain size d_p but increases with H_{cr} (Fig. 10c). It should be noted that the results shown here have been obtained for single grain sizes, implicitly assuming that the median grain size controls the settling behaviour. However, experiments with two mixed grain sizes show more complex behaviour (Jacobs *et al.* 2015) and indicate that the settling of natural polydisperse ash will be even more complex.

One consequence of plume sedimentation is that coarse and fine ash collectively sink to the ocean floor so that size separation (and drifting away of the fines) are inhibited (Fig. 4b, c). The presence of a significant fraction of fine ash in marine tephra beds has therefore been attributed to plume

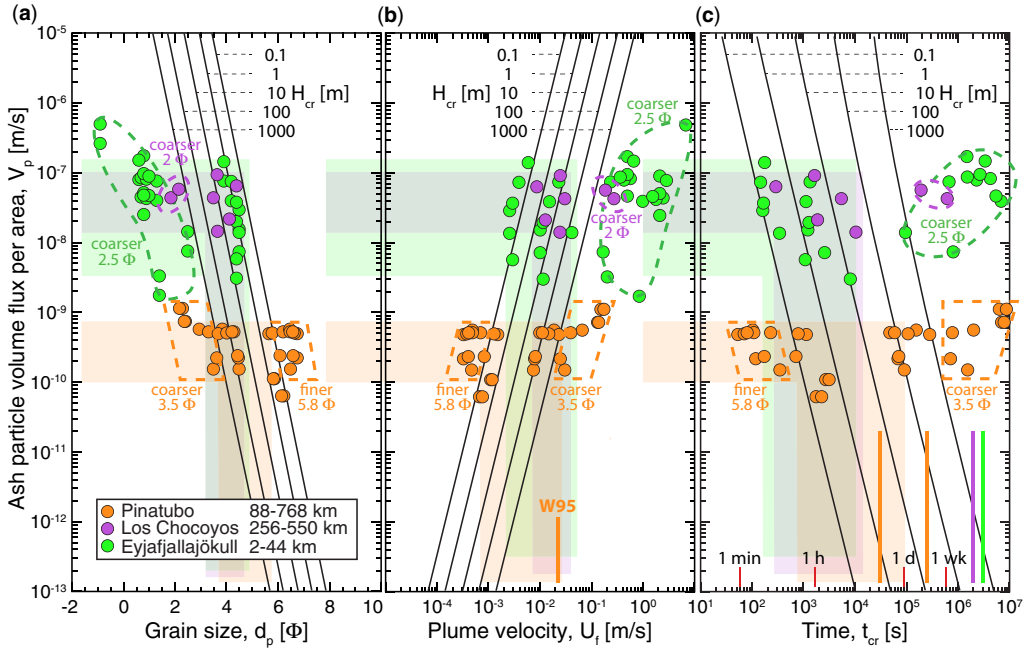

Fig. 10. (**a**) Particle volume flux V_p onto the ocean surface v. grain size d_p for the range of critical depths H_{cr} of the surface, calculated with eqn 16 of Jacobs *et al.* (2015) using $U_t(Z)$ from Figure 9. Application to tephra grain sizes and volume fluxes observed over the distance ranges given in the legend yield H_{cr} values outside the range $0.1 < H_{cr} < 1000$ m for the coarsest and the finest grain-size fractions while intermediate grain sizes yield plausible H_{cr} values. (**b**) Particle volume flux v. initial finger or plume velocity U_f for the range of indicated H_{cr} values, calculated after Manzella *et al.* (2015) and Scollo *et al.* (2017) assuming H_{cr} as scale of finger dimension (Hoyal *et al.* 1999). For the tephra data, velocity values compatible with the H_{cr} range lie between 10^{-3} and 10^{-1} m s^{-1}; this range also includes the rate measured by Wiesner *et al.* (1995) (orange bar W95 = 0.022 m s^{-1}). (**c**) Particle volume flux v. the time t_{cr} required to build up the surface layer to a depth H_{cr}. Colour-coded bars indicate the duration of eruption for the example tephras, the two bars for Pinatubo are the 9 h duration of the climactic phase and the 3 days duration when precursory eruptions from 12–14 June 1991 are included. Tephra data: Eyjafjallajökull 2010, Iceland, calculated for particle densities 1443 and 2738 kg m^{-3}, magnitude M1.3, duration 37 days, Bonadonna *et al.* (2011); Los Chocoyos Tephra, Guatemala, particle density as in Figure 9, M8.2, duration ≥20 days, Cisneros de Leon *et al.* (2021); Mt Pinatubo 15 June 1991, Philippines, M6.1, particle density 2340 kg m^{-3}, median, coarse mode and fine mode grain sizes are considered separately, Wiesner *et al.* (1995, 2004).

sedimentation (Wiesner *et al.* 2004; Kandlbauer *et al.* 2013) but requires fine-ash deposition on the sea surface in the first place, either due to ash aggregation or to plumes descending from the ash cloud. The formation of ash plumes sinking from laterally drifting ash clouds requires a relative abundance of fine ash (Scollo *et al.* 2017). Carazzo and Jellinek (2012) modelled plume settling from observational data and found that at least 6 out of the 16 phreatomagmatic, vulcanian and Plinian eruptions investigated had been able to form fingers and plumes. Kandlbauer *et al.* (2013) interpreted the continuity in grain-size distributions of the 1815 Tambora distal ash across the land–sea border to support deposition by ash plumes descending through the air and in the sea. Manzella *et al.* (2015) demonstrated that both processes, descending ash plumes and ash aggregation, played important roles in deposition of the Eyjafjallajökull 2010 tephra.

Ash settling on the seafloor. Sediment plumes descending through the density-stratified ocean at velocities of a few cm s^{-1} can cross density boundaries or may temporarily stall and spread laterally at levels of neutral buoyancy until increasing particle concentration generates new fingering (Carey 1997). They may also mix with seawater if the Richardson Number $\mathrm{Ri} = g' \times H_{cr} \times U_f^{-2}$ becomes $\mathrm{Ri} < 1$, using H_{cr} as scale of the plume dimension (Hoyal *et al.* 1999). With finger/plume speed $U_f = O(10^{-2}$ m s$^{-1})$ and $g' = O(10^{-5}$–$10^{-6})$, the condition $\mathrm{Ri} < 1$ would be met by $H_{cr} < 10$–100 m (cf. Fig. 10a). One consequence of such mixing with seawater can be the entrainment of planktonic foraminifera

(see the subsection 'Ash particles' in the first section). Since mixing with seawater decreases negative buoyancy the initial plume velocity (Fig. 10b) will probably be a maximum estimate of the velocity with which a sediment plume impinges on the seafloor, where it will spread laterally as a density current (Manville and Wilson 2004), further decreasing particle concentration by sedimentation and increasing fluid drag (Lüthi 1981). Assuming that the initial horizontal density current velocity equals the initial vertical plume velocity (<0.05 m s^{-1} from Fig. 10b), the basal shear stress would be lower than the critical shear stress needed to initiate motion of median particle sizes finer than about 1–2 Φ (calculated after van Rijn 2012; see also Komar and Clemens 1986; van den Berg and van Gelder 1993), the size range corresponding to 'realistic' conditions of plume formation (Fig. 10a). Suspension sedimentation would further reduce the chance for bed-load transport (Lowe 1988; Kubo and Nakajima 2002; Koller *et al.* 2017). These plume-derived currents are thus unlikely to generate an ash deposit with tractional bed-load structure or to erode cohesive muddy sediment which requires still larger shear stresses (van Rijn 2020). With the possible exception of canyons and steep slopes where the density currents may accumulate and accelerate (Parker 1982), we conclude that plume-derived volcaniclastic density currents of fallout ash will typically not be erosive or form cross-bedded deposits on flat seafloor. Plume spreading on the flat seafloor thus cannot introduce ripped-up (bio-)clasts into an ash fallout deposit. Gradual suspension sedimentation will rather form a normally distribution-graded deposit (Manville and Wilson 2004) that is not easily distinguished from a deposit formed by individual grain settling.

One consequence of spatially separate sinking ash plumes can be inconsistency in the lateral thickness distribution of ash on the seafloor (Manville and Wilson 2004). However, numerous closely spaced fingers will form as long as particle flux generates a sufficient particle concentration in the surface layer (Scollo *et al.* 2017). Therefore, an eruption duration that allows for several cycles of surface layer build-up and plume formation (Fig. 10c) with random changes in finger positions will cancel out differences in spatial distribution of ash on the seafloor. Interference between closely neighbouring fingers may also inhibit systematic grading in the deposit. A series of ash plumes sinking to the same spot on the seafloor may generate a deposit consisting of several normally graded layers but so far, such bed-sets have not been unambiguously identified as fallout but are known from much more powerful, repeated turbidity current pulses (Fig. 5). *In situ* observations of submarine fallout emplacement would clearly be essential to substantiate such speculations.

Submarine ash deposits from subaerial pyroclastic density currents

Volcaniclastic turbidites. While almost intact pyroclastic flow deposits can be preserved in shallow water (e.g. 40 m deep flat seafloor around Krakatau, see the subsection 'Ash turbidites' in the first section), on steeper submarine slopes and in deep waters volcaniclastic turbidites are the typical submarine equivalent of ignimbrites on land. The 30 ka Roseau ignimbrite on Dominica (West Indies), which comprises two flow units, has submarine turbidite equivalents that have locally highly variable internal structures and grading patterns suggesting emplacement by several smaller events, possibly related to pyroclastic flows reaching the sea at two distinct locations (Whitham 1989). Finer grain size, better sorting, and higher crystal/lithic ratios of the volcaniclastic turbidites are attributed to fragmentation of hot juvenile clasts upon contact with cold sea water (Whitham 1989). The presence of hemipelagic mud and minor bioclasts as well as mud clasts indicate submarine erosion by the turbidity currents. At Montserrat, West Indies, six of the block-and-ash flows generated during the 1995–2006 dome collapses entered the sea, very rapidly mixed with seawater, proximally lost their coarse load as granular flow lobes, and formed ash-loaded density currents that travelled to >30 km from source (Herd *et al.* 2005; Trofimovs *et al.* 2006). The proximal turbidites are composed of massive, well-sorted sand, with basal reverse grading reflecting a waxing current and normal grading at top reflecting a waning current controlled by the waxing and waning collapse activity at the dome (Trofimovs *et al.* 2008). The turbidites contain a few percent entrained bioclasts, have low contents of fine ash, and, with distance, become finer grained and normally graded with planar lamination and occasional cross-bedding (Trofimovs *et al.* 2008). Fine-ash suspended in the seawater settled as a separate layer on each turbidite. A large-scale example are the 1 to 7 m-thick tuffaceous sandstone beds drilled in the Shikoku Basin east of Japan, about 350 km away from their parental caldera-related ignimbrite eruption sites (Schindlbeck *et al.* 2013; Kutterolf *et al.* 2014). These volcaniclastic turbidites range from massive to coarse-tail size and density graded, and contain 57–82% juvenile material (pumice, glass shards, minerals) of homogenous composition in each unit. The lithic content of the turbidites comprises (bio)clasts eroded from the seafloor where these highly energetic turbidity currents descended *c.* 3500 m down the continental slope before continuing for >100 km along near-horizontal seafloor (Schindlbeck *et al.* 2013). Eruption-fed large turbidity currents are thought to be a major process in the formation of erosional-depositional bedforms at the lower flanks of volcanic

islands that have wavelengths of hundreds to thousands of metres and wave heights up to hundreds of metres (Casalbore *et al.* 2021). Such large-scale structures may cause different appearance of the same deposit in different cores.

The above examples stem from unwelded pyroclastic flow deposits but widespread submarine turbidites have also formed where hot flows forming highly welded ignimbrite on land entered the sea (Schmincke and Sumita 1998). An example is the 14 Ma old compositionally zoned rhyolite–trachyte–basalt high-grade ignimbrite P1 that originally covered the entire island of Gran Canaria (Canary Islands, Spain). Its depositing flows entered the ocean in every direction, leaving submarine deposits 86–44 cm thick at 56–68 km distance from shore after descending down the steep slope to about 2000 m depth and travelling about 25 to 50 km on seafloor gradually dipping to >3000 m water depths (Freundt and Schmincke 1998). The juvenile components in the volcaniclastic turbidites are variably vesicular vitric rhyolite and trachyte fragments (mostly altered to clay), aphyric basaltic tachylite particles, and crystals of the P1 phenocryst phases (mainly plagioclase, amphibole, pyroxene). Vitric angular particles with collapsed-pumice textures reflecting viscous welding compaction close to shore occur in the submarine layer but lack any devitrification as on land; the welding process was thus quickly interrupted by quenching and fragmentation (Freundt and Schmincke 1998). Syn-eruptive emplacement of the volcaniclastic turbidite layers is evidenced by (a) upward decreasing content of feldspar crystals but increasing content of basaltic particles, as in the ignimbrite on land, and (b) the absence of intensely devitrified and crystallized fragments and strongly fingerprint-resorbed anorthoclase which would have been included by post-emplacement ignimbrite erosion. While some incipient welding occurred near shore, most of the very hot pyroclastic currents mixed with seawater to form turbidity currents which picked up volcanic lithics and a mixture of shallow-water, benthic and planktonic bioclasts on their way to the >3000 m deep ocean floor.

While the volcaniclastic turbidites typically contain the largest part of the volume of pyroclastic flows entering the sea, substantial volume fractions can be separated during the entry process. A significant fraction of pumice clasts may be segregated into floating rafts (see section 'Submarine ash deposits from floating pumice rafts'). Large volumes of fine ash can be deposited by co-ignimbrite ash clouds and surges over water. For example, the 20 km^3 co-ignimbrite ash that was mainly generated where the pyroclastic flows of the Tambora 1815 eruption entered the Java Sea, spread to >1300 km distance across the sea (Sigurdsson and Carey 1989). As another example, the submarine Campanian Ignimbrite ash layer has a bimodal grain size distribution which comprises about 60% co-ignimbrite ash mixed with Plinian fallout ash (Fig. 4b; Engwell *et al.* 2014). A third example are the dilute hot pyroclastic density currents that detached from the pyroclastic flows entering the sea and travelled up to 80 km over water at >100 km h^{-1} speed during the Krakatau 1883 eruption (see section 'Properties of ash beds'), emplacing several decimetres thick tephra on opposite island shores and killing about 2000 people (Carey *et al.* 1996, 2000).

Interaction and deposition processes. Laboratory-scale experiments with flows of ignimbrite ash entering water illustrate interaction processes controlled by pyroclastic flow temperature and mass as well as by water depth (Freundt 2003). Relatively cool ash flows (<150°C) hitting water on a 26° shore gradient instantly displace water to form a tsunami wave, and mix turbulently with the water in a mixing zone whose near-vertical front gradually extends into the water and then begins to collapse to a turbidity current while the coarsest load drops to the floor (Fig. 11a). During intrusion interstitial air entraining fine ash is expelled upward and forms a dilute ash-cloud surge over water. The largest highly vesicular pumice clasts escape from the mixing zone and float on water until they soak and settle on top of the turbidite on the tank floor. Since pumice rafts have been observed after entry of pyroclastic flows into the sea, we expect that a natural sequence of turbidite capped by sunken raft pumice can be deposited but to our knowledge has not yet been reported. The most proximal floor deposit is a mixture of slumped sediment and turbidite but changes downstream into a normally graded turbidite with a very fine ash top (Fig. 11c). The much more complex behaviour of hot ash flows (>250°C) involves their advance along the water surface and mixing with water across some distance from shoreline, pushing a wave, and forming sinking sediment plumes advanced by the coarsest and densest settling particles (Fig. 11b). Hot pumice remains entrained in the mixing zone as it quickly soaks with water (cf. Whitham and Sparks 1986; Allen *et al.* 2008). The sediment plumes merge into a turbidity current down the tank that contains warm water lighter than ambient water so that, after loss of sufficient sediment, the current lifts up and proceeds under the water surface in a dilute state (in experiments where the tank was long enough). During the mixing process at the water surface, phreatic explosions eject a buoyant fine-ash cloud and an ash fountain that additionally feeds a fast, relatively concentrated ash-cloud surge over water initially formed by air and ash expelled rapidly from the mixing zone. The experimental tank floor deposit is a normally graded turbidite

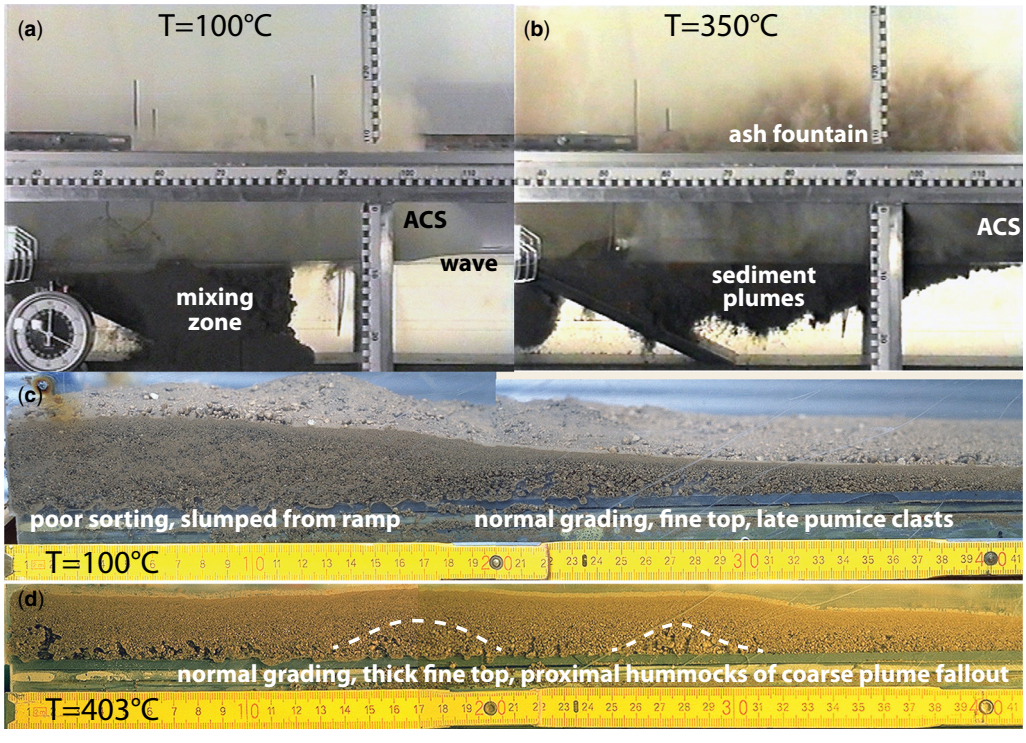

Fig. 11. (**a**) Video snapshot of a cool ash flow entering water tank, forming a dilute ash-cloud surge (ACS) over water and a zone of intense mixing under water with a steep front that just begins to collapse to a turbidity current at its base. (**b**) Video snapshot of a hot run in which the ash flow spreads and mixes along the water surface to then collapse to the tank floor forming a turbidity current. Above the water littoral explosions generate ash fountaining and a relatively dense ACS rapidly moving away from shore. (**c**) Tank floor deposit of a cool run, left edge is the foot of the ramp. Proximal facies chaotic due to slumping from the ramp, turning downstream into normally graded turbidite with very fine ash top covered by former floating pumice lapilli that sunk long after turbidity emplacement. (**d**) Tank floor deposit of a hot run, composed of basal humps of coarse particle fallout from the flow along water surface (see b) overlain by normally graded turbidite with thick fine-ash top layer and low downstream thinning. (a) and (b) reprinted by permission from SpringerNature copyright 2003.

with a relatively thick, fine-grained top zone and a lower gradient of downstream thinning in comparison to the cold runs. This turbidite overlies humps of coarse fallout clasts in a proximal region (Fig. 11d). Cantelli *et al.* (2008) performed further experiments on warm and cold turbidity currents and Dufek and Bergantz (2007) theoretically modelled the thermal interaction processes.

Turbidity currents suspend their particle load by turbulence and can travel far in a self-sustaining state of auto-suspension if the (kinetic and/or potential) energy supplied at least balances that consumed by maintaining the suspension (Bagnold 1962). The current is depositional if it deposits more grains than it entrains, and erosive if it entrains more grains than it deposits (Parker 1982). In the latter case, the current accelerates due to increasing density, hence bed stress and entrainment increase, resulting in a catastrophic current until increased concentration dampens turbulence or reduced bottom slope decelerates the current (Parker 1982). This kind of interaction with the seabed is essential for far-reaching turbidity currents and it also provides one explanation why volcaniclastic turbidites, even if directly resulting from a volcanic event, contain significant amounts of biogenic and other lithic materials (e.g. clay clasts) picked up from the seafloor. Other explanations include separate geological processes such as sediment entrainment during violent near-shore interaction or slope instabilities. In principle, the transport conditions of a turbidity current can be inferred from the bedforms and grain sizes contained in the turbidite (Komar 1985; Chikita 1990). The classical Bouma divisions A through E are interpreted as deposition from a waning turbidity current. The coarsest grains in basal layer A mark the onset of deposition when the current was no longer able to suspend such grains; for example, for 500 μm sand

grains, the current must have decelerated to below *c.* 3 m s^{-1} (Komar 1985). As the current slows further, velocities are just sufficient to move continuously finer grains by traction along the bed, forming upper plane beds (B), cross-stratification (C), lower plane beds (D) and finally layer E as suspension fallout of the finest grains. However, this classical sequence, controlled by grain size and flow power, can be substantially modified by high rates of suspension fallout (Allen 1982; Lowe 1988). With increasing suspended-load fallout rate the stability fields of tractional bedforms shrink and are replaced by direct suspension fallout deposition of a massive bed (see experiments by Arnott and Hand 1989). Zeng and Lowe (1997) modelled the relationships between velocity, concentration and grain size of turbidity currents and confirmed that normal distribution grading results from low-concentration currents while high-concentration currents form massive deposits eventually with coarse-tail grading.

Intense turbulent mixing between pyroclastic flow and water favours the generation of high-concentration turbidity currents (Fig. 11) suggesting that turbidites of such origin would have a massive proximal facies that extends over considerable distance. Large-magnitude explosive eruptions can go on for many hours or days (examples see Fig. 10c) and if the supply of pyroclastic material into the sea is steady, a turbidity current may be formed that remains quasi-steady for a significant period of time, such that steady conditions at its lower boundary lead to aggregation of a thick massive deposit (Kneller and Branney 1995). The up to 7 m thick massive tuffaceous sandstones in the Shikoku Basin reported in the subsection 'Volcaniclastic turbidites' may be a possible example of this (Schindlbeck *et al.* 2013). On the other hand, if the supply of pyroclastic flow into the sea is unsteady, pulses of turbidity currents may generate a pile of turbidite layers (Fig. 5).

Fine ash layers on top of coarser turbidites or at greater distances can have different origins: (a) terminal slow settling of fines from a turbidity current, (b) pyroclastic fallout from Plinian eruption column (as in section 'Submarine ash deposits from subaerial fallout'), from littoral explosions, or from an elevated co-ignimbrite ash cloud, (c) deposition from a pyroclastic density current over water, and (d) late, fine-grained suspension sedimentation from a warm or less saline turbidity current that lifted off the seafloor, forming either more distal ash deposit or fine ash on top of the main turbidity if advected back by opposing shallow ocean currents. These origins are difficult to distinguish because all five types of deposits will be dominated by vitric fine ash. However, unusual thickness, stratification, and the presence of marine bioclasts would favour deposition from volcaniclastic turbidity currents.

Submarine ash deposits from floating pumice rafts

Extensive rafts of densely packed floating pumice have been observed in the ocean as well as in lakes after subaerial and submarine explosive volcanic eruptions. Rafts have formed by submarine eruption columns reaching or breaching the sea surface, by coarse-grained pumice fallout from near-shore vents, and by pyroclastic flows entering the sea, but also by post-eruptive reworking of pumice (e.g. Bertrand *et al.* 2014). Bryan *et al.* (2012) reference 20 volcanic eruptions world-wide that produced pumice rafts over the period 1815 to 2008. The dispersal of the initially >400 km^2 large pumice raft produced by the July 2012 submarine (>700 m bsl) eruption of Havre volcano (Kermadec arc, SW Pacific) has been traced by satellite images, which show raft break-up and transport at 2–17 km per day into different directions by ocean surface currents and eddies to reach a maximum dispersal area of >5 50 000 km^2 with about 400 km radius after three months (Jutzeler *et al.* 2014*a*). A pumice raft originating from a shallow submarine eruption near Tonga in 2001 travelled >3500 km in about one year and, like many other pumice rafts, served as an efficient transport agent of marine biota (Bryan *et al.* 2004). Risso *et al.* (2002) related stranded pumices at Argentine and South Shetland shores to a 1962 eruption at South Sandwich Islands and concluded that the depositing pumice raft must have followed the Antarctic Circumpolar Current around the Antarctic continent for about 20 000 km. Thick rafting pumice was reported to have carried skeletons of victims from Krakatau to the African east coast (*c.* 6000 km) during the year after the 1883 eruption (Winchester 2003). Krakatau 1883 pumice washed ashore at Cocos Atoll in the early 1900s and thus had been drifting for about 20 years (De Vantier 1992). Experimental investigations of pumice soaking confirm that pumice clasts can float for several thousand hours, depending on clast size, shape, porosity and permeability, on temperature when hitting the water, and on rates of gas diffusion in partly water-soaked pumice (Whitham and Sparks 1986; Manville *et al.* 1998; Risso *et al.* 2002; Allen *et al.* 2008; Fauria *et al.* 2017). Sinking of larger clasts later than smaller clasts may generate a reversely graded deposit (saturation grading, White *et al.* 2001) but for rafts drifting in the ocean reverse lateral grading (size increasing with distance) seems more likely. For example, −2 Φ clasts take *c.* 100 h but −5 Φ clasts *c.* 10 000 h to saturate (White *et al.* 2001) and if the pumice raft drifts at ≥2 km/day, the −5 Φ clasts would be deposited >800 km away from the −2 Φ clasts. Reverse vertical grading may be found in terrestrial lakes with limited raft drift (e.g. Manville 2001).

Where vastly outsized rounded pumice clasts lie on top of marine ash beds, these are very likely floating pumice that soaked and sunk. However, practically nothing is known about ash deposits from pumice rafts. As long as particle density of a raft allows clast collisions and friction by wave motion, ash will be generated and settle to the seafloor while the pumice clasts become increasingly rounded. Boats crossing pumice rafts report loud grinding noise attesting to continuous attrition (see and hear Tonga video (2019) for example). We are not aware of any systematic study of pumice comminution in floating rafts but the ash grain size produced by pumice abrasion and comminution in pyroclastic flows is typically 10–100 μm and ash production rate by collisions is proportional to the square of impact velocity while the production rate from friction depends on the velocity of the moving bed (Dufek and Manga 2008). In the pumice raft situation, we would expect frictional abrasion by moderate but continuous wave movements as the dominant mode of ash production unless a raft is hit by severe storm. The change from angular to well-rounded shape of floating pumice requires >30 vol% removal of material (Dufek and Manga 2008). Having achieved such rounding, a stationary 70 cm-thick pumice raft (250 kg m^{-3} bulk density) would have produced a 35 mm-thick ash layer (1500 kg m^{-3}) on the ocean floor, a maximum estimate because in reality the raft would drift. However, this value is similar to the 1–15 mm thickness estimated for ash from the Havre raft (Jutzeler *et al.* 2014*a*). In terms of volume, an initially 1 km^3 pumice raft (Jutzeler *et al.* 2014*a*) would have lost about 0.3 km^3 (*c.* 7.5×10^{10} kg) when abrasion has adequately rounded the pumice. In highly energetic pyroclastic flows with frictional ash production rates ≤0.2 kg m^{-3} s^{-1} (Dufek and Manga 2008) the 0.3 km^3 ash would be formed in 20 minutes but in much less energetic pumice rafts this process will take much longer.

If a continuous ash layer is formed at all, it will most likely be restricted to some proximal region where the pumice raft is still continuous and facilitates intense clast contacts. Such an ash layer may look similar to one formed by distal pyroclastic fallout (fine grain size, relatively well sorted, possibly normally graded). However, we would expect three possible differences: (1) presence of occasional outsized clasts of soaked and sunken pumice, (2) that raft-derived ash preserves the crystal-glass ratio of the pumice because it is not affected by size/density segregation as during other transport processes, and (3) the ash should inherit the practically lithic-free nature of the pumice rafts. However, a detailed study of pumice raft-derived ash deposits still needs to be done.

Submarine ash deposits from submarine eruptions

Ash-size juvenile fragments generated in relatively small-scale, mostly mafic submarine eruptions by explosions in the vent, by thermal quench fragmentation in the water column, or by glass crusts spalling off lava flows are dispersed by turbid density currents to mostly limited distance from vent (Fiske *et al.* 1998; Head and Wilson 2003; Mueller 2003). However, there is also (rare) evidence for deep-water mafic eruptions producing widespread ash layers. The Charles Darwin volcanic field at about 3500 m water depth south of Santo Antão, Cape Verdes, includes craters surrounded by stratified clastic deposits ranging in grain size from ash to blocks (Fig. 12c), evidence of highly fragmenting eruptions. Two sediment gravity cores up to 100 km NW of the volcanic field (Fig. 12a) each contain a thin (1–2 cm) ash layer of blocky glass shards (Fig. 12b) that share the unique nephelinitic composition of the Charles Darwin field. This suggests that far-reaching ash turbidity currents can be generated by such mafic deep-water eruptions although the eruption and transport mechanisms still are subject of ongoing work (T. Kwasnitschka, S. Eisele *et al.*).

Much more commonly, however, widespread ash layers and associated proximal large volumes of pumice are formed by silicic submarine eruptions, many of which are associated with submarine calderas. Typical proximal deposits of such eruptions are huge pumice breccias. At Myojin Knoll caldera, Izu-Bonin arc, 150–200 m thick fines-poor rhyolitic pumice-block deposits were emplaced on the caldera walls rising 500–900 m high above the caldera floor at 1400 m bsl (Fiske *et al.* 2001). The 2012 submarine eruption at Havre caldera emplaced breccia of rhyolitic pumice clasts 30 cm to 9 m in diameter on caldera floor (1500 m bsl) and rim (1000 m bsl; Carey *et al.* 2018). During the 1650 AD explosive submarine eruption of Kolumbo volcano, 7 km NE of Santorini in the Aegean Sea, submarine fallout, pyroclastic density currents and segregation processes during transition from submarine to subaerial plume formed a 250 m-thick stratified succession of rhyolitic highly vesicular (42–74% vesicularity) pumice-rich deposits on the crater walls 505 m bsl, in addition to extensive pumice rafts (Cantner *et al.* 2014). The proximal submarine deposits comprise (a) fallout of relatively well sorted block breccias of slightly rounded pumice and intercalated pumice lapilli beds with sharp contacts and occasionally normal or reverse grading, (b) intercalated centimetre- to decimetre-thick coarse-ash beds presumably emplaced by vertical gravity currents descending along the margin of a plume that breached the sea surface, and (c) massive, poorly sorted sediment gravity current deposits thought to derive

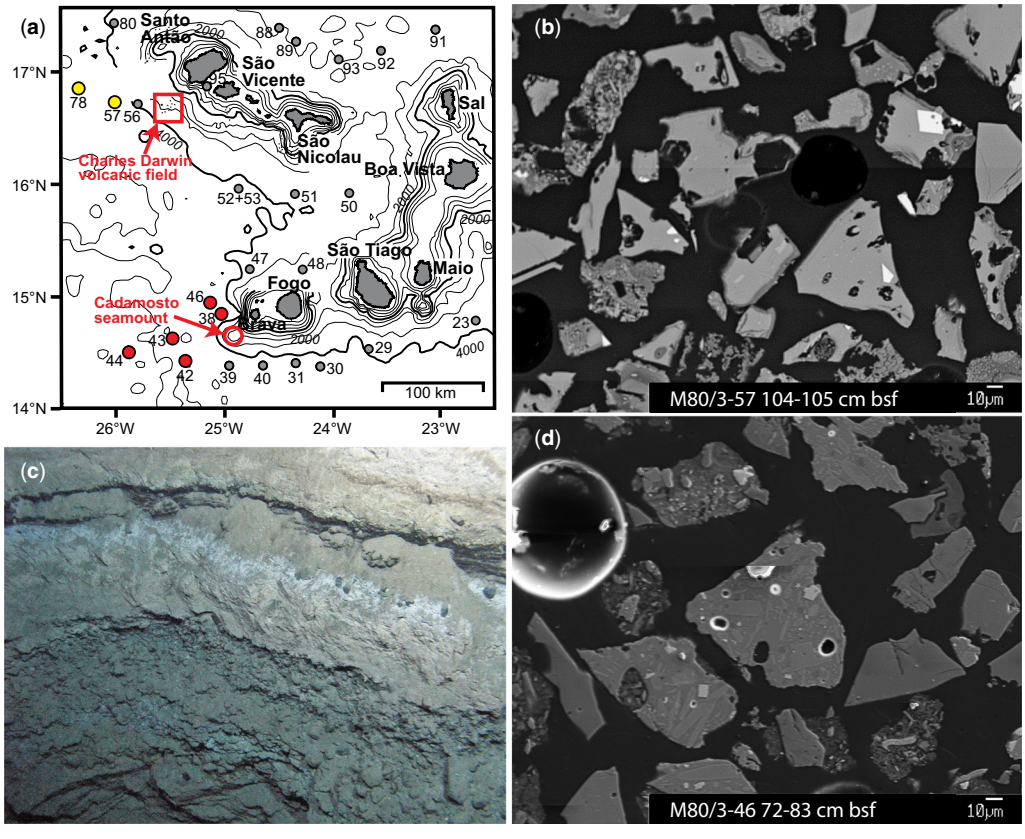

Fig. 12. Cape Verde examples. (**a**) Map of Cape Verde archipelago with gravity core positions (grey dots). Yellow dots are cores containing ash layers derived from the Charles Darwin volcanic field at 3600 m bsl, red dots are cores containing ash from Cadamosto seamount. (**b**) Widespread mafic ash composed of nephelinitic angular glass shards associated with Charles Darwin field deep-sea fragmental volcanism that is evidenced by ROV observations of lapilli and ash beds at crater rims in (**c**). (**d**) Widespread ash layer with phonolitic angular glass shards, many rich in microlites, associated with eruption at lava/dome-dominated Cadamosto seamount. Blocky shards in both cases (b and d) indicate thermal granulation rather than magmatic fragmentation.

from submarine column collapse (Cantner *et al.* 2014). The quick soaking of proximally deposited pumice blocks suggests their derivation from a near-vent high-temperature region (Allen *et al.* 2008; Cas and Simmons 2018).

Ash deposits emplaced inside Havre caldera by the explosive 2012 eruption include a basal coarse-ash layer overlain by a layer of very fine vitric ash emplaced from a buoyant plume and dilute density currents of explosively fragmented ash (Murch *et al.* 2019*a*). The majority of curviplanar shards in the ash is thought to reflect fragmentation by Induced Fuel-Coolant Interaction (IFCI), i.e. a self-accelerating fragmentation process propelled by water intruding thermally or strain-induced fine cracks in the magma (Dürig *et al.* 2020*a*, *b*). About 1/3 of the ash shows features of viscous deformation; Murch *et al.* (2019*b*) interpreted these particles to have deformed viscously while they were still protected from quenching by a steam veil. The marine ash emplaced by the 1650 Kolumbo eruption on the surrounding seafloor to >20 km distance comprises massive and stratified facies and is dominantly composed of vitric particles, followed by crystals and minor lithics (Fuller *et al.* 2018). Maximum grain size decreases away from vent in every direction but bulk grain size distribution does not show a clear relation to distance. Emplacement processes involved subaerial fallout from the northeastward-drifting ash cloud (that reached far into Turkey) but mainly sediment gravity currents derived from submarine and subaerial eruption columns (Fuller *et al.* 2018). In contrast to the deeper-seated Havre eruption, the Kolumbo ash contains a

mixture of shard morphologies (Fig. 3i–o) including the dominant vesicular and shard-shaped ash particles generated by fragmentation driven by magmatic degassing, and a smaller fraction of blocky, poorly vesicular particles formed by explosive magma–water interaction (Fuller *et al.* 2018). The thin ash beds at Kolumbo and Havre contrast with the several metres to tens of metres thick well-sorted marine tephra beds that are normally graded from pebble size at base to silt size at top (Nishimura *et al.* 1992) that have been interpreted as deposits of sediment-gravity currents generated during the huge (*c.* 50 km^3 tephra volume) shallow submarine rhyolitic eruption that formed the 8 × 10 km Sumisu caldera about 70 km away from the drill sites (Tani *et al.* 2008).

Apart from highly explosive eruptions, submarine pyroclastic deposits can also be created by dome-forming activity. Proximal deposits, typically breccias that can be pumice-rich and show quench textures such as radial fractures on blocks, have been described by Allen and McPhie (2000), Mann *et al.* (2004) and Jutzeler *et al.* (2015). Much less is known about more distally emplaced ash beds. The 2012 Havre eruption also produced rhyolitic lava flows and a dome (Ikegami *et al.* 2018). Ash deposits formed during extrusion in and near Havre caldera comprise a lower layer of predominantly tube pumice (Murch *et al.* 2020) and a second layer of mainly microcrystalline particles that were emplaced by syn-extrusive ash-venting and quench-brecciation, respectively (Murch *et al.* 2019*a*). A third layer of mainly microcrystalline ash distributed around the dome with quick radial thinning is interpreted to have formed by gravitational dome collapse. While these deposits remain limited to near-vent regions, Eisele *et al.* (2015*b*) identified two phonolitic ash layers (17 and 40 ka old, 10 and 7 cm thick) in gravity cores up to 70 km to the NW to WSW from their source, Cadamosto seamount at the southwestern tip of the Cape Verde archipelago (Fig. 12a). Limited ROV observations have characterized Cadamosto seamount as an effusive submarine volcano at >1380 m bsl, although a crater structure was also observed. The two phonolitic ash layers are dominantly composed of fine ash of blocky glass shards with few round to slightly elongated vesicles (Fig. 12d), and thus are typical products of thermal granulation upon contact of hot, poorly vesiculated magma with water, rather than products of dominantly magmatic fragmentation as in the caldera examples above. They also differ from the microcrystalline fragments observed at the Havre dome. Eisele *et al.* (2015*b*) proposed that fragmentation during extrusion of lava occurred by water access to deeper parts of the vent in order to inhibit further vesiculation of the volatile-rich magmas before fragmentation.

Distinguishing submarine from subaerial ash sources

Potential criteria to distinguish marine ash layers derived from submarine activity from those derived from subaerial activity include juvenile particle texture and morphology, lithologic composition and grain-size characteristics. A grain-size characteristic important in fallout deposits is hydraulic equivalence, i.e. the association of particles having the same fall velocity. For subaerial fallout settling through air onto the ocean, Cashman and Fiske (1991) determined that the size ratio of gas-filled pumice to lithic clasts that are hydraulically equivalent would have a value of 2 to 3 that would be inherited by the marine deposit as the particles sink to the seafloor. In a submarine eruption generating an ash plume expanding under the water surface, however, pumice would rapidly become water-soaked and its size would be 5 to 10 times that of hydraulically equivalent lithics settling through water. The results of Cashman and Fiske (1991) hold for lapilli-size spherical particles of constant density. However, natural marine tephra beds commonly have finer grain sizes and the density of vesicular juvenile particles increases to smaller grain size (Fig. 9a; Eychenne and Le Pennec 2012). Therefore, the size ratio of hydraulically equivalent juvenile and lithic particles (of same spherical shape) approaches unity towards finer grain size (Fig. 13, case 1a, 1b). Moreover, ash particles are not spherical and grain shape is critical in controlling ash particle settling (Saxby *et al.* 2020). The effect of non-spherical shapes on fall velocity can be quantified according to Dioguardi *et al.* (2018). Thus, if a lithic has much more irregular shape than a pumice of equal fall velocity, its diameter will be larger than that of the pumice (Fig. 13, case 3). Hydraulic equivalence thus is not a practical criterion to distinguish marine ash beds of subaerial and submarine origin.

The vesicle texture of juvenile particles may be a more useful criterion to distinguish submarine from subaerial origin of ash because water pressure may hinder vesicle growth. Rotella *et al.* (2015) proposed a potential fingerprint of pumice erupted in deep water by observing that, due to higher pressure at vent exit (e.g. 10 MPa per 1000 m depth), such pumice has fewer small (<10 μm) bubbles and narrower bubble size distribution compared to pumice of same composition erupted on land. Pumice clasts with quenched margins and/or prismatic joints indicate subaqueous eruption (Allen and Stewart 2003). Abundance of blocky quench fragments (e.g. Fig. 3a, l and m) in widespread marine tephra certainly also argues for submarine eruption, because sufficiently large felsic eruptions on land involving interaction with external water (i.e. phreatoplinian eruptions) typically fragment magma after degassing

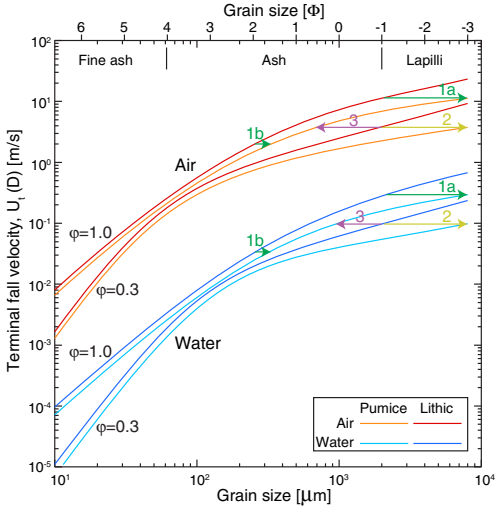

Fig. 13. Particle fall velocity as a function of grain size and grain shape, calculated after Dioguardi *et al.* (2018) for spherical ($\varphi = 1.0$) and irregular ($\varphi = 0.5$) particles. Juvenile particle density varies with grain size as defined in Figure 9a, lithic particle density is set to 2700 kg m^{-3}. Arrows point from lithic to juvenile particle of same fall velocity. For spherical particles, the hydraulically equivalent juvenile/lithic size ratio (green arrows 1) decreases to finer grain size because the density difference decreases. The same applies if both particles share the same irregular shape (yellow arrows 2). However, if pumice is spherical and lithic irregular, the lithic particle can be larger than the juvenile particle of same fall speed (arrows 3).

is almost complete, and hence do not produce significant vesicle-poor quench shards. Many deposits from silicic submarine explosive eruptions have been described as lithic-poor but proximal facies may also include lithic-rich beds, e.g. from a vent-clearing phase (Allen and Stewart 2003). Allen and McPhie (2009) summarize 'Neptunian' eruptions at >200 m water depths as eruption columns that collapse under water in response to rapid mixing with water, thereby emplacing a proximal succession of lithic breccia overlain by pumice breccia, while finer pyroclasts are carried to distance by sediment density currents; accordingly, distal ash turbidites rather than fallout layers will be a common product of deep-water highly explosive eruptions.

The products of emergent volcanism are harder to identify than the clear-cut submarine and subaerial deposits because they can have mixed characteristics from both endmembers. Tephras from emergent eruptions are easiest identified on land where they are bracketed between submarine and subaerial deposits (e.g. Staudigel and Schmincke 1984; Allen and McPhie 2000). In proximal settings, the transition from submarine to subaerial involves increasing abundance of clastic deposits and vesicularity of juvenile particles. Distal deposits of the emergent phase of Gran Canaria are mostly gravity-flow deposits with moderately vesicular juvenile particles (Schmincke and Segschneider 1998). In shallow-water settings, erupting magma is fragmented by magmatic and steam explosions as well as by thermal granulation (Kokelaar 1986) providing a range from dense angular to scoriaceous/pumiceous particles and alternating fallout and flow deposits (Cole *et al.* 2001). Strong phreatomagmatic eruptions in shallow water can excavate the volcanic basement (e.g. Allen and McPhie 2000; Pallister *et al.* 2005) and may thus lead to a relatively high content of (altered) lithics in medial to distal tephra.

Secondary emplacement processes

The investigation of resedimented pyroclastic material is important to better understand how such secondary deposits can be distinguished from primary pyroclastic deposits. Moreover, the reworked facies may contain a significant fraction of the total pyroclastic mass produced by an eruption which should ideally be added to the mass determined from the primary deposits. We define secondary deposits as those that are not directly formed by eruptive processes, which form the primary deposits. We note, however, that this distinction is not always unambiguous as discussed in the section 'Distinguishing primary and secondary ash layers'.

Volcanic landslides

In the last decades bathymetric mapping showed that major landslide deposits are common around volcanic islands worldwide. The collapse of volcanic island flanks can generate extremely large landslides reaching volumes of up to several thousand cubic kilometres (e.g. Nuuanu landslide off Oahu, Hawaiian Islands; Moore *et al.* 1989). For comparison, the subaerial flank collapse that occurred during the 1980 eruption of Mt St Helens had a volume of *c.* 3 km^3 (Sousa and Voight 1995). Major landslides have been identified along the Hawaiian ridge (Moore *et al.* 1989; Moore and Normark 1994), at the Marquesas Islands (Wolfe *et al.* 1994), La Réunion (Labazuy 1996), the Cape Verde Islands (Masson *et al.* 2008), the Lesser Antilles (Deplus *et al.* 2001), the Canary Islands (Krastel *et al.* 2001; Masson *et al.* 2002), Ritter island (Karstens *et al.* 2019, Watt *et al.* 2019) and most recently the collapse of Anak Krakatau (Walter *et al.* 2019). Kokelaar and Romagnoli (1995), Tibaldi (2001) and Di Roberto *et al.* (2010) identified multiple

partial sector collapses in the cubic kilometre-range at the north flank of Stromboli volcano, forming a channel-shaped depression that extends the Sciara del Fuoco to >2200 m below sea-level and generating volcanogenic turbidites found to >50 km away from the volcano.

One major reason why marine landslides are of great scientific interest is their potential to generate catastrophic tsunamis that can cross entire oceans (Ward and Day 2001; McGuire 2006). Yet the risks associated with these events as well as their frequency and relation to magmatic/volcanic activity are still poorly constrained and heavily debated (Boulesteix *et al.* 2012; Watt *et al.* 2012; Hunt *et al.* 2013; Paris *et al.* 2018). Geological observations at Stromboli identified an event sequence of a flank collapse triggering a tsunami and rapidly followed by a prolonged period of explosive volcanic activity (Rosi *et al.* 2019; Pistolesi *et al.* 2020). In another case, however, an explosive eruption immediately preceded a tsunami. At a larger scale, the 165 ka Icod landslide at Tenerife was preceded by a caldera-forming eruption (Hunt *et al.* 2011). The scale of the tsunami risk depends on whether flank collapse occurs catastrophically en masse, potentially forming a megatsunami (e.g. Ramalho *et al.* 2015), or gradually or even in stepwise fashion with reduced tsunami-forming potential (Hunt *et al.* 2011; Paris *et al.* 2011). Geological investigation into the collapse conditions is difficult because the landslide deposits are hard to penetrate both by coring and by seismic surveys. As landslides lose their coarsest load and mix with seawater, they form energetic turbidity currents that can travel to distances >1000 km from source (Garcia and Hull 1994; Hunt *et al.* 2011, 2014). These distal deposits are much easier to sample by drilling and can thus provide information on landslide frequency. On the lower flanks of volcanic islands and across the transition to flat seafloor, such turbidites can often be morphologically recognized by the presence of wavy bedforms on scales from tens to thousands of metres (Casalbore *et al.* 2021).

As an example of complex processes, hydroacoustic measurements and analyses of sediment cores reveal that the *c.* 73 ka Monte Amarelo flank collapse at Fogo, Cape Verdes, which generated a megatsunami (Ramalho *et al.* 2015), likely also triggered the contemporaneous, multi-phase failure of pre-existing seafloor sediments at greater distances east and south of Fogo (Krastel *et al.* 2019; Barrett *et al.* 2020). Moreover, three younger volcaniclastic turbidites recovered in a proximal and a distal core south of Fogo formed by collapse events (Barrett *et al.* 2020; Scheffler 2020; Schenk 2020) constrained to between 21 and 53 ka by comparison with the compositional and chronostratigraphic profiles from neighbouring gravity cores from Eisele *et al.* (2015*b*). The lithologic modal compositions and geochemical glass compositions of the two uppermost, centimetre- to decimetre-thick, volcaniclastic turbidites indicate two different collapse events that tapped more or less the same source area at Fogo volcano within a relatively short time (T2 in Fig. 5d). The older, third volcaniclastic turbidite succession (T1 in Fig. 5d) probably represents smaller, more topographically confined mass transport events from Fogo involving abundant non-volcanic sediment.

Since larger and retrogressive flank collapses can cut through a substantial part of an oceanic volcano's structure, the resulting single, or successions of, turbidites are expected to contain a mixture of volcanic clasts with a wide range of compositions. However, small to moderate collapses can also be restricted to the youngest, compositionally more homogeneous parts of a volcano. For example, the succession of volcaniclastic turbidites derived from collapses at Stromboli can be divided into three glass-shard compositional groups with depth in the gravity core which reflect the compositional changes through three evolutionary stages of Stromboli (Di Roberto *et al.* 2010). The assembly of volcanic clast compositions of a collapse-derived volcaniclastic turbidite thus depends on the age of the collapse relative to the compositional evolution with time and on the position and extent of the collapse relative to the structure of a volcanic island.

Shelf and slope erosion

Volcaniclastic-rich turbidites not formed directly by eruptive activity or by large-scale flank collapse can be generated by erosion at the shelf and upper-slope of a volcanic island or a continental margin close to a volcanic front (e.g. Hikurangi Subduction margin, New Zealand, Hopkins *et al.* 2020). The longer volcanic deposits from different eruptions accumulate on the shelf before getting attacked by erosion, the more heterogeneous the volcaniclastic turbidites will be in their glass geochemical compositions (Schneider *et al.* 2001). Events of shelf erosion can be stochastic (e.g. exceptional storm, earthquakes), forming distinct single turbidites, or erosive conditions can prevail for considerable time (typically climate controlled) resulting in the formation of a fan-like turbidite system (Schneider and Fisher 1996; Schneider *et al.* 2001). Coastal erosion rates are typically high immediately after emplacement of a large stock of easily erodible pyroclastic material and then decrease with time (e.g. Zhao *et al.* 2019). Coastal erosion of pyroclastic deposits by wave action varies with the nature of the deposits. Well-sorted sandy tephra has little strength and is more or less steadily eroded and resedimented by granular flows of limited extent. In contrast,

massive, poorly sorted fines-rich tuff has larger strength and is eroded to near-vertical cliffs which episodically collapse in variably large portions (Allen and Freundt 2006). The collapsed mass mixes with water and the coarsest material drops out to be deposited near shore. The remaining tuff, however, forms a turbidity current that is expected to be more concentrated, faster and extensive the larger the collapsed tuff mass. Resulting turbidites are typically density graded with pumice enriched towards the top and lithics towards the base (Allen and Freundt 2006). In either case, well-established shelfs are rich in bioclasts and organic matter and, in the case of subduction zones or long-lived volcanic islands, other volcaniclastic deposits. If erosional events catch a significant fraction of that shelf material, the resulting volcaniclastic turbidites will be rich in shallow-water bioclasts and sediment as well as potentially containing a variety of glass compositions. They will also preserve significant organic matter that can be analysed as Total Organic carbon (TOC) if rapidly buried (Chang *et al.* 2021).

Outwash from fluvial systems

Where eruptions occur in relatively close proximity to coastal environments, volcanic material can enter the marine system through a network of terrestrial, glacial and fluvial outwash mechanisms. During an eruption, volcanic material will swamp, and possibly block, the terrestrial drainage system (Park and Schmincke 2020). Transport through these systems will likely be slower than the deposition of tephra through fallout, and can emplace tephra upwind from source. For example, the river Rhine has transported pumice granules from Laacher See, Germany, >400 km into the North Sea (Busschers *et al.* 2007). However, a fluvially sourced volcaniclastic turbidite can be identified by very well rounded pumice, terrigenous sediment fragments, and terrestrial sourced micro-flora (e.g. pollen) and fauna (e.g. freshwater species) (Kjær *et al.* 2004). When captured from a range of volcanic sources, the fluvially introduced volcaniclastic material will have a mixed geochemical signature (Hopkins *et al.* 2020). Where organic carbon is preserved in a partly fluvially fed marine volcaniclastic turbidite, carbon isotope analysis can reveal a terrestrial origin (Chang *et al.* 2021).

Ice rafting

In high-latitude regions, particularly during glacial periods, fallout tephra can be emplaced on sea-ice and glaciers which eventually break up and drift until melting allows the ash load to settle to the seafloor. While sea-ice drift is relatively rapid (years to decades), for tephra emplaced on glaciers the period from eruption through calving until emplacement on the seafloor can reach several millennia and potentially induce substantial error in marine tephrochronology (Brendryen *et al.* 2010; Griggs *et al.* 2014). If the ice was exposed to numerous eruptions before break-up, as is typically the case for glaciers, the ice-rafted ash will likely have heterogeneous glass-shard geochemical compositions (Lackschewitz and Wallrabe-Adams 1997; Lacasse *et al.* 1998). Since initial fallout emplacement occurs closer to source but settling to the seafloor happens at potentially much greater distances, the ice-rafted ash will be unusually coarse grained, potentially including lapilli-size dropstones, and it will likely be relatively rich in lithic fragments and crystals (Lacasse *et al.* 1996).

Distinguishing primary and secondary ash layers

Distinguishing between primary and secondary tephra layers is essential for unravelling eruption histories, sources, and event stratigraphy as well as for establishing age models, and calculating sedimentation rates in the marine environment. To do so, different criteria and techniques are applied which cover lithological, sedimentological, and geochemical characteristics as well as visual, numerical and statistical correlation techniques. It should be noted, however, that even using this range of techniques it can be difficult to confidently define what is a primary v. a secondary deposit. For example, when transient deposits are formed by a pyroclastic flow entering the sea, and then are quickly remobilized, are the final submarine deposits then primary or secondary? Here, we would identify them as primary because they would show primary characteristics as discussed below, but this decision might well be discussed.

In rare cases one criterion alone (e.g. geochemistry) is sufficient to distinguish between primary and secondary, and fall and flow deposits, but the combination of lithological, sedimentological, and geochemical characteristics leads to less ambiguous interpretations (e.g. Gudmundsdóttir *et al.* 2011; Cassidy *et al.* 2014; Eisele *et al.* 2015*a*). Misinterpretation can lead to substantial errors, for example, marine ash beds having the grain size, texture and homogeneous phonolitic glass composition of the *c.* 107 ka old CGII tephra on Santo Antão, Cape Verdes, occur repeatedly in marine sediments over a thickness interval of up to 5 m above the primary CGII marine tephra (Eisele *et al.* 2015*a*). Mistaking one of these layers for the primary bed would easily introduce an age error of up to 80 000 years into the chronostratigraphy.

Lithological composition

The lithological composition is an elementary aspect to distinguish between primary and secondary tephra deposits and fall and flow processes. Visual inspection of the core, point counting and image analysis of smear slides or thin sections can quantify the relative abundance of the lithologic components (e.g. Gudmundsdóttir *et al.* 2011; Schindlbeck *et al.* 2013). The predominance of juvenile particles (glass and magmatic minerals) would be an argument in favour of a primary fall or flow deposit. A large fraction of non-volcanic clasts, subaerially weathered or altered (volcanic) clasts, and particularly of shallow-water bioclasts characterises secondary turbidites. The significance of hydrothermally altered volcanic lithics is ambiguous as they can be introduced by an eruption as well as by an eruption-independent collapse possibly facilitated by hydrothermally weakened rocks (e.g. Kerle *et al.* 2003). Critelli and Ingersoll (1995) used the relative abundance of neovolcanic grains (glass, fresh minerals, fragments of equal chemical composition) v. palaeovolcanic grains (rounded, altered, same grain size as non-volcanic detritus) and non-volcanic fragments to distinguish syn-eruptive, inter-eruptive and pre-/post-eruptive volcaniclastic sandstones. However, these lithologic criteria can be ambiguous. For example, pyroclastic flows on land and the primary turbidity currents into which they turn under water, but also secondary turbidity currents unrelated to an eruption, can be erosive and thus pick up significant fractions of lithics along their subaerial and submarine paths.

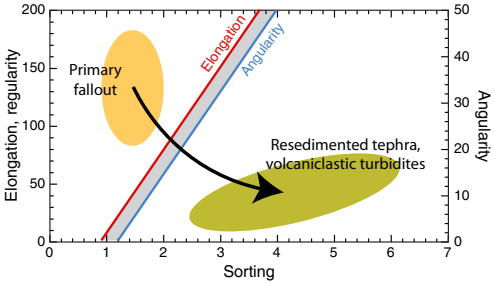

Fig. 14. Particle and bed characteristics that can be used to distinguish primary tephra from resedimented volcaniclastic deposits. Particle elongation or regularity measured as aspect ratio/area, particle angularity measured as perimeter/area, and sorting is determined from the frequency distribution of particle areas. Aspect ratio of long to short axis, perimeter length and particle cross-sectional area are determined by 2D image analysis. High values of angularity and elongation associated with good sorting characterize primary fallout tephra while secondary transport processes make particles rounder and mix a range of grain sizes to produce poorer sorting. Simplified after Cassidy *et al.* (2014).

Sediment structure and texture

Erosive basal contacts and wavy or cross-bedding of volcaniclastic deposits are clear indicators of deposition from a density current whereas marine fallout layers are typically massive with a sharp planar base but may occasionally be planar stratified. Ash-bed structures are commonly observed in 2D core cuts but can be visualized in 3D by X-ray computed micro-tomography (μCT) scanning (Griggs *et al.* 2015). Bouma facies occur in volcaniclastic as in other turbidites and include massive and normally graded facies that cannot always be distinguished from massive or normally graded fallout deposits. Grain-size distribution and grain-size sorting are also important criteria. Fall deposits in a marine environment are commonly well-sorted, whereas flow deposits are commonly poorly sorted (Fig. 14). This is particularly the case with secondary turbidites that have admixed and dispersed pelagic clay (Schindlbeck *et al.* 2013; Cassidy *et al.* 2014; Eisele *et al.* 2015*b*; Jutzeler *et al.* 2017; Hopkins *et al.* 2020). Moreover, fall deposits mostly have unimodal grain-size distributions while turbidity current deposits tend to be polymodal, partly due to the addition of eroded sediment. However, these criteria are ambiguous; suspension fallout from turbidity currents can be relatively well sorted, normally graded and have unimodal size distribution, and can thus be difficult to distinguish from fallout. On the other hand, ash fallout can be bimodal and, hence, less well sorted due to ash aggregation in, or plume sedimentation from, the drifting ash cloud (see the subsection 'Ash settling in the ocean', Fig. 4c), due to an eruption column strongly pulsating in height, or due to ash contributions from different eruption phases such as Plinian and co-ignimbrite ash clouds (e.g. the Pinatubo 1991 and Campanian Ignimbrite examples in Fig. 4b, c).

Particle morphology

Another critical aspect for distinguishing primary from secondary deposits is the morphology of the grains that is observed petrographically, but best quantified by image analysis software (e.g. Cioni *et al.* 2008; Cassidy *et al.* 2014; Eisele *et al.* 2015*b*; Jutzeler *et al.* 2017; Hopkins *et al.* 2020; Chang *et al.* 2021). In volcaniclastic deposits the morphology of juvenile particles is preferentially studied because (a) it is known that they were highly angular when ejected from the vent, and (b) they are mostly more susceptible to abrasion than hard lithic fragments, particularly if highly vesicular. Pyroclastic particles transported by ash clouds and sinking

through the ocean suffer little interparticle contacts and mostly preserve their angularity. They also preserve initial elongated particle shapes but low values of elongation may also mean that an eruption produced mostly equi-dimensional particles. Thus, angular clasts and good size sorting are characteristics of fallout deposits (Fig. 14). Conversely, transport by density currents (both subaerial and submarine) involves frequent intense particle contacts that comminute and abrade the particles leading to less angular, less elongated particle morphologies which, together with poor sorting, characterize resedimented tephra in secondary turbidites (Fig. 14).

Geochemical compositions

Fresh glass compositions. Glass shard compositions are the preferred choice to characterize the degree of compositional homogeneity in volcaniclastic deposits, although mineral compositions can be used additionally but do not provide the same sensitivity. Primary fall and flow deposits are typically characterized by homogeneous glass compositions if the erupted source magma had homogeneous composition. If the erupted magma was compositionally zoned or mixed, the glass compositions reflect a coherent differentiation or mixing trend for all elements. For example, the compositional range observed in the proximal deposits from the 1912 Novarupta eruption, Alaska, are mimicked in the glass and mineral compositions of the distal marine tephra (Federman and Scheidegger 1984; Fierstein and Hildreth 1992). Secondary volcaniclastic deposits, on the other hand, being derived from collapse or erosion of larger sections of volcanic stratigraphy, comprise glass compositions that are not immediately genetically related and can have a relatively wide, heterogeneous scatter (Kutterolf *et al.* 2008*a*, 2018; Gudmundsdóttir *et al.* 2011; Schindlbeck *et al.* 2013, 2016*a*, 2018; Eisele *et al.* 2015*b*; Hopkins *et al.* 2017, 2020).

There are a number of issues in using glass chemistry alone to distinguish primary from secondary ash deposits. There are no predetermined rules for what exactly 'homogeneous' or 'heterogeneous' means, and the useful boundary between these characteristics can vary with the nature of eruption (magmatic v. phreatomagmatic, complex nature of magma reservoir zonation, tapping of different reservoirs). For example, eruptions can tap two or more magma chambers simultaneously and the respective glass compositions are found mixed in the tephra (e.g. Okataina, New Zealand, Shane *et al.* 2008; Lonquimay, Chile, Gilbert *et al.* 2012). In rare cases, such mixed tephra can also form when two vents with distinct geochemical signatures erupt simultaneously and combine into a mixed downwind plume (e.g. Campi Flegrei, Pistolesi *et al.* 2016; Rabaul, Blong 1994). Glass compositional populations can also vary laterally in widely dispersed tephra (e.g. Pearce *et al.* 2020). Moreover, primary fallout can contain older glass eroded from conduit walls and pyroclastic flows can entrain older glass from surface deposits.

Conversely, secondary volcaniclastic deposits can have a very homogeneous glass composition if they tapped just one primary pyroclastic reservoir, particularly if that homogeneous source tephra has a huge volume. For example, in the Santo Antão case (mentioned at the beginning of this section), multiple repetition of homogeneously composed phonolitic ash beds separated by marine sediments occurs above the primary marine ash bed of that tephra, implying episodic erosional tapping of only that voluminous tephra on land (Eisele *et al.* 2015*a*, fig. 7).

There are analytical problems as well. Glass composition can vary on scales of tens of micrometres due to concentration gradients away from phenocrysts (Pearce *et al.* 2002) and variable contents of microlites in the glass shards can produce a range of glass compositions (e.g. Cashman 1992; Sparks *et al.* 2000). The number of analyses per ash bed (possibly limited by measurable shards/minerals or by lab time) might not be representative of the true glass or mineral compositional range. Partial alteration of glass shards can also introduce some heterogeneity in the compositional data (see below). All these uncertainties emphasize the need to use other parameters as well in distinguishing primary from secondary ash layers (e.g. particle shape, Cassidy *et al.* 2014; Chang *et al.* 2021).

Alteration of glass. When interpreting geochemical compositions particularly of older tephras, or tephras in more chemically aggressive environments, it needs to be considered that these compositions can have been modified by alteration (e.g. Kutterolf *et al.* 2007; Lowe *et al.* 2017). Ash alteration is commonly further evolved in mafic than in felsic ash layers, such that unaltered glass in felsic ash may coexist with mafic ash in which glass is distinctly altered and contains secondary mineralisation (Schacht *et al.* 2010). The observation that the fraction of shards that are altered at their rims increases with age and depth of burial of mafic marine ash beds also attests to their vulnerability for alteration. Strong chemical ash alteration is commonly identified in deeply buried sediments (>100 m), where tephra deposited some tens of millions of years ago is degraded to smectite and clays, and pore waters are enriched in dissolved Ca and Si, but depleted in Na, K and Mg relative to the bottom water (e.g. Gieskes and Lawrence 1981; Mottl 1989) in response to the alteration of volcanic glass (Schacht *et al.* 2008). Secondary mineralization then includes

palagonite (Bonatti 1965; Stroncik and Schmincke 2002) or carbonates, zeolites, and phyllosilicates that can form in vesicles or fractures in the glass (Fisk and McLoughlin 2013) such that pseudomorph mineralization can preserve original particle textures (Smith 1991; Freundt and Schmincke 1998).

In shallow cores (≤8 m length), Schacht *et al.* (2008) observed little evidence for major-element changes in glass and pore water chemistry which they attributed to alteration processes operating very slowly (in fact, natural alteration rates appear to be three orders of magnitudes slower than in laboratory studies at similar conditions). However, Gatti *et al.* (2014) report *c.* 11% differences in Na_2O/K_2O in Young Toba Tuff (*c.* 74 ka) marine glass shards buried 1–10 m deep below seafloor, probably related to seawater-induced alkali migration. Schacht *et al.* (2010) observed mobilization of some rare-earth elements (La, Ce) from volcanic glass into pore water in sediments ≤11 m below seafloor.

Tephra correlation

In the marine environment, where drill cores provide only 1D information on tephras, it is even more important to stratigraphically correlate cores, and particularly single ash layers, in order to obtain 3D and eventually 4D information. Moreover, stratigraphic correlations with source volcanoes are essential to bridge the land–sea gap and connect proximal and distal tephra facies. The most common tool for such correlations is the so-called 'geochemical finger-printing' technique (e.g. Kutterolf *et al.* 2008*a*, 2016; Lowe 2011; Ponomareva *et al.* 2015*a*, *b*; Schindlbeck *et al.* 2016*a*, 2018; Lowe *et al.* 2017; Derkachev *et al.* 2020; Rutledal *et al.* 2020; Wulf *et al.* 2020) commonly using glass-shard compositions, occasionally mineral compositions (Shane 1998; Sell and Samson 2011), and even melt-inclusion compositions (Matsu'ura *et al.* 2011). Geochemical fingerprinting is based on the experience that most volcanoes and their eruption products possess fairly unique geochemical compositions of bulk rock and particularly of glass, if not in major then in trace elements (e.g. Kutterolf *et al.* 2008*a*; Okuno *et al.* 2011; Lim *et al.* 2013). Of course, such geochemical correlation should always be combined with petrographic observations (mineral assemblage, juvenile particle morphology) and must be performed in conjunction with stratigraphic, palaeoenvironmental (sometimes archaeological), and chronological criteria (Lowe 2011). This is even more important in regions where tephra geochemical compositions are not sufficiently unique (e.g. Hopkins *et al.* 2017). Then petrographic observation of features that may vary with eruption style, vent conditions and magmatic volatile contents may be helpful, such as vesicle textures, particle morphology or the coexistence of pumice and obsidian (e.g. Cioni *et al.* 2008).

Glass-geochemical correlations can suffer from several potential limitations. One is the chemical alteration of glass as discussed above, which may affect major and trace element concentrations, however, some fluid immobile trace elements such as the high field strength elements Ti, Zr, Y, and Nb (Pearce and Norry 1979; Clift and Blusztajn 1999; Pearce *et al.* 1999) can still be used for correlation purposes. If strong changes in wind direction occurred during explosive eruptions of compositionally zoned magmas distal ash at a given direction from source may contain only a small fraction of the entire compositional spectrum of the eruption (e.g. Bogaard and Schmincke 1985; Shane *et al.* 2008). If erupted component magmas and their glasses and minerals have different densities or were fragmented to different grain sizes and shapes, these components can become segregated during aeolian transport so that, again, distal ash reflects only part of the original magma composition (e.g. Pearce *et al.* 2020).

Major-element concentrations in glass shards and minerals are most commonly measured by electron microprobe (EMP) spot analyses while trace-element concentrations are determined by laser ablation inductively coupled plasma mass spectrometry (LA-ICP-MS) or by secondary-ion mass spectrometry (SIMS, ion probe). Each analytical method has its own analytical uncertainty that varies with the element analysed. For the purpose of correlation, chemical compositions are either compared graphically or by numerical statistical methods (see review by Lowe *et al.* 2017).

Graphical geochemical correlation

The comparison of geochemical data in bi- or trivariate plots of oxide or element concentrations or concentration ratios is a common approach in tephrochronology (e.g. Kutterolf *et al.* 2008*a*; Pearce *et al.* 2008; Shane and Wright 2011). Multi-element spidergrams allow comparison of a larger number of elements simultaneously, and 3-dimensional plots, histograms or a scatter plot matrix have also been employed (e.g. Sarna-Wojcicki *et al.* 2000; Lowe *et al.* 2017). The comparison of marine ash compositions with tephras on land requires a comprehensive data base of the land tephras (e.g. Lowe *et al.* 2015; Tomlinson *et al.* 2015; Mahony *et al.* 2020) from which reference fields can be constructed (Fig. 15a). The marine ash data can then be plotted as single points or as averages (with standard deviations) per layer for comparison with those reference fields (Fig. 15a). The best choice of elements or

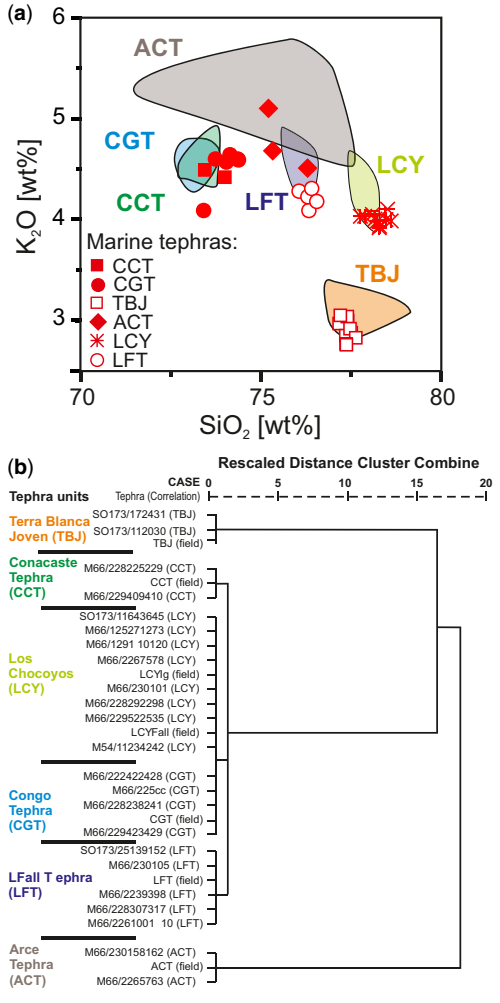

Fig. 15. (**a**) Example of graphical correlation using a K_2O v. SiO_2 diagram. Coloured fields enclose on-land tephra glass compositions. Red symbols for marine tephras from Pacific gravity cores collected offshore Central America are averages of at least 15 glass-shard analyses per ash layer. For tephra acronyms see (b). Tephras that cannot be well distinguished here (e.g. CCT, CGT) require other element plots, including trace elements. (**b**) After applying factor analysis to reduce 42 elements and element ratios to 9 principal components which account for 95% of variance in the samples, the dendrogram is produced by hierarchical cluster analysis (squared Euclidean distance, farthest neighbour method) using SPSS statistical software. The cluster analysis successfully reproduces known stratigraphic relations for the examples from El Salvador and Guatemala (cf. Kutterolf *et al.* 2008*a*).

ratios plotted needs to be evaluated in each case. The combinations which best distinguish different compositions will vary with the degree of differentiation (e.g. basaltic v. rhyolitic) of the tephras investigated, and with the general nature of the magmatic compositions and geotectonic setting (e.g. calc-alkaline v. highly alkalic or peralkaline compositions).

Numerical geochemical correlation

In order to compare all analysed elements simultaneously (possibly weighted by analytical precision relative to observed abundance or by petrologic significance), statistical techniques can be used. Sarna-Wojcicki *et al.* (1979) were among the first to apply a statistical correlation procedure to a large number of elements, determining a correlation coefficient together with its uncertainty that can be evaluated in a dendrogram. Similar, improved correlation methods have since been used in tephrostratigraphy to complement the graphical correlation (see Lowe *et al.* 2017 for a review of statistical techniques). Numerical correlation techniques use similarity coefficients (SC) and coefficients of variation (CV) to compare the whole geochemical datasets. The results can be clustered into dendrograms according to geochemical similarity to assist correlations (e.g. Kuehn and Foit 2006; Brendryen *et al.* 2010). Jordan *et al.* (2006) and Kutterolf *et al.* (2008*a*) used cluster analysis where a distance matrix from overall differences in the compositions of samples has been established to help correlate tephra deposits (Fig. 15b). The canonical Discriminant Function Analysis (DFA) is another statistical technique related to Principal Component Analysis (PCA) that reduces the dimensionality of data (such as compositional analyses) with a large number of independent variables (Lowe 2011) resulting in one or two canonical variables containing the whole compositional information (e.g. Molinaroli *et al.* 1991). Techniques such as cluster analysis can also be used to correlate other than geochemical features such as particle morphological parameters (Cioni *et al.* 2008).

Tephrochronology

Tephrochronology is a very important tool in determining the ages and rates of other geological processes such as changing climate proxies (e.g. Abbott *et al.* 2011). However, this wide field lies beyond the scope of this paper where we just want to emphasize that available age data do, of course, play an essential role in the tephra correlation between cores and with deposits on land. Marine tephra layers can be dated in four different ways.

(1) As noted above, the age of a well-dated tephra on land can be 'imported' if a marine ash bed can be sufficiently well correlated with that tephra.

(2) If that is not the case, the marine tephra may be directly radiometrically dated by, e.g. ^{14}C dating of C-bearing material within or directly below or above the bed (limited to <50 kyr), $^{40}Ar/^{39}Ar$ dating of K-bearing single crystals, or $^{238}U/^{230}Th$ dating of zircon crystals where present (e.g. Cisneros de Leon *et al.* 2021). Using thermoluminiscence of late Pleistocene to recent glass particles may also be an option (e.g. Berger 1991).

(3) Results from (1) and (2) can be used to estimated ages of undated (or undatable) marine tephra bed by linear interpolation provided the intercalated marine sediments do not show signs of highly variable sedimentation rates or erosion.

(4) An age model for a marine sediment core can be established by ^{18}O and ^{14}C profiles using microfossils (see the section 'Core correlation by sediment properties') as well as by measuring magnetic reversals. Such age models are typically determined for IODP/ODP cores (e.g. Brunner *et al.* 1998; Schindlbeck *et al.* 2018) but also for gravity cores (e.g. Vlag *et al.* 2004; Eisele *et al.* 2015*b*), and they constrain the ages of intercalated tephra beds.

All these dating methods have analytical errors. Therefore, integrating all available age data is essential to determine the best age (Blockley *et al.* 2008). Also, when many ash beds have been emplaced on the seafloor within a relatively short period of time, age dating alone may not provide unambiguous correlations and needs to be interpreted in the context of the other correlation parameters we have introduced above.

Core correlation by sediment properties

Ash layers in cores can also be correlated indirectly by correlating the cored sediments. A common approach is to measure foraminifer $\delta^{18}O$ isotopic variations at narrow spacings. The resulting profiles can be used to correlate cores but particularly to develop an age model of the core (Fig. 16c). Similarly, X-ray fluorescence (XRF) profile analysis produces compositional patterns that can be used for correlation but also help to identify ash layers or ash concentrations in sediment. Changes in sediment characteristics typically go along with colour changes which can be spectrometrically analysed and used for correlation provided that lightening conditions are kept constant. Figure 16a and b

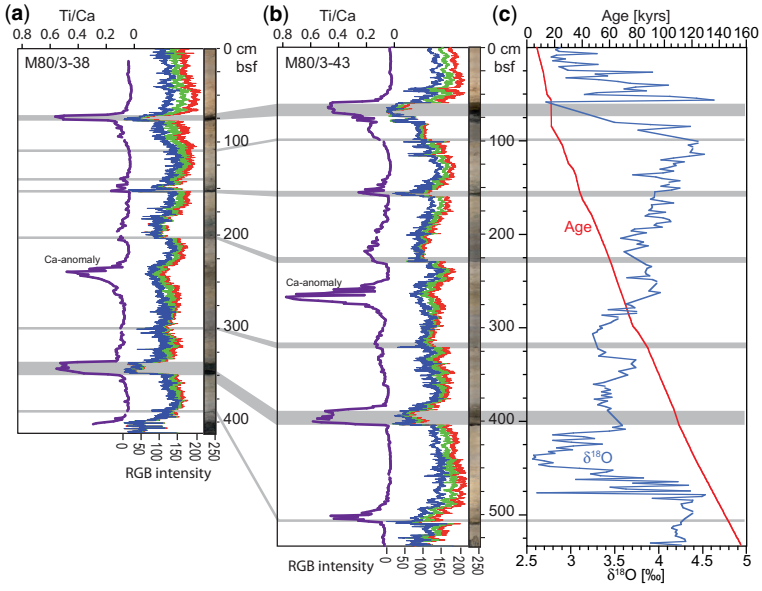

Fig. 16. Core logs of XRF analytical data (Ti/Ca ratio, violet curve) and colour spectral analysis R(ed)G(reen)B(lue) intensities of (**a**) core 38 and (**b**) core 43 from RV *Meteor* cruise M80/3, Cape Verde archipelago. Ash layers (connected by grey bars) have lower RGB intensities but higher Ti/Ca (but note Ca-anomaly at carbonate-rich horizon) and can thus be correlated between cores. (**c**) Benthic foraminifer $\delta^{18}O$ profile (blue) of core 43 that has been used to determine the age–depth relationship (red) by scaling to known $\delta^{18}O$-age variations. This allows to date ash layers and to identify age intervals in correlated cores. After Eisele *et al.* (2015*b*, fig. 7), with permission from Elsevier © 2015.

illustrates the combined use of XRF and RGB profiles in core correlation. Cassidy *et al.* (2014) also employed colour spectrography of a core for correlation and used lightness and hue values. In addition, core logging profiles (Fig. 2) can also be used for core correlations.

Conclusions

We have reviewed the appearance of marine volcaniclastic beds, which depends on the mode of emplacement by fallout or density current, the nature of subaerial or submarine eruption or of the submarine resedimentation processes, the distance and direction from primary or secondary source, the extent of modification on the seafloor by erosion and bioturbation, and finally, deformation during coring and core processing. The conditions of post-emplacement modifications on the seafloor constrain regions where ash layers have the best chance to survive until deeper burial. These preservation conditions place preliminary constraints on the selection of useful drill sites, apart from the optimal drilling strategy for the specific goals to be achieved. While seismic pre-site surveys reveal the best locations for ocean-drilling sites, gravity-core locations are best chosen by combining high-resolution bathymetry with hydroacoustic sub-bottom profiling of the target region.

In our review of the emplacement of pyroclastic fallout from terrestrial eruptions on the seafloor we have applied experimentally calibrated conditions for sediment plume formation to the natural condition of medium to fine ash deposited on the ocean. Such plumes are likely to replace individual grain settling for medium ash grain sizes at the range of observed distal fallout sedimentation rates. Sinking plumes can admix seawater (and planktonic biota) and convert into turbidity currents on the seafloor which are, however, too weak for tractional bedload transport or seafloor erosion. Hence, fallout ash beds aggregate by suspension sedimentation forming normal size grading above a sharp planar base, and are not readily distinguished from ash beds generated by individual particle settling.

Much more powerful volcaniclastic turbidity currents are generated where either pyroclastic flows from land enter the sea or where landslides from volcanic flank collapses mix with seawater. The homogeneity of juvenile volcanic components is an important criterion to distinguish these sources. Resulting turbidites typically rest on eroded surfaces and have Bouma facies divisions including thick massive facies that can be found even a few hundred kilometres from source. Turbidity currents also are the common product of submarine explosive eruptions. Very powerful eruptions in shallow water can generate eruption columns breaching the sea surface and emplacing fallout of highly vesicular particles similar to subaerial eruptions. Eruption columns reaching (close to) the sea surface, but also subaerial eruptions close to shore and pyroclastic flows entering the sea, can generate huge pumice rafts drifting for years, while pumice abrasion delivers ash to the seafloor. Ash and pumice mixed with water form proximal pumice breccias and distal ash turbidites mostly with low-energy characteristics containing both dense angular and vesicular shards. We show examples that even smaller-scale basaltic and felsic dome-forming eruptions can generate turbidity currents emplacing widespread volcaniclastic beds containing angular poorly vesicular or dense shards.

Turbidites formed by shelf erosion or break-up, potentially involving fluvial input, can be identified by high contents of shallow-water bioclasts and (possibly partly terrigenous) organic matter. At high latitudes, particularly during glacial times, ice rafts can emplace ash at great distance from source that is clearly outsized compared to primary distal fallout. The distinction between primary and secondary volcaniclastic deposits is essential for successful tephrostratigraphy and we discussed the relevant parameters bed structure and texture, lithologic composition, and juvenile particle's morphology and glass geochemical compositions. We also discussed the methods for tephra correlation which is a prerequisite to broaden the view from 1D single core information to 3D information from a core network and associated volcanic deposits on land, which deliver detailed information on eruption processes.

Acknowledgements We gratefully appreciate the constructive reviews by Raffaello Cioni and Mauro Rosi.

Author contributions **AF**: conceptualization (lead), formal analysis (lead), investigation (supporting), visualization (equal), writing – original draft (equal), writing – review & editing (lead); **JCS-B**: investigation (equal), visualization (equal), writing – original draft (equal), writing – review & editing (supporting); **SK**: investigation (equal), visualization (equal), writing – original draft (equal), writing – review & editing (supporting); **JLH**: visualization (equal), writing – original draft (equal), writing – review & editing (supporting).

Funding JLH acknowledges the NZ Marsden Fund Te Pūta Rangahau a Marsden for supporting her Marsden Fast Start project, 'Cryptotephra: unearthing hidden eruptions from Taupo Volcanic Zone' (MFP-VUW1809). JCB acknowledges the Bundesministerium für Bildung und Forschung for supporting her within the PalMod II-Cc. 2, TP5 Project (01LP1926E): Climate variability and its relationship to volcanism.

Data availability Data sharing is not applicable to this review article as no datasets were generated or analysed during the current study.

References

Abbott, P.M., Davies, S.M., Austin, W.E.N., Pearce, N.J.G. and Hibbert, F.D. 2011. Identification of cryptotephra horizons in a North East Atlantic marine record spanning Marine Isotope Stages 4 and 5a (*c.* 60 000–*c.* 82 000 a b2k). *Quaternary International*, **246**, 177–189, https://doi.org/10.1016/j.quaint.2011.07.033

Allan, A.S.R., Baker, J.A., Carter, L. and Wysoczanksi, R.J. 2008. Reconstructing the Quaternary evolution of the world's most active silicic volcanic system: insights from an *c.* 1.65 Ma deep ocean tephra record sourced from Taupo Volcanic Zone, New Zealand. *Quaternary Science Reviews*, **27**, 2341–2360, https://doi.org/10.1016/j.quascirev.2008.09.003

Allen, J.R.L. 1982. *Sedimentary Structures: Their Character and Physical Basis*. Developments in Sedimentology, **30A**.

Allen, S.R. and Freundt, A. 2006. Resedimentation of cold pumiceous ignimbrite into water: Facies transformations simulated in flume experiments. *Sedimentology*, **53**, 717–734, https://doi.org/10.1111/j.1365-3091.2006.00790.x

Allen, S.R. and McPhie, J. 2000. Water-settling and resedimentation of submarine rhyolitic pumice at Yali, eastern Aegean, Greece. *Journal of Volcanology and Geothermal Research*, **95**, 285–307, https://doi.org/10.1016/S0377-0273(99)00127-4

Allen, S.R. and McPhie, J. 2009. Products of Neptunian eruptions. *Geology*, **37**, 639–642, https://doi.org/10.1130/G30007A.1

Allen, S.R. and Stewart, A.L. 2003. Products of explosive subaqueous felsic eruptions based on examples from the Hellenic Island Arc, Greece. *AGU Geophysical Monograph Series*, **140**, 285–298.

Allen, S.R., Fiske, R.S. and Cashman, K.V. 2008. Quenching of steam-charged pumice: implications for submarine pyroclastic volcanism. *Earth and Planetary Science Letters*, **274**, 40–49, https://doi.org/10.1016/j.epsl.2008.06.050

Allen, S.R., Freundt, A. and Kurokawa, K. 2012. Characteristics of submarine pumice-rich density current deposits sourced from turbulent mixing of subaerial pyroclastic flows at the shoreline: field and experimental assessment. *Bulletin of Volcanology*, **74**, 657–675, https://doi.org/10.1007/s00445-011-0553-1

Alloway, B.V., Larsen, G., Lowe, D.J., Shane, P.A.R. and Westgate, J.A. 2007. Tephrochronology. *In*: Elias, S.A. (ed.) *Encyclopaedia of Quaternary Science*. Elsevier, London, 2869–2898.

Arnott, R.W.C. and Hand, B.M. 1989. Bedforms, primary structures and grain fabric in the presence of suspended sediment rain. *Journal of sedimentary Petrology*, **59**, 1062–1069.

Bagnold, R.A. 1962. Auto-suspension of transported sediment; turbidity currents. *Proceedings of the Royal Society, London*, **265**, 315–319.

Baines, P.G. and Sparks, R.S.J. 2005. Dynamics of giant volcanic ash clouds from supervolcanic eruptions. *Geophysical Research Letters*, **32**, L24808, https://doi.org/10.1029/2005GL024597

Barrett, R., Lebas, E. *et al*. 2020. Revisiting the tsunamigenic volcanic flank-collapse of Fogo Island in the Cape Verdes, offshore West Africa. *Geological Society, London, Special Publications*, **500**, https://doi.org/10.1144/SP500-2019-187

Berben, S.M.P., Dokken, T.M., Abbott, P.M., Cook, E., Sadatzki, H., Simon, M.H. and Jansen, E. 2020. Independent tephrochronological evidence for rapid and synchronous oceanic and atmospheric temperature rises over the Greenland stadial–interstadial transitions between *c.* 32 and 40 ka b2k. *Quaternary Science Reviews*, **236**, 106277, https://doi.org/10.1016/j.quascirev.2020.106277

Berger, G.W. 1991. The use of glass for dating volcanic ash by thermoluminescence. *Journal of Geophysical Research*, **96**, 19705–19720, https://doi.org/10.1029/91JB01899

Bertrand, S., Daga, R., Bedert, R. and Fontijn, K. 2014. Deposition of the 2011–2012 Cordón Caulle tephra (Chile, 40°S) in lake sediments: implications for tephrochronology and volcanology. *Journal of Geophysical Research: Earth Surface*, **119**, 2555–2573, https://doi.org/10.1002/2014JF003321

Blockley, S.P.E., Bronk Ramsey, C. and Pyle, D.M. 2008. Improved age modelling and high-precision age estimates of late Quaternary tephras, for accurate palaeoclimate reconstruction. *Journal of Volcanology and Geothermal Research*, **177**, 251–262, https://doi.org/10.1016/j.jvolgeores.2007.10.015

Blong, R. 1994. The Rabaul eruption, 1994. *The Australian Geographer*, **25**, 186–190, https://doi.org/10.1080/00049189408703118

Bogaard, P.V.D. and Schmincke, H.U. 1985. Laacher See tephra – A widespread isochronous late Quaternary tephra layer in central and Northern Europe. *Geological Society of America Bulletin*, **96**, 1554–1571, https://doi.org/10.1130/0016-7606(1985)96<1554:LSTAWI>2.0.CO;2

Bonadonna, C., Genco, R. *et al*. 2011. Tephra sedimentation during the 2010 Eyjafjallajökull eruption (Iceland) from deposit, radar, and satellite observations. *Journal of Geophysical Research*, **116**, B12202, https://doi.org/10.1029/2011JB008462

Bonatti, E. 1965. Palagonite, hyaloclastites and alteration of volcanic glass in the ocean. *Bulletin of Volcanology*, **28**, 257–269, https://doi.org/10.1007/BF02596930

Boulesteix, T., Hildenbrand, A., Gillot, P.Y. and Soler, V. 2012. Eruptive response of oceanic islands to giant landslides: new insights from the geomorphologic evolution of the Teide–Pico Viejo Volcanic Complex (Tenerife, Canary). *Geomorphology*, **138**, 61–73, https://doi.org/10.1016/j.geomorph.2011.08.025

Bradley, W.H. 1965. Vertical density currents. *Science (New York, NY)*, **150**, 1423–1428, https://doi.org/10.1126/science.150.3702.1423

Brazier, S., Sparks, R.S.J., Carey, S.N., Sigurdsson, H. and Westgate, J.A. 1983. Bimodal grain size distribution and secondary thickening in air-fall ash layers. *Nature*, **301**, 115–119, https://doi.org/10.1038/301115a0

Brendryen, J., Haflidason, H. and Sejrup, H.P. 2010. Norwegian Sea tephrostratigraphy of Marine Isotope Stages 4 and 5: prospects and problems for tephrochronology in the North Atlantic region. *Quaternary Science Reviews*, **29**, 847–864, https://doi.org/10.1016/j.quascirev.2009.12.004

Brunner, C., Sblendorio-Levy, J. *et al*. 1998. Biostratigraphic and magnetostratigraphic evaluation of sites 953, 954, 955 and 956, Canary Islands. *Proceedings of the Ocean Drilling Program, Scientific Results*, **157**, 97–114.

Bryan, S.E., Cook, A.G. *et al*. 2004. Pumice rafting and faunal dispersion during 2001–2002 in the Southwest Pacific: record of a dacitic submarine explosive eruption from Tonga. *Earth and Planetary Science Letters*, **227**, 135–154, https://doi.org/10.1016/j.epsl.2004.08.009

Bryan, S.E., Cook, A.G. *et al*. 2012. Rapid, long-distance dispersal by pumice rafting. *PLoS ONE*, **7**, e40583, https://doi.org/10.1371/journal.pone.0040583

Busschers, F.S., Kasse, C. *et al*. 2007. Late Pleistocene evolution of the Rhine-Meuse System in the southern North Sea Basin: imprints of climate change, sea-level oscillation and glacio-isostacy. *Quaternary Science Reviews*, **26**, 3216–3248, https://doi.org/10.1016/j.quascirev.2007.07.013

Çağatay, M.N., Wulf, S. *et al*. 2015. The tephra record from the Sea of Marmara for the last *c.* 70 ka and its palaeoceanographic implications. *Marine Geology*, **361**, 96–110, https://doi.org/10.1016/j.margeo.2015.01.005

Callow, R.H. and McIlroy, D. 2011. Ichnofabrics and ichnofabric-forming trace fossils in Phanerozoic turbidites. *Bulletin of Canadian Petroleum Geology*, **59**, 103–111, https://doi.org/10.2113/gscpgbull.59.2.103

Cantelli, A., Johnson, S., White, J.D.L. and Parker, G. 2008. Sediment sorting in the deposits of turbidity currents created by experimental modeling of explosive subaqueous eruptions. *Journal of Geology*, **116**, 76–93, https://doi.org/10.1086/524676

Cantner, K., Carey, S. and Nomikou, P. 2014. Integrated volcanologic and petrologic analysis of the 1650 AD eruption of Kolumbo Submarine Volcano, Greece. *Journal of Volcanology and Geothermal Research*, **269**, 28–43, https://doi.org/10.1016/j.jvolgeores.2013.10.004

Carazzo, G. and Jellinek, A.M. 2012. A new view of the dynamics, stability and longevity of volcanic clouds. *Earth and Planetary Science Letters*, **325–326**, 39–51, https://doi.org/10.1016/j.epsl.2012.01.025

Carey, S. 1997. Influence of convective sedimentation on the formation of widespread tephra fall layers in the deep sea. *Geology*, **25**, 839–842, https://doi.org/10.1130/0091-7613(1997)025<0839:IOCSOT>2.3.CO;2

Carey, S.N. and Sigurdsson, H. 1978. Deep-sea evidence for distribution of tephra from the mixed magma eruption of the Soufrière on St. Vincent, 1902: ash turbidites and air fall. *Geology*, **6**, 271–274, https://doi.org/10.1130/0091-7613(1978)6<271:DEFDOT>2.0.CO;2

Carey, S.N. and Sigurdsson, H. 1982. Influence of particle aggregation on deposition of distal tephra from the May 18, 1980, eruption of Mount St. Helens volcano. *Journal of Geophysical Research*, **87**, 7061–7072, https://doi.org/10.1029/JB087iB08p07061

Carey, S., Sigurdsson, H., Mandeville, C. and Bronto, S. 1996. Pyroclastic flows and surges over water: An example from the 1883 Krakatau eruption. *Bulletin of Volcanology*, **57**, 493–511, https://doi.org/10.1007/BF00304435

Carey, S., Sigurdsson, H., Mandeville, C. and Bronto, S. 2000. Volcanic hazards from pyroclastic flow discharge into the sea: examples from the 1883 eruption of Krakatau, Indonesia. *Geological Society of America Special Paper*, **345**, 1–14.

Carey, R.J., Soule, S.A. *et al*. 2018. The largest deep-ocean silicic volcanic eruption of the past century. *Science Advances*, **4**, e1701121, https://doi.org/10.1126/sciadv.1701121

Carter, L., Nelson, C.S., Neil, H.L. and Froggatt, P.C. 1995. Correlation, dispersal, and preservation of the Kawakawa tephra and other late Quaternary tephra layers in the Southwest Pacific Ocean. *New Zealand Journal of Geology and Geophysics*, **38**, 29–46, https://doi.org/10.1080/00288306.1995.9514637

Cas, R.A.F. and Simmons, J.M. 2018. Why deep-water eruptions are so different from subaerial eruptions. *Frontiers in Earth Science*, **6**, 198, https://doi.org/10.3389/feart.2018.00198

Casalbore, D., Clare, M.A. *et al*. 2021. Bedforms on the submarine flanks of insular volcanoes: new insights gained from high resolution seafloor surveys. *Sedimentology*, **68**, 1400–1438, https://doi.org/10.1111/sed.12725

Cashman, K.V. 1992. Groundmass crystallization of Mount St. Helens dacite, 1980–1986 – a tool for interpreting shallow magmatic processes. *Contributions to Mineralogy and Petrology*, **109**, 431–449, https://doi.org/10.1007/BF00306547

Cashman, K.V. and Fiske, R.S. 1991. Fallout of pyroclastic debris from submarine volcanic eruptions. *Science (New York, NY)*, **253**, 275–280, https://doi.org/10.1126/science.253.5017.275

Cassidy, M., Watt, S.F.L., Palmer, M.R., Trofimovs, J., Symons, W., Maclachlan, S.E. and Stinton, A.J. 2014. Construction of volcanic records from marine sediment cores: a review and case study (Montserrat, West Indies). *Earth-Science Reviews*, **138**, 137–155, https://doi.org/10.1016/j.earscirev.2014.08.008

Chang, Y.C., Mitchell, N.C., Hansteen, T.H., Schindlbeck-Belo, J.C. and Freundt, A. 2021. Volcaniclastic deposits and sedimentation processes around volcanic ocean islands: the central Azores. *Geological Society, London, Special Publications*, **520**, https://doi.org/10.1144/SP520-2021-62

Chikita, K. 1990. Sedimentation by river-induced turbidity currents: field measurements and interpretation. *Sedimentology*, **37**, 891–905, https://doi.org/10.1111/j.1365-3091.1990.tb01832.x

Cioni, R., D'Oriano, C. and Bertagnini, A. 2008. Fingerprinting ash deposits of small scale eruptions by their physical and textural features. *Journal of Volcanology and Geothermal Research*, **177**, 277–287, https://doi.org/10.1016/j.jvolgeores.2008.06.003

Cisneros de Leon, A., Schindlbeck-Belo, J.C. *et al*. 2021. A history of violence: magma incubation, timing and tephra distribution of the Los Chocoyos supereruption (Atitlán Caldera, Guatemala). *Journal of Quaternary Science*, **36**, 169–179, https://doi.org/10.1002/jqs.3265

Cita, M.B. and Aloisi, G. 2000. Deep-sea tsunami deposits triggered by the explosion of Santorini (3500 y BP), eastern Mediterranean. *Sedimentary Geology*, **135**, 181–203, https://doi.org/10.1016/S0037-0738(00)00071-3

Cita, M.B. and Podenzani, M. 1980. Destructive effects of oxygen starvation and ash falls on benthic life: a pilot study. *Quaternary Research*, **13**, 230–241, https://doi.org/10.1016/0033-5894(80)90031-9

Clift, P.D. and Blusztajn, J. 1999. The trace-element characteristics of Aegean and Aeolian volcanic arc marine tephra. *Journal of Volcanology and Geothermal Research*, **92**, 321–347, https://doi.org/10.1016/S0377-0273(99)00059-1

Cole, P.D., Guest, J.E., Duncan, A.M. and Pacheco, J.M. 2001. Capelinhos 1957–1958, Faial, Azores: deposits formed by an emergent surtseyan eruption. *Bulletin of Volcanology*, **63**, 204–220, https://doi.org/10.1007/s004450100136

Critelli, S. and Ingersoll, R.V. 1995. Interpretation of neovolcanic v. palaeovolcanic sand grains: an example from Miocene deep-marine sandstone of the Topanga Group (Southern California). *Sedimentology*, **42**, 783–804, https://doi.org/10.1111/j.1365-3091.1995.tb00409.x

Cunningham, J.K. and Beard, A.D. 2014. An unusual occurrence of mafic accretionary lapilli in deep-marine volcaniclastics on 'Eua, Tonga: palaeoenvironment and process. *Journal of Volcanology and Geothermal Research*, **274**, 139–151, https://doi.org/10.1016/j.jvolgeores.2014.01.012

Davies, S.M. 2015. Cryptotephras: the revolution in correlation and precision dating. *Journal of Quaternary Science*, **30**, 114–130, https://doi.org/10.1002/jqs.2766

Davies, S.M., Abbott, P.M. *et al*. 2014. A North Atlantic tephrostratigraphical framework for 130–60 ka b2k: new tephra discoveries, marine-based correlations, and future challenges. *Quaternary Science Reviews*, **106**, 101–121, https://doi.org/10.1016/j.quascirev.2014.03.024

De Vantier, L.M. 1992. Rafting of tropical marine organisms on buoyant coralla. *Marine Ecology Progress Series*, **86**, 301–302, https://doi.org/10.3354/meps086301

Deplus, C., Le Friant, A. *et al*. 2001. Submarine evidence for large-scale debris avalanches in the Lesser Antilles Arc. *Earth and Planetary Science Letters*, **192**, 145–157, https://doi.org/10.1016/S0012-821X(01)00444-7

Derkachev, A.N., Gorbarenko, S.A., Ponomareva, V.V., Portnyagin, M.V., Malakhova, G.I. and Liu, Y. 2020. Middle to late Pleistocene record of explosive volcanic eruptions in marine sediments offshore Kamchatka (Meiji Rise, NW Pacific). *Journal of Quaternary Science*, **35**, 362–379, https://doi.org/10.1002/jqs.3175

Di Roberto, A., Rosi, M., Bertagnini, A., Marani, M.P. and Gamberi, F. 2010. Distal turbidites and tsunamigenic landslides of Stromboli Volcano (Aeolian Islands, Italy). *In*: Mosher, D.C., Shipp, R.C. *et al*. (eds) *Submarine Mass Movements and Their Consequences. Advances in Natural and Technological Hazards Research*. Springer, Dordrecht, **28**, 719–731, https://doi.org/10.1007/978-90-481-3071-9_58

Dioguardi, F., Mele, D. and Dellino, P. 2018. A new one-equation model of fluid drag for irregularly shaped particles valid over a wide range of Reynolds Number. *Geophysical Research Letters*, **123**, 144–156, https://doi.org/10.1002/2017JB014926

Dufek, J. and Bergantz, G.W. 2007. The suspended-load and bed-load transport of particle laden gravity currents: Insight from pyroclastic flows that traverse water. *Theoretical and Computational Fluid Dynamics*, **21**, 119–145, https://doi.org/10.1007/s00162-007-0041-6

Dufek, J. and Manga, M. 2008. The in-situ production of ash in pyroclastic flows. *Journal of Geophysical Research*, **113**, B09207, https://doi.org/10.1029/2007JB005555

Duggen, S., Croot, P., Schacht, U. and Hoffmann, L. 2007. Subduction zone volcanic ash can fertilize the surface ocean and stimulate phytoplankton growth: evidence from biogeochemical experiments and satellite data. *Geophysical Research Letters*, **34**, L01621, https://doi.org/10.1029/2006GL027522

Dunbar, N.W., Iverson, N.A. *et al*. 2017. New Zealand supereruption provides time marker for the Last Glacial Maximum in Antarctica. *Scientific Reports*, **7**, 12238, https://doi.org/10.1038/s41598-017-11758-0

Durant, A.J., Villarosa, G., Rose, W.I., Delmelle, P., Prata, A.J. and Viramonte, J.G. 2012. Long-range volcanic ash transport and fallout during the 2008 eruption of Chaitén Volcano, Chile. *Physics and Chemistry of the Earth*, **45–46**, 50–64, https://doi.org/10.1016/j.pce.2011.09.004

Dürig, T., White, J.D.L. *et al*. 2020*a*. Deep-sea eruptions boosted by induced fuel-coolant explosions. *Nature Geoscience*, **13**, 498–503, https://doi.org/10.1038/s41561-020-0603-4

Dürig, T., White, J.D.L., Zimanowski, B., Büttner, R., Murch, A. and Carey, R.J. 2020*b*. Deep-sea fragmentation style of havre revealed by dendrogrammatic analyses of particle morphometry. *Bulletin of Volcanology*, **82**, 67, https://doi.org/10.1007/s00445-020-01408-1

Eisele, S., Freundt, A., Kutterolf, S., Ramalho, R.S., Kwasnitschka, T., Wang, K.L. and Hemming, S.R. 2015*a*. Stratigraphy of the Pleistocene, phonolitic Cão Grande Formation on Santo Antão, Cape Verde. *Journal of Volcanology and Geothermal Research*, **301**, 204–220, https://doi.org/10.1016/j.jvolgeores.2015.03.012

Eisele, S., Reißig, S., Freundt, A., Kutterolf, S., Nürnberg, D., Kwasnitschka, T. and Wang, K-L. 2015*b*. Pleistocene to Holocene offshore tephrostratigraphy of highly explosive eruptions from the southwestern Cape Verde archipelago. *Marine Geology*, **369**, 233–250, https://doi.org/10.1016/j.margeo.2013.06.017

Eisma, D. and Passchier, C.A. 1978. Rates of sedimentation on the Cape Verde rise. *Netherlands Journal of Sea Research*, **12**, 107–114, https://doi.org/10.1016/0077-7579(78)90028-5

Engwell, S., Sparks, R.S.J. and Carey, S. 2014. Physical characteristics of tephra layers in the deep sea realm: the Campanian ignimbrite eruption. *Geological Society, London, Special Publications*, **398**, 2–19, https://doi.org/10.1144/SP398.7

Eychenne, J. and Le Pennec, J.L. 2012. Sigmoidal particle density distribution in a subplinian scoria fall deposit. *Bulletin of Volcanology*, **74**, 2243–2249, https://doi.org/10.1007/s00445-012-0671-4

Fauria, K.E., Manga, M. and Wei, Z. 2017. Trapped bubbles keep pumice afloat and gas diffusion makes pumice sink. *Earth and Planetary Science Letters*, **460**, 50–59, https://doi.org/10.1016/j.epsl.2016.11.055

Federman, A.N. and Scheidegger, K.F. 1984. Compositional heterogeneity of distal tephra deposits from the 1912 eruption of Novarupta, Alaska. *Journal of Volcanology and Geothermal Research*, **21**, 233–254, https://doi.org/10.1016/0377-0273(84)90024-6

Fierstein, J. and Hildreth, W. 1992. The plinian eruptions of 1912 at Novarupta, Katmai National Park, Alaska. *Bulletin of Volcanology*, **54**, 646–684, https://doi.org/10.1007/BF00430778

Fisk, M. and McLoughlin, N. 2013. Atlas of alteration textures in volcanic glass from the ocean basins. *Geosphere*, **9**, 317–341, https://doi.org/10.1130/GES00827.1

Fiske, R.S., Cashman, K.V., Shibata, A. and Watanabe, K. 1998. Tephra dispersal from Myojinsho, Japan, during its shallow submarine eruption of 1952–1953. *Bulletin of Volcanology*, **59**, 262–275, https://doi.org/10.1007/s004450050190

Fiske, R.S., Naka, J., Iizasa, K., Yuasa, M. and Klaus, A. 2001. Submarine silicic caldera at the front of the Izu-Bonin Arc, Japan: voluminous seafloor eruptions of rhyolite pumice. *Geological Society of America Bulletin*, **113**, 813–824, https://doi.org/10.1130/0016-7606(2001)113<0813:SSCATF>2.0.CO;2

Freundt, A. 2003. Entrance of hot pyroclastic flows into the sea: experimental observations. *Bulletin of Volcanology*, **65**, 144–164, https://doi.org/10.1007/s00445-002-0250-1

Freundt, A. and Schmincke, H.U. 1998. Emplacement of ash layers related to high-grade ignimbrite P1 in the sea around Gran Canaria. *Proceedings of the Ocean Drilling Program, Scientific Results*, **157**, 201–218.

Froese, D.G., Lowe, D.J., Knott, J.R. and Slate, J.L. 2008. Global tephra studies: John Westgate and Andrei Sarna-Wojcicki commemorative volume. *Quaternary International*, **178**, 1–3, https://doi.org/10.1016/j.quaint.2007.12.005

Fuller, S., Carey, S. and Nomikou, P. 2018. Distribution of fine-grained tephra from the 1650 AD submarine eruption of Kolumbo Volcano, Greece. *Journal of Volcanology and Geothermal Research*, **352**, 10–25, https://doi.org/10.1016/j.jvolgeores.2018.01.004

Garcia, M.O. and Hull, D.M. 1994. Turbidites from giant Hawaiian landslides: results from Ocean Drilling Program Site 842. *Geology*, **22**, 159–162, https://doi.org/10.1130/0091-7613(1994)022<0159:TFGHLR>2.3.CO;2

Gatti, E. and Oppenheimer, C. 2012. Utilization of distal tephra records for understanding climatic and environmental consequences of the youngest Toba Tuff. *Geophysical Monograph Series*, **198**, 63–73, https://doi.org/10.1029/2012GM001216

Gatti, E., Villa, I.M., Achyuthan, H., Gibbard, P.L. and Oppenheimer, C. 2014. Geochemical variability in distal and proximal glass from the youngest Toba Tuff eruption. *Bulletin of Volcanology*, **76**, 859, https://doi.org/10.1007/s00445-014-0859-x

Gieskes, J.M. and Lawrence, J.R. 1981. Alteration of volcanic matter in deep sea sediments: evidence from the chemical composition of interstitial waters from deep sea drilling cores. *Geochimica et Cosmochimica Acta*, **45**, 1687–1703, https://doi.org/10.1016/0016-7037(81)90004-1

Gilbert, J.S. and Lane, S.J. 1994. The origin of accretionary lapilli. *Bulletin of Volcanology*, **56**, 398–411, https://doi.org/10.1007/BF00326465

Gilbert, D., Freundt, A., Kutterolf, S. and Burkert, C. 2012. Post-glacial time series of explosive eruptions and associated changes in the magma plumbing system of Lonquimay Volcano, south-central Chile. *International Journal of Earth Sciences*, **103**, 2043–2062, https://doi.org/10.1007/s00531-012-0796-x

Griggs, A.J., Davies, S.M., Abbott, P.M., Coleman, M., Palmer, A.P., Rasmussen, T.L. and Johnston, R. 2015. Visualizing tephra deposits and sedimentary processes in the marine environment: the potential of X-ray microtomography. *Geochemistry, Geophysics, Geosystems*, **16**, 4329–4343, https://doi.org/10.1002/2015GC006073

Griggs, A.J., Davies, S.M., Abbott, P.M. and Rasmussen, T.L. 2014. Optimising the use of marine tephrochronology in the North Atlantic: a detailed investigation of the Faroe marine ash zones II, III and IV. *Quaternary Science Reviews*, **106**, 122–139, https://doi.org/10.1016/j.quascirev.2014.04.031

Gudmundsdóttir, E.R., Eiríksson, J. and Larsen, G. 2011. Identification and definition of primary and reworked tephra in Late Glacial and Holocene marine shelf sediments off north Iceland. *Journal of Quaternary Science*, **26**, 589–602, https://doi.org/10.1002/jqs.1474

Haeckel, M., van Beusekom, J., Wiesner, M.G. and König, I. 2001. The impact of the 1991 Mount Pinatubo tephra fallout on the geochemical environment of the deep-sea sediments in the South China Sea. *Earth and Planetary Science Letters*, **193**, 151–166, https://doi.org/10.1016/S0012-821X(01)00496-4

Harders, R., Kutterolf, S., Hensen, C., Moerz, T. and Brueckmann, W. 2010. Tephra layers: a controlling factor on submarine translational sliding? *Geochemistry, Geophysics, Geosystems*, **11**, Q05S23, https://doi.org/10.1029/2009GC002844

Head, J.W. III and Wilson, L. 2003. Deep submarine pyroclastic eruptions: theory and predicted landforms and deposits. *Journal of Volcanology and Geothermal Research*, **121**, 155–193, https://doi.org/10.1016/S0377-0273(02)00425-0

Herd, R.A., Edmonds, M. and Bass, V. 2005. Catastrophic lava dome failure at Soufriere Hills Volcano, Montserrat 12–13 July 2003. *Journal of Volcanology and Geothermal Research*, **148**, 234–252, https://doi.org/10.1016/j.jvolgeores.2005.05.003

Hess, S. and Kuhnt, W. 1996. Deep-sea benthic foraminiferal recolonization of the 1991 Mt. Pinatubo ash layer in the South China Sea. *Marine Micropaleontology*, **28**, 171–197, https://doi.org/10.1016/0377-8398(95)00080-1

Hess, S., Kuhnt, W., Hill, S., Kaminski, M.A., Holbourn, A. and de Leon, M. 2001. Monitoring the recolonization of the Mt. Pinatubo 1991 ash layer by benthic foraminifera. *Marine Micropaleontology*, **43**, 119–142, https://doi.org/10.1016/S0377-8398(01)00025-1

Holasek, R.E., Self, S. and Woods, A.W. 1996. Satellite observations and interpretation of the 1991 Mount Pinatubo eruption plumes. *Journal of Geophysical*

Research, **101**, 27635–27655, https://doi.org/10.1029/96JB01179

Hong, W.-L., Torres, M.E. and Kutterolf, S. 2020. Towards a global quantification of volcanogenic aluminosilicate alteration rates through the mass balance of strontium in marine sediments. *Chemical Geology*, **550**, 119743, https://doi.org/10.1016/j.chemgeo.2020.119743

Hopkins, J.L., Wilson, C.J.N. *et al*. 2017. Multi-criteria correlation of tephra deposits to source centres applied in the Auckland Volcanic Field, New Zealand. *Bulletin of Volcanology*, **79**, 55, https://doi.org/10.1007/s00445-017-1131-y

Hopkins, J.L., Wysoczanski, R.J. *et al*. 2020. Deposition and preservation of tephra in marine sediments at the active Hikurangi subduction margin. *Quaternary Science Reviews*, **247**, 106500, https://doi.org/10.1016/j.quascirev.2020.106500

Hoyal, D.C.J.D., Bursik, M.I. and Atkinson, J.F. 1999. Settling-driven convection: a mechanism of sedimentation from stratified fluids. *Journal of Geophysical Research*, **104**, 7953–7966, https://doi.org/10.1029/1998JC900065

Huang, T.C., Watkins, N.D. and Shaw, D.M. 1975. Atmospherically transported volcanic glass in deep-sea sediments: volcanism in sub-Antarctic latitudes of the South Pacific during late Pliocene and Pleistocene time. *Geological Society of America Bulletin*, **86**, 1305–1315, https://doi.org/10.1130/0016-7606(1975)86<1305:ATVGID>2.0.CO;2

Hunt, C., Moskowitz, B.M. and Banerjee, S.K. 1995. Magnetic properties of rocks and minerals. *Rock Physics and Phase Relations AFU Ref Shelf*, **3**, 189–204.

Hunt, J.B. and Najman, Y.M.R. 2003. Tephrochronological and tephrostratigraphical potential of Pliocene–Pleistocene volcaniclastic deposits in the Japan forearc, ODP Leg 186. *Proceedings of the Ocean Drilling Program, Scientific Results*, **186**, https://doi.org/10.2973/odp.proc.sr.186.107.2003

Hunt, J.E., Wynn, R.B., Masson, D.G., Talling, P.J. and Teagle, D.A.H. 2011. Sedimentological and geochemical evidence for multistage failure of volcanic island landslides: a case study from Icod Landslide on North Tenerife. *Geochemistry Geophysics Geosystems*, **12**, Q12007, https://doi.org/10.1029/2011GC003740

Hunt, J.E., Wynn, R.B., Talling, P.J. and Masson, D.G. 2013. Turbidite record of frequency and source of large volume (>100 km^3) Canary Island landslides in the last 1.5 Ma: implications for landslide triggers and geohazards. *Geochemistry, Geophysics, Geosystems*, **14**, 2100–2123, https://doi.org/10.1002/ggge.20139

Hunt, J.E., Talling, P.J., Clare, M.A., Jarvis, I. and Wynn, R.B. 2014. Long-term (17 Ma) turbidite record of the timing and frequency of large flank collapses of the Canary Islands. *Geochemistry, Geophysics, Geosystems*, **15**, 3322–3345, https://doi.org/10.1002/2014GC005232

Ikegami, F., McPhie, J., Carey, R., Mundana, R., Soule, A. and Jutzeler, M. 2018. The eruption of submarine rhyolite lavas and domes in the deep ocean – Havre 2012, Kermadec Arc. *Frontiers in Earth Science*, **6**, 147, https://doi.org/10.3389/feart.2018.00147

Iriyama, Y., Toramaru, A. and Yamamoto, T. 2018. Theory for deducing volcanic activity from size distributions in plinian pyroclastic fall deposit. *Journal of Geophysical Research*, **123**, 2199–2213, https://doi.org/10.1002/2017JB014782

Jacobs, C.T., Goldin, T.J. *et al*. 2015. An improved quantitative measure of the tendency for volcanic ash plumes to form in water: implications for the deposition of marine ash beds. *Journal of Volcanology and Geothermal Research*, **290**, 114–124, https://doi.org/10.1016/j.jvolgeores.2014.10.015

James, M.R., Gilbert, J.S. and Lane, S.J. 2002. Experimental investigation of volcanic particle aggregation in the absence of a liquid phase. *Journal of Geophysical Research*, **107**, https://doi.org/10.1029/2001JB000950

Jordan, B.R., Sigurdsson, H., Carey, S.N., Rogers, R. and Ehrenborg, J. 2006. Geochemical correlation of Caribbean Sea tephra layers with ignimbrites in Central America. *Geological Society of America Special Paper*, **402**, 175–208.

Jutzeler, M., Marsh, R., Carey, R.J., White, J.D.L., Talling, P.J. and Karlstrom, L. 2014*a*. On the fate of pumice rafts formed during the 2012 Havre submarine eruption. *Nature Communications*, **5**, 3660, https://doi.org/10.1038/ncomms4660

Jutzeler, M., White, J.D.L., Talling, P.J., McCanta, M., Morgan, S., Le Friant, A. and Ishizuka, O. 2014*b*. Coring disturbances in IODP piston cores with implications for offshore record of volcanic events and the Missoula megafloods. *Geochemistry, Geophysics, Geosystems*, **15**, 3572–3590, https://doi.org/10.1002/2014GC005447

Jutzeler, M., McPhie, J. and Allen, S.R. 2015. Explosive destruction of a Pliocene hot lava dome underwater: Dogashima (Japan). *Journal of Volcanology and Geothermal Research*, **304**, 75–81, https://doi.org/10.1016/j.jvolgeores.2015.08.009

Jutzeler, M., Manga, M. *et al*. 2017. Submarine deposits from pumiceous pyroclastic density currents traveling over water: an outstanding example from offshore Montserrat (IODP 340). *Geological Society of America Bulletin*, **129**, 392–414, https://doi.org/10.1130/B31448.1

Kandlbauer, J., Carey, S. and Sparks, R.S.J. 2013. The 1815 Tambora ash fall: implications for the transport and deposition of distal ash on land and in the deep sea. *Bulletin of Volcanology*, **75**, 708, https://doi.org/10.1007/s00445-013-0708-3

Karstens, J., Berndt, C. *et al*. 2019. From gradual spreading to catastrophic collapse: reconstruction of the 1888 Ritter island volcanic sector collapse from high resolution 3D seismic data. *Earth and Planetary Science Letters*, **517**, 1–13, https://doi.org/10.1016/j.epsl.2019.04.009

Kennett, J. 1981. Marine tephrochronology. *In*: Emiliani, C. (ed.) *The Oceanic Lithosphere*. Wiley, New York, 1373–1436.

Kent, A.J.R., Peate, D.W., Newman, S., Stolper, E.M. and Pearce, J.A. 2002. Chlorine in submarine glasses from the Lau basin: seawater contamination and constraints on the composition of slab-derived fluids. *Earth and Planetary Science Letters*, **202**, 361–377, https://doi.org/10.1016/S0012-821X(02)00786-0

Kerle, N., van Wyk de Vries, B. and Oppenheimer, C. 2003. New insight into factors leading to the 1998 flank collapse and lahar disaster at Casita Volcano, Nicaragua. *Bulletin of Volcanology*, **65**, 331–345, https://doi.org/10.1007/s00445-002-0263-9

Kjær, K.H., Sultan, L., Krüger, J. and Schomacker, A. 2004. Architecture and sedimentation of outwash fans in front of the Mýrdalsjökull ice cap, Iceland. *Sedimentary Geology*, **172**, 139–163, https://doi.org/10.1016/j.sedgeo.2004.08.002

Kneller, B.C. and Branney, M.J. 1995. Sustained high-density turbidity currents and the deposition of thick massive sands. *Sedimentology*, **42**, 607–616, https://doi.org/10.1111/j.1365-3091.1995.tb00395.x

Koffman, B.G., Kreutz, K.J., Kurbatov, A.V. and Dunbar, N.W. 2013. Impact of known local and tropical volcanic eruptions of the past millennium on the WAIS divide microparticle record. *Geophysical Research Letters*, **40**, 4712–4716, https://doi.org/10.1002/grl.50822

Kohn, B.P. and Glasby, G.P. 1978. Tephra distribution and sedimentation rates in the Bay of Plenty, New Zealand. *New Zealand Journal of Geology and Geophysics*, **21**, 49–70, https://doi.org/10.1080/00288306.1978.10420721

Kokelaar, P. 1986. Magma–water interactions in subaqueous and emergent basaltic volcanism. *Bulletin of Volcanology*, **48**, 275–290, https://doi.org/10.1007/BF01081756

Kokelaar, P. and Busby, C. 1992. Subaqueous explosive eruption and welding of pyroclastic deposits. *Science (New York, NY)*, **257**, 196–201, https://doi.org/10.1126/science.257.5067.196

Kokelaar, P. and Romagnoli, C. 1995. Sector collapse, sedimentation and clast population evolution at an active island-arc volcano: Stromboli, Italy. *Bulletin of Volcanology*, **57**, 240–262, https://doi.org/10.1007/BF00265424

Koller, D.K., de Oliveira Borges, A.L., Puhl, E. and Manica, R. 2017. Prediction of the bedforms generated by density currents based on fluvial phase diagrams. *Brazilian Journal of Water Resources (RBRH)*, **22**, e49, https://doi.org/10.1590/2318-0331.0217160021

Komar, P.D. 1985. The hydraulic interpretation of turbidites from their grain sizes and sedimentary structures. *Sedimentology*, **32**, 395–407, https://doi.org/10.1111/j.1365-3091.1985.tb00519.x

Komar, P.D. and Clemens, K.E. 1986. The relationship between a grain's settling velocity and the threshold of motion under unidirectional currents. *Journal of Sedimentary Petrology*, **56**, 258–266.

Krastel, S., Schmincke, H.-U., Jacobs, C.L., Rihm, R., Le Bas, T.P. and Alibes, B. 2001. Submarine landslides around the Canary Islands. *Journal of Geophysical Research*, **106**, 3977–3998, https://doi.org/10.1029/2000JB900413

Krastel, S., Andrade, M. *et al.* 2019. The tsunamigenic gravitational flank-collapse of Fogo volcano, Cape Verde Islands, Seismic pre-site survey for an IODP site on the Cape Verde Plateau, Cruise No. M155, 26.05.19–30.06.19, Pointe-à-Pitre (Guadeloupe) – Mindelo (Cape Verde). *METEOR-Berichte, Gutachterpanel Forschungsschiffe, Bonn*, **M155**, 1–44, https://doi.org/10.1029/2000JB900413

Kubo, Y. and Nakajima, T. 2002. Laboratory experiments and numerical simulation of sediment-wave formation by turbidity currents. *Marine Geology*, **192**, 105–121, https://doi.org/10.1016/S0025-3227(02)00551-0

Kuehn, S.C. and Foit, F.F. Jr 2006. Correlation of widespread Holocene and Pleistocene tephra layers from Newberry Volcano, Oregon, USA, using glass compositions and numerical analysis. *Quaternary International*, **148**, 113–137, https://doi.org/10.1016/j.quaint.2005.11.008

Kunii, D. and Levenspiel, O. 1969, 1977. *Fluidization Engineering*. Wiley, New York.

Kutterolf, S., Schacht, U., Wehrmann, H., Freundt, A. and Mörz, T. 2007. Onshore to offshore tephrostratigraphy and marine ash layer diagnesis in Central America. *In*: Buntschuh, J. and Alvarado, G.E. (eds) *Central America – Geology, Resources and Hazards*. Taylor and Francis/Balkema, 395–423.

Kutterolf, S., Freundt, A., Peréz, W., Mörz, T., Schacht, U., Wehrmann, H. and Schmincke, H.U. 2008*a*. Pacific offshore record of plinian arc volcanism in Central America: 1. along-arc correlations. *Geochemistry, Geophysics, Geosystems*, **9**, Q02S01, https://doi.org/10.1029/2007GC001631

Kutterolf, S., Freundt, A. and Peréz, W. 2008*b*. The Pacific offshore record of plinian arc volcanism in Central America, part 2: tephra volumes and erupted masses. *Geochemistry, Geophysics, Geosystems*, **9**, Q02S02, https://doi.org/10.1029/2007GC001791

Kutterolf, S., Freundt, A., Schacht, U., Bürk, D., Harders, R., Mörz, T. and Peréz, W. 2008*c*. The Pacific offshore record of plinian arc volcanism in Central America, part 3: application to forearc geology. *Geochemistry, Geophysics, Geosystems*, **9**, Q02S03, https://doi.org/10.1029/2007GC001826

Kutterolf, S., Liebetrau, V., Mörz, T., Freundt, A., Hammerich, T. and Garbe-Schönberg, D. 2008*d*. Lifetime and cyclicity of fluid venting at forearc mound structures determined by tephrostratigraphy and radiometric dating of authigenic carbonates. *Geology*, **36**, 707–710, https://doi.org/10.1130/G24806A.1

Kutterolf, S., Jegen, M., Mitrovica, J.X., Kwasnitschka, T., Freundt, A. and Huybers, P. 2013. A detection of Milankovitch frequencies in global volcanic activity. *Geology*, **41**, 227–230, https://doi.org/10.1130/G33419.1

Kutterolf, S., Schindlbeck, J.C. *et al.* 2014. Large volume submarine ignimbrites in the Shikoku Basin: an example for explosive volcanism in the Western Pacific during the Late Miocene. *Geochemistry, Geophysics, Geosystems*, **15**, 1837–1851, https://doi.org/10.1002/2014GC005263

Kutterolf, S., Hansteen, T.H., Freundt, A., Wehrmann, H., Appel, K., Krüger, K. and Perez, W. 2015. Bromine and chlorine emissions from plinian eruptions along the Central American volcanic Arc: from source to atmosphere. *Earth and Planetary Science Letters*, **429**, 234–246, https://doi.org/10.1016/j.epsl.2015.07.064

Kutterolf, S., Schindlbeck, J.C. *et al.* 2016. A 400-ka tephrochronological framework for Central America from Lake Petén Itzá (Guatemala) sediments. *Quaternary Science Reviews*, **150**, 200–220, https://doi.org/10.1016/j.quascirev.2016.08.023

Kutterolf, S., Schindlbeck, J.C., Robertson, A.H.F., Avery, A., Baxter, A.T., Petronotis, K. and Wang, K.-L. 2018. Tephrostratigraphy and provenance from IODP expedition 352, Izu-Bonin Arc: tracing tephra sources and volumes from the Oligocene to the Recent. *Geochemistry,*

Geophysics, Geosystems, **19**, 150-174, https://doi.org/10.1002/2017GC007100

Kutterolf, S., Schindlbeck, J.C., Jegen, M., Freundt, A. and Straub, S.M. 2019. Milankovitch frequencies in tephra records at volcanic arcs: the relation of kyr-scale cyclic variations in volcanism to global climate changes. *Quaternary Science Reviews*, **204**, 1–16, https://doi.org/10.1016/j.quascirev.2018.11.004

Labazuy, P. 1996. Recurrent landslides events on the submarine flank of Piton de la Fournaise Volcano (Reunion Island). *Geological Society, London, Special Publications*, **110**, 295–306, https://doi.org/10.1144/GSL.SP.1996.110.01.23

Lacasse, C., Sigurdsson, H., Carey, S., Paterne, M. and Guichard, F. 1996. North Atlantic deep-sea sedimentation of late Quaternary tephra from the Iceland hotspot. *Marine Geology*, **129**, 207–235, https://doi.org/10.1016/0025-3227(96)83346-9

Lacasse, C., Werner, R., Paterne, M., Sigurdsson, H., Carey, S. and Pinte, G. 1998. Long-range transport of Icelandic tephra to the Irminger Basin, site 919. *Proceedings of the Ocean Drilling Program, Scientific Results*, **152**, 51–65.

Lackschewitz, K.S. and Wallrabe-Adams, H.J. 1997. Composition and origin of volcanic ash zones in late Quaternary sediments from the Reykjanes Ridge: evidence for ash fallout and ice-rafting. *Marine Geology*, **136**, 209–224, https://doi.org/10.1016/S0025-3227(96)00056-4

Langmann, B., Zaksek, K., Hort, M. and Duggen, S. 2010. Volcanic ash as fertiliser for the surface ocean. *Atmospheric Chemistry and Physics*, **10**, 3891–3899, https://doi.org/10.5194/acp-10-3891-2010

Ledbetter, M.T. and Sparks, R.S.J. 1979. Duration of large-magnitude explosive eruptions deduced from graded bedding in deep-sea ash layers. *Geology*, **7**, 240–244, https://doi.org/10.1130/0091-7613(1979)7<240:DOLEED>2.0.CO;2

Lim, C., Lee, I. and Ikehara, K. 2013. Geochemical identification of cryptotephras using INAA from late Quaternary hemipelagic sediments, southwest Japan. *Marine Geology*, **346**, 233–245, https://doi.org/10.1016/j.margeo.2013.09.013

Lowe, D.R. 1988. Suspended-load fallout rate as an independent variable in the analysis of current structures. *Sedimentology*, **35**, 765–776, https://doi.org/10.1111/j.1365-3091.1988.tb01250.x

Lowe, D.J. 2011. Tephrochronology and its application: a review. *Quaternary Geochronology*, **6**, 107–153, https://doi.org/10.1016/j.quageo.2010.08.003

Lowe, J.J., Bronk Ramsey, C., Housley, R.A., Lane, C.S., and Tomlinson, E.L. and RESET team and Associates 2015. The RESET project: constructing a European tephra lattice for refined synchronisation of environmental and archaeological events during the last *c.* 100 ka. *Quaternary Science Reviews*, **118**, 1–17, https://doi.org/10.1016/j.quascirev.2015.04.006

Lowe, D.J., Pearce, N.J., Jorgensen, M.A., Kuehn, S.C., Tryon, C.A. and Hayward, C.L. 2017. Correlating tephras and cryptotephras using glass compositional analyses and numerical and statistical methods: review and evaluation. *Quaternary Science Reviews*, **175**, 1–44, https://doi.org/10.1016/j.quascirev.2017.08.003

Lu, Y., Waldmann, N., Alsop, G.I. and Marco, S. 2017. Interpreting soft sediment deformation and mass transport deposits as seismites in the Dead Sea depocenter. *Journal of Geophysical Research*, **122**, 8305–8325, https://doi.org/10.1002/2017JB014342

Luo, M., Torres, M. *et al*. 2020. Impact of iron release by volcanic ash alteration on carbon cycling in sediments of the Northern Hikurangi Margin. *Earth and Planetary Science Letters*, **541**, 116288, https://doi.org/10.1016/j.epsl.2020.116288

Lüthi, S. 1981. Experiments on non-channelized turbidity currents and their deposits. *Marine Geology*, **40**, M59–M68, https://doi.org/10.1016/0025-3227(81)90139-0

Mahony, S.H., Sparks, R.S.J. *et al*. 2016. Increased rates of large-magnitude explosive eruptions in Japan in the late Neogene and Quaternary. *Geochemistry, Geophysics, Geosystems*, **17**, 2467–2479, https://doi.org/10.1002/2016GC006362

Mahony, S.H., Barnard, N.H., Sparks, R.S.J. and Rougier, J.C. 2020. VOLCORE, a global database of visible tephra layers sampled by ocean drilling. *Nature Scientific Data*, **7**, 330, https://doi.org/10.1038/s41597-020-00673-1

Mandeville, C.W., Carey, S., Sigurdsson, H. and King, J. 1994. Paleomagnetic evidence for high-temperature emplacement of the 1883 subaqueous pyroclastic flows from Krakatau Volcano, Indonesia. *Journal of Geophysical Research*, **99**, 9487–9504, https://doi.org/10.1029/94JB00239

Mandeville, C.W., Carey, S. and Sigurdsson, H. 1996. Sedimentology of the Krakatau 1883 submarine pyroclastic deposits. *Bulletin of Volcanology*, **57**, 512–529, https://doi.org/10.1007/BF00304436

Mann, C.P., Stix, J., Vallance, J.W. and Richer, M. 2004. Subaqueous intracaldera volcanism, Ilopango Caldera, El Salvador, Central America. *Geological Society of America Special Paper*, **375**, 159–174, https://doi.org/10.1130/SPE375

Manville, V. 2001. Sedimentology and history of Lake Reporoa: an ephemeral supra-ignimbrite lake, Taupo Volcanic Zone, New Zealand. *Special Publications of the International Association of Sedimentologists*, **30**, 109–140, https://doi.org/10.1002/9781444304251.ch6

Manville, V. and Wilson, C.J.N. 2004. Vertical density currents: a review of their potential role in the deposition and interpretation of deep-sea ash layers. *Journal of the Geological Society, London*, **161**, 947–958, https://doi.org/10.1144/0016-764903-067

Manville, V., White, J.D.L., Houghton, B.F. and Wilson, C.J.N. 1998. The saturation behaviour of pumice and some sedimentological implications. *Sedimentary Geology*, **119**, 5–16, https://doi.org/10.1016/S0037-0738(98)00057-8

Manzella, I., Bonadonna, C., Phillips, J.C. and Monnard, H. 2015. The role of gravitational instabilities in deposition of volcanic ash. *Geology*, **43**, 211–214, https://doi.org/10.1130/G36252.1

Marquez, E.J. 2000. The 1991 Mount Pinatubo eruption and eastern South China Sea foraminifera: occurrence, composition and recovery. *Island Arc*, **9**, 527–541, https://doi.org/10.1111/j.1440-1738.2000.00299.x

Marquez, E.J., Militante-Matias, P.J. *et al.* 1999. Deep-sea foraminiferal distribution of the central and eastern portions of the South China Sea. *GEOSEA 98 Proceedings, Geological Society of Malaysia Bulletin*, **43**, 529–536, https://doi.org/10.7186/bgsm4319 9953

Masson, D.G., Watts, A.B., Gee, M.J.R., Urgeles, R., Mitchell, N.C., Le Bas, T.P. and Canals, M. 2002. Slope failures on the flanks of the Western Canary Islands. *Earth-Science Reviews*, **57**, 1–35, https://doi.org/10.1016/S0012-8252(01)00069-1

Masson, D.G., Le Bas, T.P., Grevemeyer, I. and Weinrebe, W. 2008. Flank collapse and large-scale landsliding in the Cape Verde islands, off West Africa. *Geochemistry, Geophysics, Geosystems*, **9**, Q07015, https://doi.org/10.1029/2008GC001983

Mastin, L.G., Guffanti, M. *et al*. 2009. A multidisciplinary effort to assign realistic source parameters to models of volcanic ash-cloud transport and dispersion during eruptions. *Journal of Volcanology and Geothermal Research*, **186**, 10–21, https://doi.org/10.1016/j.jvolgeores.2009.01.008

Matsu'ura, T., Ueno, T. and Furusawa, A. 2011. Characterization and correlation of cryptotephras using major-element analyses of melt inclusions preserved in quartz in last interglacial marine sediments, southeastern Shikoku, Japan. *Quaternary International*, **246**, 48–56, https://doi.org/10.1016/j.quaint.2011.03.017

McGuire, W.J. 2006. Global risk from extreme geophysical events: threat identification and assessment. *Philosophical Transactions of the Royal Society*, **A364**, 1889–1909, https://doi.org/10.1098/rsta.2006.1804

Metzner, D., Kutterolf, S., Toohey, M., Timmreck, C., Niemeier, U., Freundt, A. and Krüger, K. 2012. Radiative forcing and climate impact resulting from SO_2 injections based on a 200 000-year record of plinian eruptions along the Central American volcanic arc. *International Journal of Earth Sciences*, **103**, 2063–2079, https://doi.org/10.1007/s00531-012-0814-z

Molinaroli, E., Blom, M. and Basu, A. 1991. Methods of provenance determination tested with discriminant function analysis. *Journal of Sedimentary Research*, **61**, 900–908.

Moore, J.G. and Normark, W.R. 1994. Giant Hawaiian landslides. *Annual Review of Earth and Planetary Sciences*, **22**, 119–144, https://doi.org/10.1146/annurev.ea.22.050194.001003

Moore, J.G. and Peck, D.L. 1962. Accretionary lapilli in volcanic rocks of the western continental United States. *Journal of Geology*, **70**, 182–193, https://doi.org/10.1086/626807

Moore, J.G., Clague, D.A., Holcomb, R.T., Lipman, P.W., Normark, W.R. and Torresan, M.E. 1989. Prodigious submarine land-slides on the Hawaiian ridge. *Journal of Geophysical Research*, **94**, 17465–17485, https://doi.org/10.1029/JB094iB12p17465

Mottl, M. 1989. Hydrothermal convection, reaction and diffusion in sediments on the Costa Rica rift flank: porewater evidence from ODP site 677 and 678. *Proceedings of the Ocean Drilling Program, Scientific Results*, **111**, 195–209.

Mueller, W.U. 2003. A subaqueous eruption model for shallow-water, small-volume eruptions: Evidence from two Precambrian examples. *AGU Geophysical Monograph Series*, **140**, 189–203.

Murch, A.P., White, J.D.L. and Carey, R.J. 2019*a*. Characteristics and deposit stratigraphy of submarine-erupted silicic ash, Havre Volcano, Kermadec Arc, New Zealand. *Frontiers in Earth Science*, **7**, 1, https://doi.org/10.3389/feart.2019.00001

Murch, A.P., White, J.D.L. and Carey, R.J. 2019*b*. Unusual fluidal behavior of a silicic magma during fragmentation in a deep subaqueous eruption, Havre Volcano, southwestern Pacific Ocean. *Geology*, **47**, 487–490, https://doi.org/10.1130/G45657.1

Murch, A.P., White, J.D.L., Barreyre, T., Carey, R.J., Mundana, R. and Ikegami, F. 2020. Volcaniclastic dispersal during submarine lava effusion: the 2012 eruption of Havre Volcano, Kermadec Arc, New Zealand. *Frontiers in Earth Science*, **8**, 237, https://doi.org/10.3389/feart.2020.00237

Ninkovich, D. and Shackleton, N.J. 1975. Distribution, stratigraphic position and age of ash layer 'L' in the Panama Basin region. *Earth and Planetary Science Letters*, **27**, 20–34, https://doi.org/10.1016/0012-821X(75)90156-9

Ninkovich, D., Sparks, R.S.J. and Ledbetter, M.T. 1978. The exceptional magnitude and intensity of the Toba eruption, Sumatra: an example of the use of deep-sea tephra layers as a geological tool. *Bulletin of Volcanology*, **41**, 286–298, https://doi.org/10.1007/BF02597228

Nishimura, A., Rodolfo, K.S., Koizumi, A., Gill, J. and Fujioka, K. 1992. Episodic deposition of Pliocene–Pleistocene pumice from the Izu-Bonin Arc, Leg 126. *Proceedings of the Ocean Drilling Program, Scientific Results*, **126**, 3–21.

Okuno, M., Torii, M. *et al*. 2011. Widespread tephras in sediments from Lake Ichi-No-Megata in northern Japan: Their description, correlation and significance. *Quaternary International*, **246**, 270–277, https://doi.org/10.1016/j.quaint.2011.08.015

Paladio-Melosantos, M.L.O., Solidum, R.U. *et al*. 1996. Tephra falls of the 1991 eruptions of Mount Pinatubo. *In*: Newhall, C.G. and Punongbayan, R.S. (eds) *Fire and Mud: Eruptions and Lahars of Mount Pinatubo, Philippines*. Philippine Institute of Volcanology and Seismology, Quezon City, and University of Washington Press, Seattle, 513–536.

Pallister, J.S., Trusdell, F.A., Brownfield, I.K., Siems, D.F., Budahn, J.R. and Sutley, S.F. 2005. The 2003 phreatomagmatic eruptions of Anatahan Volcano – textural and petrologic features of deposits at an emergent island volcano. *Journal of Volcanology and Geothermal Research*, **146**, 208–225, https://doi.org/10.1016/j.jvolgeores.2004.11.036

Papp, K.R., Dean, K.G. and Dehn, J. 2005. Predicting regions susceptible to high concentrations of airborne volcanic ash in the North Pacific region. *Journal of Volcanology and Geothermal Research*, **148**, 295–314, https://doi.org/10.1016/j.jvolgeores.2005.04.020

Paris, R., Geichetti, T., Chevalier, J., Guillou, H. and Frank, N. 2011. Tsunami deposits in Santiago island (Cape Verde archipelago) as possible evidence of a massive flank failure of Fogos Volcano. *Sedimentary Geology*, **239**, 129–145, https://doi.org/10.1016/j.sedgeo.2011.06.006

Paris, R., Ramalho, R.S. *et al*. 2018. Mega-tsunami conglomerates and flank collapses of ocean island

volcanoes. *Marine Geology*, **395**, 168–187, https://doi.org/10.1016/j.margeo.2017.10.004

Park, C. and Schmincke, H.U. 2020. Multistage damming of the Rhine river by tephra fallout during the 12,900 BP plinian Laacher See eruption (Germany). Syn-eruptive rhine damming I. *Journal of Volcanology and Geothermal Research*, **389**, 106688, https://doi.org/10.1016/j.jvolgeores.2019.106688

Parker, G. 1982. Conditions for the ignition of catastrophically erosive turbidity currents. *Marine Geology*, **46**, 307–327, https://doi.org/10.1016/0025-3227(82)90086-X

Paterne, M., Labeyrie, J., Guichard, F., Mazaud, A. and Maitre, F. 1990. Fluctuations of the Campanian explosive volcanic activity (south Italy) during the past 190 000 years, as determined by marine tephrochronology. *Earth and Planetary Science Letters*, **98**, 166–174, https://doi.org/10.1016/0012-821X(90)90057-5

Pearce, J.A. and Norry, M.J. 1979. Petrogenetic implications of Ti, Zr, Y and Nb variations in volcanic rocks. *Contributions to Mineralogy and Petrology*, **69**, 33–47, https://doi.org/10.1007/BF00375192

Pearce, N.J.G., Westgate, J.A., Perkins, W.T., Eastwood, W.J. and Shane, P. 1999. The application of laser ablation ICP-MS to the analysis of volcanic glass shards from tephra deposits: bulk glass and single shard analysis. *Global and Planetary Change*, **21**, 151–171, https://doi.org/10.1016/S0921-8181(99)00012-0

Pearce, N.J.G., Eastwood, W.J., Westgate, J.A. and Perkins, W.T. 2002. Trace-element composition of single glass shards in distal Minoan tephra from SW Turkey. *Journal of the Geological Society, London*, **159**, 545–556, https://doi.org/10.1144/0016-764 901-129

Pearce, N.J., Alloway, B.V. and Westgate, J.A. 2008. Mid-Pleistocene silicic tephra beds in the Auckland region, New Zealand: their correlation and origins based on the trace element analyses of single glass shards. *Quaternary International*, **178**, 16–43, https://doi.org/10.1016/j.quaint.2006.09.005

Pearce, N.J.G., Westgate, J.A., Gualda, G.A.R., Gatti, E. and Muhammad, R.F. 2020. Tephra glass chemistry provides storage and discharge details of five magma reservoirs which fed the 75 ka youngest Toba Tuff eruption, Northern Sumatra. *Journal of Quaternary Science*, **35**, 256–271, https://doi.org/10.1002/jqs.3149

Pillans, B., Alloway, B., Naish, T., Westgate, J., Abbott, S. and Palmer, A. 2005. Silicic tephras in Pleistocene shallow-marine sediments of Wanganui Basin, New Zealand. *Journal of the Royal Society of New Zealand*, **35**, 43–90, https://doi.org/10.1080/03014223.2005.9517777

Pistolesi, M., Isaia, R. *et al*. 2016. Simultaneous eruptions from multiple vents at Campi Flegrei (Italy) highlight new eruption processes at calderas. *Geology*, **44**, 487–490, https://doi.org/10.1130/G37870.1

Pistolesi, M., Bertagnini, A., Di Roberto, A., Ripepe, M. and Rosi, M. 2020. Tsunami and tephra deposits record interactions between past eruptive activity and landslides at Stromboli Volcano, Italy. *Geology*, **48**, 436–440, https://doi.org/10.1130/G47331.1

Ponomareva, V., Portnyagin, M. and Davies, S.M. 2015*a*. Tephra without borders: Far-reaching clues into past explosive eruptions. *Frontier in Earth Science*, **3**, 83, https://doi.org/10.3389/feart.2015.00083

Ponomareva, V., Portnyagin, M., Pevzner, M., Blaauw, M., Kyle, P. and Derkachev, A. 2015*b*. Tephra from andesitic Shiveluch Volcano, Kamchatka, NW Pacific: chronology of explosive eruptions and geochemical fingerprinting of volcanic glass. *International Journal of Earth Sciences*, **104**, 1459–1482, https://doi.org/10.1007/s00531-015-1156-4

Ramalho, R.S., Winckler, G. *et al*. 2015. Hazard potential of volcanic flank collapses raised by new megatsunami evidence. *Scientific Advances*, **1**, e1500456, https://doi.org/10.1126/sciadv.1500456

Rampino, M.R. and Ambrose, S.H. 2000. Volcanic winter in the Garden of Eden: The Toba supereruption and the late Pleistocene human population crash. *Geological Society of America Special Paper*, **345**, 71–82.

Reedman, A.J., Howells, M.F., Orton, G. and Campbell, S.D.G. 1987. The Pitts Head Tuff formation: a subaerial to submarine welded ash-flow tuff of Ordovician age, North Wales. *Geological Magazine*, **124**, 427–439, https://doi.org/10.1017/S0016756800017015

Risso, C., Scasso, R.A. and Aparicio, A. 2002. Presence of large pumice blocks on Tierra Del Fuego and South Shetland Islands shorelines, from 1962 South Sandwich Islands eruption. *Marine Geology*, **186**, 413–422, https://doi.org/10.1016/S0025-3227(02)00190-1

Rose, W.I. and Chesner, C.A. 1990. Worldwide dispersal of ash and gases from earth's largest known eruption: Toba, Sumatra, 75 ka. *Paleogeography Paleoclimatology Paleoecology (Global and Planetary Change)*, **89**, 269–275, https://doi.org/10.1016/0031-0182(90)90068-I

Rose, W.I. and Durant, A. 2009. Fine ash content of explosive eruptions. *Journal of Volcanology and Geothermal Research*, **186**, 32–39, https://doi.org/10.1016/j.jvolgeores.2009.01.010

Rosi, M., Vezzoli, L., Aleotti, P. and De Censi, M. 1996. Interaction between caldera collapse and eruptive dynamics during the Campanian ignimbrite eruption, Phlegraean Fields, Italy. *Bulletin of Volcanology*, **57**, 541–554, https://doi.org/10.1007/BF00304438

Rosi, M., Vezzoli, L., Castelmenzano, A. and Grieco, G. 1999. Plinian pumice fall deposit of the Campanian ignimbrite eruption (Phlegraean Fields, Italy). *Journal of Volcanology and Geothermal Research*, **91**, 179–198, https://doi.org/10.1016/S0377-0273(99)00035-9

Rosi, M., Paladio-Melosantos, M.L., Di Muro, A., Leoni, R. and Bacolcol, T. 2001. Fall vs flow activity during the 1991 climactic eruption of Pinatubo Volcano (Philippines). *Bulletin of Volcanology*, **62**, 549–566, https://doi.org/10.1007/s004450000118

Rosi, M., Levi, S.T. *et al*. 2019. Geoarchaeological evidence of middle-age tsunamis at Stromboli and consequences for the tsunami hazard in the Southern Tyrrhenian Sea. *Scientific Reports*, **9**, 677, https://doi.org/10.1038/s41598-018-37050-3

Rotella, M.D., Wilson, C.J.N., Barker, S.J., Schipper, C.I., Wright, I.C. and Wysoczanski, R.J. 2015. Dynamics of deep submarine silicic explosive eruptions in the Kermadec Arc, as reflected in pumice vesicularity textures. *Journal of Volcanology and Geothermal Research*, **301**, 314–332, https://doi.org/10.1016/j.jvolgeores.2015.05.021

Rutledal, S., Berben, S.M., Dokken, T.M., Van Der Bilt, W.G., Cederstrøm, J.M. and Jansen, E. 2020. Tephra

horizons identified in the Western North Atlantic and Nordic Seas during the last glacial period: extending the marine tephra framework. *Quaternary Science Reviews*, **240**, 106247, https://doi.org/10.1016/j.quascirev.2020.106247

Sammartini, M., Camerlenghi, A. *et al*. 2018. Open-slope, translational submarine landslide in a tectonically active volcanic continental margin (Licosa Submarine Landslide, Southern Tyrrhenian Sea). *Geological Society, London, Special Publications*, **477**, 133–150, https://doi.org/10.1144/SP477.34

Sarna-Wojcicki, A.M., Bowman, H.W. and Russell, P.C. 1979. Chemical correlation of some late Cenozoic tuffs of northern and central California by neutron activation analysis of glass and comparison with X-ray fluorescence analysis. *US Geological Survey Professional Paper*, **1147**, 1–45.

Sarna-Wojcicki, A.M., Pringle, M.S. and Wijbrans, J. 2000. New $^{40}Ar/^{39}Ar$ age of the Bishop Tuff from multiple sites and sediment rate calibration for the Matuyama-Brunhes boundary. *Journal of Geophysical Research: Solid Earth*, **105**, 21431–21443, https://doi.org/10.1029/2000JB900901

Saxby, J., Cashman, K., Rust, A. and Beckett, F. 2020. The importance of grain size and shape in controlling the dispersion of the Vedde cryptotephra. *Journal of Quaternary Science*, **35**, 175–185, https://doi.org/10.1002/jqs.3152

Schacht, U., Wallmann, K., Kutterolf, S. and Schmidt, M. 2008. Volcanogenic sediment–seawater interactions and the geochemistry of pore waters. *Chemical Geology*, **249**, 321–338, https://doi.org/10.1016/j.chemgeo.2008.01.026

Schacht, U., Wallmann, K. and Kutterolf, S. 2010. The influence of volcanic ash alteration on the REE composition of marine pore waters. *Journal of Geochemical Exploration*, **106**, 176–187, https://doi.org/10.1016/j.gexplo.2010.02.006

Scheffler, J. 2020. *First compositional characterization of the three youngest volcaniclastic layers in distal core M155/14, south of Fogo, Cape Verdes*. BSc thesis, Department of Geoscience, University of Kiel.

Schenk, J.A. 2020. *Die Verfolgung von Massentransportablagerungen von ihrer Quelle zu ihrer Ablagerung: Kompositionelle Charakterisierung der jüngsten vulkaniklastischen Lagen im proximalen Kern M155/38 südlich von Fogo, Kap Verden*. BSc thesis, Department of Geoscience, University of Kiel.

Schindlbeck, J.C., Kutterolf, S., Freundt, A., Scudder, R.P., Pickering, K.T. and Murray, R.W. 2013. Emplacement processes of submarine volcaniclastic deposits (IODP site C0011, Nankai Trough). *Marine Geology*, **343**, 115–124, https://doi.org/10.1016/j.margeo.2013.06.017

Schindlbeck, J.C., Kutterolf, S. *et al*. 2016*a*. Late Cenozoic tephrostratigraphy offshore the southern Central American volcanic arc: 1. tephra ages and provenance. *Geochemistry, Geophysics, Geosystems*, **17/11**, 4641–4668, https://doi.org/10.1002/2016GC006503

Schindlbeck, J.C., Kutterolf, S., Freundt, A., Straub, S.M., Vannucchi, P. and Alvarado, G.E. 2016*b*. Late Cenozoic tephrostratigraphy offshore the southern Central American volcanic arc: 2. implications for magma production rates and subduction erosion. *Geochemistry, Geophysics, Geosystems*, **17**, 4585–4604, https://doi.org/10.1002/2016GC006504

Schindlbeck, J.C., Kutterolf, S., Straub, S., Andrews, G.D.M., Wang, K.-L. and Mleneck-Vautravers, M.J. 2018. One million years tephra record at IODP sites U1436 and U1437: Insights into explosive volcanism from the Japan and Izu arcs. *Island Arc*, **27**, e12244, https://doi.org/10.1111/iar.12244

Schmincke, H.U. and Segschneider, B. 1998. Shallow submarine to emergent basaltic shield volcanism of Gran Canaria: evidence from drilling into the volcanic apron. *Proceedings of the Ocean Drilling Program, Scientific Results*. **157**, 141–179.

Schmincke, H.U. and Sumita, M. 1998. Tephra event stratigraphy and emplacement of tephra layers, Mogan and Fataga stratigraphic intervals. part II: origin and emplacement of volcaniclastic layers. *Proceedings of the Ocean Drilling Program, Scientific Results*. **157**, 267–291.

Schneider, J.L. and Fisher, R.V. 1996. Obispo Formation, California: remobilized pyroclastic material. *US Geological Survey Bulletin*, **1995**, O1–O21.

Schneider, J.L., Le Ruyet, A., Chanier, F., Buret, C., Ferriere, J., Proust, J.N. and Rosseel, J.B. 2001. Primary or secondary distal volcaniclastic turbidites: How to make the distinction? An example from the Miocene of New Zealand (Mahia Peninsula, North Island). *Sedimentary Geology*, **145**, 1–22, https://doi.org/10.1016/S0037-0738(01)00108-7

Schumacher, R. and Schmincke, H.U. 1995. Models for the origin of accretionary lapilli. *Bulletin of Volcanology*, **56**, 626–639, https://doi.org/10.1007/BF00301467

Scolamacchia, T. and Dingwell, D.B. 2014. Sulfur as a binding agent of aggregates in explosive eruptions. *Bulletin of Volcanology*, **76**, 871, https://doi.org/10.1007/s00445-014-0871-1

Scollo, S., Bonadonna, C. and Manzella, I. 2017. Settling-driven gravitational instabilities associated with volcanic clouds: new insights from experimental investigations. *Bulletin of Volcanology*, **79**, 39, https://doi.org/10.1007/s00445-017-1124-x

Seilacher, A. 1969. Fault-graded beds interpreted as seismites. *Sedimentology*, **13**, 155–159, https://doi.org/10.1111/j.1365-3091.1969.tb01125.x

Sell, B.K. and Samson, S.D. 2011. A tephrochronologic method based on apatite trace-element chemistry. *Quaternary Research*, **76**, 157–166, https://doi.org/10.1016/j.yqres.2011.03.007

Sevink, J., van Gorp, W., Di Vito, M.A. and Arienzo, I. 2020. Distal tephra from campanian eruptions in early Late Holocene fills of the Agro Pontino Graben and Fondi Basin (Southern Lazio, Italy). *Journal of Volcanology and Geothermal Research*, **405**, 107041, https://doi.org/10.1016/j.jvolgeores.2020.107041

Shane, P. 1998. Correlation of rhyolitic pyroclastic eruptive units from the Taupo Volcanic Zone by Fe–Ti oxide compositional data. *Bulletin of Volcanology*, **60**, 224–238, https://doi.org/10.1007/s004450050229

Shane, P. and Wright, I.C. 2011. Late Quaternary tephra layers around Raoul and Macauley Islands, Kermadec Arc: implications for volcanic sources, explosive volcanism and tephrochronology. *Journal of Quaternary Science*, **26**, 422–432, https://doi.org/10.1002/jqs.1468

Shane, P., Nairn, I.A., Martin, S.B. and Smith, V.C. 2008. Compositional heterogeneity in tephra deposits resulting from the eruption of multiple magma bodies: implications for tephrochronology. *Quaternary International*, **178**, 44–53, https://doi.org/10.1016/j.quaint.2006.11.014

Sigurdsson, H. and Carey, S. 1989. Plinian and co-ignimbrite tephra fall from the 1815 eruptions of Tambora Volcano. *Bulletin of Volcanology*, **51**, 243–270, https://doi.org/10.1007/BF01073515

Sigurdsson, H., Sparks, R.S.J., Carey, S.N. and Huang, T.C. 1980. Volcanogenic sedimentation in the Lesser Antilles Arc. *Journal of Geology*, **88**, 523–540, https://doi.org/10.1086/628542

Smith, R.B. 1991. Diagenesis and cementation of lower Miocene pyroclastic sequences in the Sulu Sea, sites 768, 769, and 771. *Proceedings of the Ocean Drilling Program, Scientific Results*, **124**, 181–199.

Solan, M., Wigham, B.D. *et al*. 2004. In situ quantification of bioturbation using time-lapse fluorescent sediment profile imaging (f-SPI), luminophore tracers and model simulation. *Marine Ecology Progress Series*, **271**, 1–12, https://doi.org/10.3354/meps271001

Sousa, J. and Voight, B. 1995. Multiple-pulsed debris avalanche emplacement at Mount St. Helens in 1980: evidence from numerical continuum flow simulations. *Journal of Volcanology and Geothermal Research*, **66**, 227–250.

Sparks, R.S.J. and Huang, T.C. 1980. The volcanological significance of deep-sea ash layers associated with ignimbrites. *Geological Magazine*, **117**, 425–436, https://doi.org/10.1017/S0016756800028533

Sparks, R.S.J. and Walker, G.P.L. 1977. The significance of vitric-enriched air-fall ashes associated with crystal-enriched ignimbrites. *Journal of Volcanology and Geothermal Research*, **2**, 329–341, https://doi.org/10.1016/0377-0273(77)90019-1

Sparks, R.S.J., Self, S. and Walker, G.P.L. 1973. Products of ignimbrite eruptions. *Geology*, **1**, 115–118, https://doi.org/10.1130/0091-7613(1973)1<115:POIE>2.0.CO;2

Sparks, R.S.J., Sigurdsson, H. and Carey, S.N. 1980. The entrance of pyroclastic flows into the sea. II: theoretical considerations on subaqueous emplacement and welding. *Journal of Volcanology and Geothermal Research*, **7**, 97–105, https://doi.org/10.1016/0377-0273(80)90022-0

Sparks, R.S.J., Brazier, S., Huang, T.C. and Muerdter, D. 1983. Sedimentology of the Minoan deep-sea tephra layer in the Aegean and eastern Mediterranean. *Marine Geology*, **54**, 131–167, https://doi.org/10.1016/0025-3227(83)90011-7

Sparks, R.S.J., Bursik, M.I., Ablay, G.J., Thomas, R.M.E. and Carey, S.N. 1992. Sedimentation of tephra by volcanic plumes. part 2: controls on thickness and grain-size variations of tephra fall deposits. *Bulletin of Volcanology*, **54**, 685–695, https://doi.org/10.1007/BF00430779

Sparks, R.S.J., Murphy, M.D., Lejeune, A.M., Watts, R.B., Barcley, J. and Young, S.R. 2000. Control on the emplacement of the andesite lava dome of the Soufriere Hills Volcano, Montserrat by degassing-induced crystallization. *Terra Nova*, **12**, 14–20, https://doi.org/10.1046/j.1365-3121.2000.00267.x

Staudigel, H. and Schmincke, H.-U. 1984. The Pliocene seamount series of La Palma/Canary Islands. *Journal of Geophysical Research*, **89**, 11195–11215, https://doi.org/10.1029/JB089iB13p11195

Stroncik, N.A. and Schmincke, H.U. 2002. Palagonite – a review. *International Journal of Earth Sciences*, **91**, 680–697, https://doi.org/10.1007/s00531-001-0238-7

Sun, C., Plunkett, G. *et al*. 2014. Ash from Changbaishan millennium eruption recorded in Greenland ice: Implications for determining the eruption's timing and impact. *Geophysical Research Letters*, **41**, 694–701, https://doi.org/10.1002/2013GL058642

Tamura, Y., Busby, C.J. and Blum, P. and the Expedition 350 Scientists 2015. *Proceedings of the International Ocean Discovery Program, Expedition 350: Izu-Bonin-Mariana Rear Arc*. College Station, Texas, https://doi.org/10.14379/iodp.proc.350.2015

Tani, K., Fiske, R.S., Tamura, Y., Kido, Y., Naka, J., Shukuno, H. and Takeuchi, R. 2008. Sumisu volcano, Izu-Bonin Arc, Japan: site of a silicic caldera-forming eruption from a small open-ocean island. *Bulletin of Volcanology*, **70**, 547–562, https://doi.org/10.1007/s00445-007-0153-2

Telling, J. and Dufek, J. 2012. An experimental evaluation of ash aggregation in explosive volcanic eruptions. *Journal of Volcanology and Geothermal Research*, **209–210**, 1–8, https://doi.org/10.1016/j.jvolgeores.2011.09.008

Thornalley, D.J., McCave, I.N. and Elderfield, H. 2011. Tephra in deglacial ocean sediments south of Iceland: stratigraphy, geochemistry and oceanic reservoir ages. *Journal of Quaternary Science*, **26**, 190–198, https://doi.org/10.1002/jqs.1442

Tibaldi, A. 2001. Multiple sector collapses at Stromboli Volcano, Italy: how they work. *Bulletin of Volcanology*, **63**, 112–125, https://doi.org/10.1007/s004450100129

Todd, J.A., Austin, W.E. and Abbott, P.M. 2014. Quantifying bioturbation of a simulated ash fall event. *Geological Society, London, Special Publications*, **398**, 195–207, https://doi.org/10.1144/SP398.9

Tomlinson, E.L., Smith, V.C. *et al*. 2015. The major and trace element glass compositions of the productive Mediterranean volcanic sources: tools for correlating distal tephra layers in and around Europe. *Quaternary Science Reviews*, **118**, 48–66, https://doi.org/10.1016/j.quascirev.2014.10.028

Tonga video. 2019. Sky News, August 27, https://news.sky.com/story/pumice-island-size-of-manhattan-floating-in-pacific-after-underwater-volcano-erupts-11795096

Trofimovs, J., Amy, L. *et al*. 2006. Submarine pyroclastic deposits formed at the Soufriere Hills Volcano, Montserrat (1995–2003): what happens when pyroclastic flows enter the ocean? *Geology*, **34**, 549–552, https://doi.org/10.1130/G22424.1

Trofimovs, J., Sparks, R.S.J. and Talling, P.J. 2008. Anatomy of a submarine pyroclastic flow and associated turbidity current: July 2003 dome collapse, Soufriere Hills Volcano, Montserrat, West Indies. *Sedimentology*, **55**, 617–634, https://doi.org/10.1111/j.1365-3091.2007.00914.x

Turney, C.S.M. 1998. Extraction of rhyolitic component of Vedde microtephra from minerogenic lake sediments.

Journal of Paleolimnology, **19**, 199–206, https://doi.org/10.1023/A:1007926322026

Van den Berg, J.H. and van Gelder, A. 1993. A new bedform stability diagram, with emphasis on the transition of ripples to plane bed in flows over fine sand and silt. *Special Publications of the International Association of Sedimentologists*, **17**, 11–21.

Van Eaton, A.R. and Wilson, C.J.N. 2013. The nature, origins and distribution of ash aggregates in a large-scale wet eruption deposit: Oruanui, New Zealand. *Journal of Volcanology and Geothermal Research*, **250**, 129– 154, https://doi.org/10.1016/j.jvolgeores.2012.10.016

Van den Bogaard, C. and Schmincke, H.-U. 2002. Linking the North Atlantic to central Europe: a high-resolution Holocene tephrochronological record from northern Germany. *Journal of Quaternary Science*, **17**, 3–20, https://doi.org/10.1002/jqs.636

Van Rijn, L.C. 2012. Simple general formulae for sand transport in rivers, estuaries and coastal waters, http://www.leovanrijn-sediment.com

Van Rijn, L.C. 2020. Literature review of critical bed-shear stresses for mud-sand mixtures, http://www.leovanrijn-sediment.com

Vannucchi, P., Sak, P.B., Morgan, J.P., Ohkushi, K., and Ujiie, K. and IODP Expedition 334 Shipboard Scientists 2013. Rapid pulses of uplift, subsidence, and subduction erosion offshore Central America: implications for building the rock record of convergent margins. *Geology*, **41**, 995–998, https://doi.org/10.1130/G34355.1

Vlag, P.A., Kruiver, P.P. and Dekkers, M.J. 2004. Evaluating climate change by multivariate statistical techniques on magnetic and chemical properties of marine sediments (Azores region). *Palaeogeography, Palaeoclimatology, Palaeoecology*, **212**, 23–44, https://doi.org/10.1016/S0031-0182(04)00302-5

Walker, G.P.L. 1981. Generation and dispersal of fine ash and dust by volcanic eruptions. *Journal of Volcanology and Geothermal Research*, **11**, 81–92, https://doi.org/10.1016/0377-0273(81)90077-9

Wallrabe-Adams, H.-J. and Lackschewitz, K.S. 2003. Chemical composition, distribution, and origin of silicic volcanic ash layers in the Greenland–Iceland–Norwegian Sea: explosive volcanism from 10 to 300 ka as recorded in deep sea sediments. *Marine Geology*, **193**, 273–293, https://doi.org/10.1016/S0025-3227(02)00661-8

Walter, T.R., Haghshenas Haghighi, M. *et al*. 2019. Complex hazard cascade culminating in the Anak Krakatau sector collapse. *Nature Communications*, **10**, 4339, https://doi.org/10.1038/s41467-019-12284-5

Wastegard, S., Johansson, H. and Pacheco, J.M. 2020. New major element analyses of proximal tephras from the Azores and suggested correlations with cryptotephras in north-west Europe. *Journal of Quaternary Science*, **35**, 114–121, https://doi.org/10.1002/jqs.3155

Ward, S.N. and Day, S. 2001. Cumbre Vieja Volcano – potential collapse and tsunami at La Palma, Canary Islands. *Geophysical Research Letters*, **28**, 3397–3400, https://doi.org/10.1029/2001GL013110

Watt, S.F.L., Talling, P.J. *et al*. 2012. Combinations of volcanic-flank and seafloor-sediment failure offshore Montserrat, and their implications for tsunami generation. *Earth and Planetary Science Letters*, **319**, 228–240, https://doi.org/10.1016/j.epsl.2011.11.032

Watt, S.F.L., Karstens, J. *et al*. 2019. From catastrophic collapse to multi-phase deposition: flow transformation, seafloor interaction and triggered eruption following a volcanic-island landslide. *Earth and Planetary Science Letters*, **517**, 135–147, https://doi.org/10.1016/j.epsl.2019.04.024

Wetzel, A. 2009. The preservation potential of ash layers in the deep-sea: the example of the 1991-Pinatubo ash in the South China Sea. *Sedimentology*, **56**, 1992–2009, https://doi.org/10.1111/j.1365-3091.2009.01066.x

White, M.J. and McPhie, J. 1997. A submarine welded ignimbrite – crystal-rich sandstone facies association in the Cambrian Tyndall group, western Tasmania, Australia. *Journal of Volcanology and Geothermal Research*, **76**, 277–295, https://doi.org/10.1016/S0377-0273(96)00105-9

White, J.D.L., Manville, V., Wilson, C.J.N., Houghton, B.F., Riggs, N.R. and Ort, M. 2001. Settling and deposition of AD 181 Taupo pumice in lacustrine and associated environments. *Special Publications of the International Association of Sedimentologists*, **30**, 141–150, https://doi.org/10.1002/9781444304251.ch7

Whitham, A.G. 1989. The behaviour of subaerially produced pyroclastic flows in a subaqueous environment: evidence from the Roseau eruption, Dominica, West Indies. *Marine Geology*, **86**, 27–40, https://doi.org/10.1016/0025-3227(89)90016-9

Whitham, A.G. and Sparks, R.S.J. 1986. Pumice. *Bulletin of Volcanology*, **48**, 209–224, https://doi.org/10.1007/BF01087675

Wiemer, G. and Kopf, A. 2015. Altered marine tephra deposits as potential slope failure planes? *Geo-Marine Letters*, **35**, 305–314, https://doi.org/10.1007/s00367-015-0408-4

Wiesner, M.G., Wang, Y. and Zheng, L. 1995. Fallout of volcanic ash to the deep South China Sea induced by the 1991 eruption of Mount Pinatubo. *Geology*, **23**, 885–888, https://doi.org/10.1130/0091-7613(1995)023<0885:FOVATT>2.3.CO;2

Wiesner, M.G., Wetzel, A., Catana, S.G., Listanco, E.L. and Mirabueno, H.T. 2004. Grain size, areal thickness distribution and controls on sedimentation of the 1991 Mount Pinatubo tephra layer in the South China Sea. *Bulletin of Volcanology*, **66**, 226–242, https://doi.org/10.1007/s00445-003-0306-x

Wilson, C.J.N. 2001. The 26.5 ka Oruanui eruption, New Zealand: an introduction and overview. *Journal of Volcanology and Geothermal Research*, **112**, 133–174, https://doi.org/10.1016/S0377-0273(01)00239-6

Winchester, S. 2003. *Krakatoa. The Day the World Exploded: August 27, 1883*. Harper Perennial (see pp. 293–296 on pumice rafts).

Wolfe, C.J., McNutt, M.K. and Detrick, R.S. 1994. The Marquesas Archipelagic Apron: Seismic stratigraphy and implications for volcano growth, mass wasting, and crustal underplating. *Journal of Geophysical Research*, **99**, 13591–13608, https://doi.org/10.1029/94JB00686

Wulf, S., Hardiman, M.J. *et al*. 2018. The Marine Isotope Stage 1–5 cryptotephra record of Tenaghi Philippon,

Greece: towards a detailed tephrostratigraphic framework for the eastern Mediterranean region. *Quaternary Science Reviews*, **186**, 236–262, https://doi.org/10.1016/j.quascirev.2018.03.011

Wulf, S., Keller, J. *et al*. 2020. Advancing Santorini's tephrostratigraphy: new glass geochemical data and improved marine-terrestrial tephra correlations for the past ~360 kyrs. *Earth-Science Reviews*, **200**, 102964, https://doi.org/10.1016/j.earscirev.2019.102964

Zeng, J. and Lowe, D.R. 1997. Numerical simulation of turbidity current flow and sedimentation: I. theory. *Sedimentology*, **44**, 67–84, https://doi.org/10.1111/j.1365-3091.1997.tb00424.x

Zhao, Z., Mitchell, N.C., Quartau, R., Tempera, F. and Bricheno, L. 2019. Submarine platform development by erosion of a surtseyan cone at Capelinhos, Faial Island, Azores. *Earth Surface Processes and landforms*, **44**, 2982–3006, https://doi.org/10.1002/esp.4724

Zhiyao, S., Tingting, W., Fumin, X. and Ruijie, L. 2008. A simple formula for predicting settling velocity of sediment particles. *Water Science and Engeneering*, **1**, 37–43, https://doi.org/10.3882/j.issn.1674-2370.2008.01.005

Zielinski, G.A., Mayewski, P.A. *et al*. 1997. Volcanic aerosol records and tephrochronology of the Summit, Greenland, ice cores. *Journal of Geophysical Research*, **102**, 625–640.